UNIVERSITY OF CALIFORNIA,
IRVINE

MEMS Components for NMR Atomic Sensors

DISSERTATION

submitted in partial satisfaction of the requirements
for the degree of

DOCTOR OF PHILOSOPHY

in Electrical Engineering and Computer Science

by

Radwan M. Mohammednoor

Dissertation Committee:
Andrei M. Shkel, Chair
Ozdal Boyraz
Lorenzo Valdevit

2019

DEDICATION

This dissertation and all my academic achievements are dedicated
to my inspiring parents, Mohammedshafia Mohammednoor and Khayriah Qari,
to my best friend and my beloved wife, Abrar Bawakid,
and to my adorable children Danah and Ibrahim,
without whom this dissertation would have never been completed.

TABLE OF CONTENTS

LIST OF FIGURES

LIST OF TABLES

ACKNOWLEDGMENTS

First and foremost, I thank Almighty Allah for giving me the strength and patience to work through all these years so that today I can stand proudly with my head held high.

I would like to start by acknowledging my Ph.D. advisor Professor **Andrei Shkel**, for his guidance, support, encouragement, patience, and his believe in me and my work throughout my study period.

I would like to thank the other members of my dissertation committee, Professor **Ozdal Boyraz** and Professor **Lorenzo Valdevit** for their valuable feedback and devoting time of their busy schedules.

I extend my thanks to my colleagues in the MicroSystems Laboratory, Venu Gundeti, Yu-Wei Lin, Mohammad Asadian, Nikita Kulachenkov, Danmeng Wang, and Sina Askari for sharing their expertise and knowledge. I am also thankful to my other colleagues for their support and help. I also would like to thank the Integrated Nanosystems Research Facility (INRF UCI) staff, Mo Kebaili and Jake Hes for their help in the fabrication part of the research.

I will be forever thankful to **Abrar Bawakid**, my wife and my best friend. Her unfailing love, support, understanding, and encouragement has seen me through hectic times. I thank her for patiently and simultaneously raising our adorable children and bringing joy to our family. I also thank my little sweet children, **Danah** and **Ibrahim**, for the patience they showed me during this journey.

I deeply thank my parents, Mohammedshafia Mohammednoor and Khayriah Qari, for their prayers and their inculcating in me the dedication and discipline to do whatever I undertake well. I also thank my brother, Safwan, Baraa, Aamer, and Imran, and my sisters, Arwa, Abrar, Ebtehal, Afnan, and Asmaa, for their support and kind help. I extend my gratitude to my parents-in-law, Omar Bawakid and Afaf Bawakid, for their support to our family during this journey.

This research was supported partially by NSF, DARPA, and ADD.

I acknowledge the full scholarship of King Abdulaziz City for Science and Technology (KACST).

I am also thankful to IEEE for granting me permission to reuse my pre-published material in this dissertation.

CURRICULUM VITAE

Radwan M. Mohammednoor

EDUCATION

Master of Science in Electrical Engineering **2014**
University of Southern California *Los Angeles, CA, USA*

Bachelor of Science in Electrical Engineering **2008**
King Abdulaziz University *Jeddha, Saudi Arabia*

RESEARCH EXPERIENCE

Graduate Research Assistant **2014–2019**
Microsystems Laboratory, University of California, Irvine *Irvine, CA, USA*

REFEREED JOURNAL PUBLICATIONS

Reconfigurable Analog Emulator: a Tool for Development of NMR Atomic Sensors **2019**
IEEE Sensors Journal- manuscript submitted

Design Considerations for Micro-Glassblown Atomic Vapor Cells **2019**
IEEE Journal of MicroElctroMechanical Systems (JMEMS)- manuscript submitted

MEMS Components for NMR Atomic Senors **2018**
IEEE Journal of MicroElctroMechanical Systems (JMEMS)

INTERNATIONAL CONFERENCE PUBLICATIONS

Study on Micro glassblown cells for NMR Sensors **Apr. 2019**
IEEE INERTIAL '19

Design Space Exploration of Hemi-Toroidal Fused Quartz Shell Resonators **Apr. 2019**
IEEE INERTIAL '19

Status of Component Development for NMR gyro **Mar. 2017**
IEEE INERTIAL '17

ABSTRACT OF THE DISSERTATION

MEMS Components for NMR Atomic Sensors

By

Radwan M. Mohammednoor

Doctor of Philosophy in Electrical Engineering and Computer Science

University of California, Irvine, 2019

Andrei M. Shkel, Chair

This dissertation introduces a batch fabrication method to manufacture Micro-Electro-Mechanical System (MEMS) components for NMR atomic sensors, such as NMR gyroscope (NMRG) and NMR magnetometer (NMRM). The introduced method utilized a glassblowing process, origami-like folding, and a more traditional MEMS fabrication. We developed an analytical model of imperfections, including errors associated with micro-fabrication of MEMS components. In light of the developed error model and experimental evaluation of components, we predicted the effect of errors on performance of NMRG and NMRM. We concluded that with a realistic design, a 5mrad angular misalignment between coils and folded mirrors and a 100um linear misalignment between folded coils, it would be feasible to achieve an NMRG with ARW $0.1°/\sqrt{hr}$ and an NMRM with sensitivity on the order of $10\text{fT}/\sqrt{Hz}$ using MEMS technology.

A design process for miniaturized atomic vapor cells using the micro-glassblowing process was presented in this dissertation. Multiple design considerations were discussed, including cell geometry, optical properties, materials, and surface coating. The geometry and the optical properties were studied using experimentally verified analytical and Finite Element Models (FEM). The cell construction material and surface coating were the focus of our experimental study on factors that affect the transverse relaxation time (T2) of nuclear

spins. We showed that the developed wafer-level coating process with Atomic Layer Deposition (ALD) of Al2O3 increased the relaxation time (T2), which is projected to reduce the ARW of NMR gyroscopes and the sensitivity of NMR magnetometers by four times.

Complementary to the developed atomic sensors components, an analog emulator for NMR atomic sensors was developed. The emulator represents the spin dynamics of atoms in an applied magnetic field that are governed by Bloch equations. Characterization of atomic sensors' components using the emulator was achieved by including one or more of those components with the emulator in a hardware-in-the-loop (HIL) configuration. Finally, we presented a comparison of the response between the NMR emulator and an actual NMR system, showing similarities of responses of the two systems and feasibility of using HIL configuration in development of micro-scale NMR sensors. In summary, the contribution of this thesis is summarized as follows:

- Developed and experimentally verified the analytical model that links the folding accuracy to the atomic sensor performance;
- Developed a wafer-level fabrication process of a network of interconnected atomic cells utilizing glassblowing technology;
- Demonstrated the feasibility of filling an array of atomic cells simultaneously with noble and buffer gases, and measured the noble gas response as well as the pressure of all gases after sealing.
- Developed a multi-aspect design process for producing highly spherical glassblown cells within the practical limits of the fabrication process. Identified that the critical design process aspects are geometry, optical properties, surface coating, and material.
- Presented design and validation of an NMR atomic sensor emulator. The emulator was developed for characterization and analysis of the developed components in a hardware-in-the-loop configuration.

Chapter 1

Introduction

1.1 Motivation

Inertial sensors utilize inertia to measure the relative motion of an object. There are two types of inertial sensors, accelerometers which measure an object's linear acceleration, and gyroscopes which measure the rotation of an object. These sensors have a wide range of applications from consumer electronics, such as cell phones and gaming consoles, to industrial applications, such as automotive industry, all the way to navigation and military applications.

The motivation for developing high-performance inertial sensors is to target scenarios where GPS signal is not accessible. Some examples for those scenarios are underwater navigation, or when GPS signal is jammed, or cannot be trusted.

1.2 Trends in Inertial Sensors and Magnetometers

Depending on the physical principle of operation gyroscopes can be divided into three broad categories

Vibratory: Vibratory gyroscopes depend on Coriolis force, which is a rotation induced coupling between two modes of vibration of a mechanical resonator, [1, 4]. They are mostly found in consumer applications, such as smart-phones and video games consoles. Gyroscopes used for consumer applications have Angle Random Walk (ARW) usually on the order of 10-0.1°/$\sqrt{hr}$.

Optical: Optical gyros are the standard for Navigation applications, and they are used on-board of airplanes. Optical gyroscopes deploy the Sagnac effect to detect rotation, where two beams of light are sent in opposite closed paths and, when a rotation is applied, a phase shift occur between the two light beams which can be detected using an interferometer. Ring Laser gyroscope (RLG) can achieve ARW on the order of 0.005°/$\sqrt{hr}$.

Atomic: The last category is the atomic gyroscopes, where atoms motion is used to detect rotation. Atomic gyroscopes can be divided into two subcategories. Atomic interferometry gyros (AIG) (also referred to as cold atoms gyros) and atomic spin gyros (ASG) (usually referred to as warm atoms gyros), [37]. Atomic interferometry gyros are similar to optical gyros. However, atoms are treated as waves instead of photons, [58, 55, 105, 27]. On the other hand, Atomic spin Gyros (ASGs) utilize the spin property of atoms to track rotation. Atomic spin gyros have multiple implementations. One of them is the Nuclear Magnetic Resonance Gyroscope (NMRG). These devices are still in the prototype phase and are projected to achieve ARW better than 0.001°/$\sqrt{hr}$.

Magnetometers are classified based on their physical principle of operation into two categories. Sensors with a magnetic core and non-magnetic core.

Magnetometers with magnetic core: These magnetometers contain a magnetic

core, and the external magnetic field changes the physical properties of the core. Examples of those magnetometers include fluxgate [10, 78], Hall-effect [103], magnetoresistive [11, 14], and cavity optomechanical magnetometers [96, 52, 17]. These magnetometers are used in Earth's magnetic field mapping and industrial applications, such as current monitoring and magnetic memory read-out, [71, 131]. These magnetometers usually have medium to low sensitivity and are limited in performance to pico-Tesla range ($10^{-12}T$)

Magnetometers with non-magnetic core: These magnetometer respond to a magnetic field by inducing a quantum mechanical effect (quantum magnetometers), they have high sensitivity and can measure ultra-small magnetic fields in the ranges of Femto-Tesla ($10^{-15}T$) and atto-Tesla ($10^{-18}T$). Superconducting quantum interference device (SQUID), [16], optically pumped atomic magnetometers [19], and nitrogen-vacancy center (NV center) in diamond [119], are examples of this category of magnetometers. Quantum magnetometers are utilized in non-invasive biomedical applications, such as magnetic resonance imagining (MRI), magnetocardiography (MCG), and magnetoencephalography (MEG). They are also used in Nuclear Magnetic Resonance (NMR) spectroscopy, [109]. A subcategory of optically pumped atomic magnetometers is the NMR magnetometer.

Our discussion in this dissertation is focused on NMR gyroscopes and NMR magnetometers.

1.3 Atomic Sensors History

NMRG concept was first introduced in the early 1950s, [47]. However, the actual development started in the 1960s when General Electric and TRW started research and development on building first prototypes. In these first experiments, they used optical means similar to what is being used today to polarize the nuclear Spins, [41, 115, 6].

The 1970s was the prime time for NMRG development; many companies and research labs started exploring different NMRG implementations. Two of the promising implementations at that time were introduced by Singer, and Litton Systems. Singer's implementation used two isotopes of mercury and a mercury lamp to polarize and detect the nuclear spins directly, [12]. Litton's implementation used noble gas spins, Like Xe, and an intermediate atom species, in their case it was Rb, to polarize the noble gas and detect it, [45]. Most of today's implementations use this combination of alkali metal and a noble gas, [64, 70]. Litton reported the highest performance of NMRG at that time, with ten times improvement in the noise level over Singer's NMRG, [44].

At the beginning of the 1980s, the rush for NMRG development slowed down. There are two reasons for that. The first was, the lack of enabling technology, such as stable lasers at Rubidium wavelength; The second reason was a fast development of competing technologies, like the fiber optic gyro. For nearly 25 years, there was no significant development in NMRG.

In the 2000s another rush to develop NMRG took place, but this time it was on a chip-scale. In the past 15 years, the interest to develop miniaturized NMRG has grown up significantly. Many research groups and companies around the world started developing their chip-scale versions of NMRG.

1.4 Atomic Sensors Miniaturization

Atomic sensors can deliver a precise measurement of physical quantities, such as time, magnetic field, and rotation by utilizing a cloud of conditioned atoms, [58]. For example, in table-top setups, an atomic magnetometer can measure magnetic fields with a sensitivity of $1fT/\sqrt{Hz}$, [63], and an atomic gyroscope can measure rotation with an Angle Random Walk (ARW) of 0.002 deg/$\sqrt{hr}$, [69]. The emerging applications that demand low-cost chip-scale

atomic sensors, [114, 65], have started a trend in the early 2000s on the miniaturization of atomic sensors and their components. The advancements in miniaturized cell fabrication, [2, 35, 100, 43], and Vertical Cavity Surface Emitting Lasers (VCSELs), [112], encouraged developments towards miniaturization of atomic clocks, [62], atomic magnetometers (NMRMs), [60, 53, 57], and atomic gyroscopes (NMRGs), [79, 3, 57].

The process of conditioning atoms for atomic sensors (such as NMRM and NMRG) consists of multiple steps. The first step is to confine the atomic cloud in a container, i.e., a vapor cell. The next step is to heat the cell, which is necessary to vaporize the alkali metal and to increase the vapor pressure, which would effectively increase the signal-to-noise ratio of the measurement. This is followed by aligning the atomic spins of nuclei by applying a precise static and oscillating magnetic fields via electromagnetic coils. The next step is to optically polarize the spins using a laser source, assuring that their magnetic moments are aligned forming a net magnetization vector. Lastly, in the case of NMRG, the sensor is encapsulated using a μ-metal shield to preserve this conditioning during sensor operation. In the case of NMRM, no magnetic shield would be typically used.

The utilization of Micro-Electro-Mechanical Systems (MEMS) techniques accelerated the advancement of miniaturization of atomic cells, [36, 99, 61]. However, MEMS techniques have not been adopted widely for other essential components of atomic sensors, such as multi-axis magnetic field coils, cell heaters, and optical components. In previous studies, [57, 70], multi-axes coils and cell heaters were realized through flexible printed circuit boards technique. Individually machined optical apparatus, such as lenses and light reflectors, were assembled to route the light in-and-out of the cell, [84][70]. One obvious limitation of such techniques was that the components were picked and placed individually, which made the assembly process inefficient and devices bulky. MEMS techniques offered an approach to address this limitation by utilizing a lithography driven batch fabrication.

To address the limitation of individually picking and placing components, a minia-

turization method based on micro-fabrication of NMR components on a wafer-level was introduced, as a potential approach for size, weight, power, and cost (SWaP+C) reduction. The method combined micro glassblowing technology for fabrication of miniaturized atomic cells, [36], and a 3-D folded MEMS structures, [134], for the fabrication of magnetic coils, interconnects, silicon backbones, and light reflectors. However, miniaturization come with a cost of imperfections. In this dissertation, we discuss and analyze the contribution of errors introduced by each component on the overall performance of NMR atomic sensors. We then demonstrate that MEMS-based implementation is a potential candidate for precision sensing.

Although the miniaturization of atomic sensors started with the miniaturization of the atomic cells, [36, 99, 61], to date, there are challenges in achieving the full potential of miniaturized cells. Some of the challenges in cells development that arise from miniaturization include: developing a batch fabrication process that yields low size, weight, power, and cost (SWAP+C) cells [114]; developing low SWAP+C cells with geometrical requirements, such as multiple optical ports and cell symmetry; developing cells with homogeneous wall material; developing cells with wall coatings and materials that preserve the atomic polarization inside the cells.

Multiport cells are needed for some applications, such as Nuclear Magnetic Resonance (NMR) gyros and magnetometers, [70, 20], while symmetry is preferred to avoid unwanted phenomena, such as self magnetization and quadruple shift, [130]. In-homogeneity in the cell wall material creates an electric field gradient across the cell, [31], which results in a quadruple frequency shift that negatively affects the performance of NMR atomic sensors. Additionally, as we miniaturize atomic cells, the interaction of the atomic vapor with the cell walls increases due to increase of the surface area to volume ratio, [56]. So, the cell material and the surface treatment need to be carefully addressed.

The fabrication and filling of miniaturized-glassblown spherical cells, [34, 91, 94], enabled

a wafer-level fabrication of highly spherical axis-symmetric multiport cells with homogeneous wall material that addresses some of the previously mentioned challenges. In this dissertation, we discuss the different design aspects of miniaturized atomic cells. The design process aspects include geometry, optical properties, material, and surface treatment (coating). The design process combines analytical, [34], with finite element modeling (FEM) of the cell's geometry and optical properties, [8, 9], backed up with experimental validation as well as a study on different cell wall materials and surface coating, [93].

1.5 Atomic Sensors Emulator

Atomic sensors have been used to measure multiple physical quantities, such as time, magnetic field, and rotation with high precision, [63, 73, 69, 70, 58]. The main building blocks of such sensors are the sensing unit (physics package) and control electronics. The physics package of a Nuclear Magnetic Resonance Gyroscope (NMRG), as mentioned in the previous section, includes an atomic vapor cell, a cell heater, magnetic field coils, a magnetic shield, light sources, photo-detectors, and optics, [30]. Control electronics include temperature control, magnetic field control, light sources control, rotation rate read-out, and feedback electronics, [125].

Development of physics package received much attention in recent years, [62, 72, 60, 135, 53, 57, 79, 3, 126]. The general approach for the development of atomic sensors starts with the physics package followed by the control electronics. With this approach, the effect of individual components on the overall sensor performance can be only measured after assembly of the physics package completed, which is a lengthy and costly process. The sequential process of development also adds a lead time to the development of control electronics.

Emulators have been used in many applications, including Micro-Electro-Mechanical

Systems (MEMS) sensors [86], fuel cells [75], and biomedical applications [104]. In this dissertation, we introduce a reconfigurable analog emulator that mimics the spin dynamics of a noble gas. The benefits of using a reconfigurable analog emulator are:

- Parallel development of physics packages and control electronics;
- Visualization of characteristics of the atomic sensor components on the overall sensor's performance;
- Fine-tuning of control electronics with pre-determined atomic sensors parameters;
- Independent development and testing of electronics dedicated to atomic sensors.

1.6 Research Objective

The research objective to develop an approach for high-performance atomic sensors components using batch fabrication processes. These components can be used in various atomic sensors, including NMR gyroscope and NMR magnetometers. There are two processes involved in component development. The first process is the MEMS 3D folding technique, which can be utilized for fabrication of the NMR sensor magnetic field coils, heater, light reflectors, and sensor backbone. The second is the utilization of micro glassblowing technique in fabrication and filling of miniaturized NMR atomic vapor cells.

The folded components development included the assessment of the process limitations by developing analytical and finite element models that link fabrication imperfections' to sensor performance. The miniaturized atomic vapor cell development includes demonstrating the fabrication and filling technique as well as optimizing cell design process.

A complementary objective is to develop an atomic sensor emulator that aids sensor development. The emulator works as a characterization and analysis platform of the devel-

oped components, by connecting one or more atomic sensors components with the emulator in a hardware-in-the-loop configuration.

1.7 Dissertation outline

The principle of operation of NMR atomic sensors is introduced in Chapter 2. In Chapter 3, a miniaturization method for NMR atomic sensors based on the micro-fabrication of NMR components on a wafer-level is introduced, as well as discussion and analysis of the contribution of fabrication imperfections to the overall performance of NMR atomic sensors. Different design aspects for miniaturized NMR atomic vapor cells utilizing the glassblowing technology are discussed in Chapter 4. Chapter 5 presents an analog NMR sensor emulator as a tool to characterize the developed components. Finally, Chapter 6, concludes the dissertation, highlights the dissertation contribution and gives an outlook on future research direction.

Chapter 2

NMR Sensors: Principle of Operation

To explain the operation for NMR sensors, we will first discuss the underlying physics using a simplified model of the atom. Then, the operation of those sensors will be introduced.

2.1 Background

Let us take the example of a hydrogen atom with one valence electron in its outer shell. This electron's spin around its axis is identified as "spin angular momentum," and it takes the values of $\pm 1/2$ depending on the energy (higher energy $+1/2$, lower energy $-1/2$). This spin can be considered as a vector $\vec{S}$.

The same electron's orbit around the nucleus is referred to as "orbital angular momentum," which is considered as a vector as well and it is denoted by $\vec{L}$. We can use the vector sum, Figure 2.1-(a,b), to add those two angular momenta and we obtain

$$\vec{J} = \vec{S} + \vec{L} \tag{2.1}$$

where $\vec{J}$ is the total angular momentum of the electron. Similar to the electrons, protons

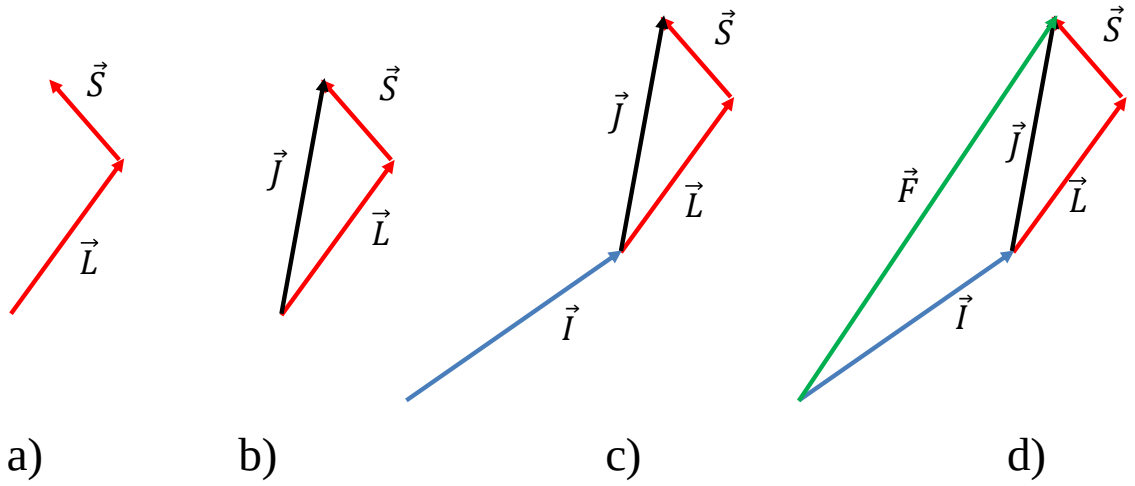

Figure 2.1: Vector sum of different angular momenta

and neutrons have "spin angular momentum." Generally, when two spins pair with each other they cancel each other out, so the effective spin of the nucleus $\vec{I}$ is the summation of spins from unpaired protons and neutrons, as shown in Figure 2.1-(c). The net angular momentum of the whole atom, as seen in Figure 2.1-(d), is then calculated as

$$\vec{F} = \vec{I} + \vec{J} \tag{2.2}$$

Each one of the angular momenta ($\vec{S}$, $\vec{L}$, $\vec{J}$, $\vec{I}$ and $\vec{F}$) has an associated magnetic moment. For our discussion, we will focus on the magnetic moment associated with the nuclear spin $\vec{\mu_I}$. This magnetic moment of the spin can be considered as a magnetic dipole, as shown in

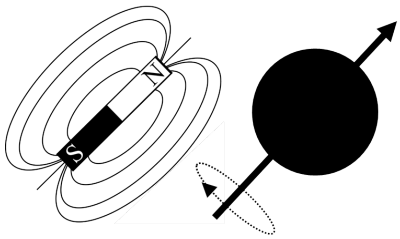

Figure 2.2: spinning charged particles have a magnetic moment similar to that of a magnetic dipole (bar magnet)

Figure 2.2, and it is related to the nuclear spin as follows

$$\vec{\mu_I} = \gamma_I \vec{I} \tag{2.3}$$

The quantity γ_I is a unique value for each element isotope and is called the gyromagnetic ratio, and it is defined as

$$\gamma_I = \frac{e}{2m_p} g_I, \tag{2.4}$$

where e is the elementary charge, m_p is the mass of a proton, and g_I is the nuclear g-factor.

This section reviewed a simplified description of the basic background of the hydrogen atom model, [120, 39]. A similar model can be applied to the Alkali metals. These elements occupy the first column of the periodic table (Li, Na, K, Rb, Cs, Fr). Alkali metals have only one free electron in their outer shell.

2.2 Nuclear Magnetic Resonance

We have established the relation between the spinning motion and the magnetic moment and the fact that those magnetic moments are considered as magnetic dipoles. Let us now discuss the concept of magnetic resonance. Assume we have a group of atoms, each one of

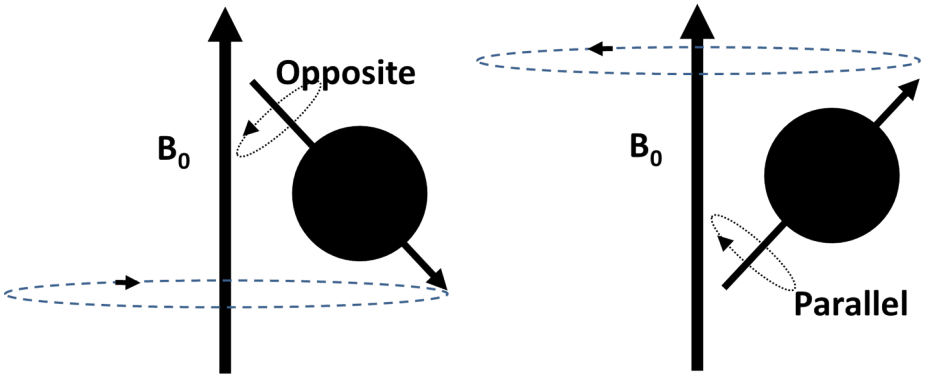

Figure 2.3: States of atoms in external magnetic field

those atoms has a net spin and subsequently a magnetic moment. Naturally, the direction of the magnetic moment of those atoms is random. If we apply an external DC magnetic field $\vec{B_0}$, there will be a torque acting on those magnetic moments trying to align them to the direction of the applied magnetic field. This torque is described as follows

$$\frac{d\vec{I}}{dt} = \vec{\mu_I} \times \vec{B_0} \tag{2.5}$$

The energy states of the outer electrons and the nucleus distribute the atoms equally into high and low energy states. High energy states are aligned along the magnetic field, and the other half is in the opposite direction, as shown in Figure 2.3. Once these atoms are parallel with $\vec{B_0}$, they start to precess about the magnetic field $\vec{B_0}$. The motion the nuclei spin can be described by

$$\frac{d\vec{\mu}_I}{dt} = \vec{\mu_I} \times \gamma_I \vec{B_0} \tag{2.6}$$

The frequency of precession is identified as the Larmor frequency and is given by

$$\vec{\omega}_L = \gamma_I \vec{B_0}, \tag{2.7}$$

where γ_I is the gyromagnetic ratio described by equation (2.4). Almost half of the atoms will precess clockwise, and the other half will precess counter-clockwise. If we injected atoms at the lower energy state with the exact amount of energy, this will bring them to the higher energy state, and we could achieve a spin-flip. In this case, the magnetic moments of all atoms will add up to form a net magnetization vector. The spin-flip is achieved by applying an RF magnetic field with a specific frequency that is proportional to the energy difference between the higher and lower states:

$$\nu = \frac{E}{\hbar} \tag{2.8}$$

where E is the energy difference between the states in (J), $\hbar$ is Planck's constant, and ν is the frequency in Hz. Once we remove the RF magnetic field, the atoms will try to go back to their original state (relaxation), producing a signal proportional in its frequency to the signal used for the spin-flip. This operation is called Nuclear Magnetic Resonance (NMR).

In classical applications of NMR, such as magnetic resonance imaging (MRI), the spin-flip is done via an RF magnetic field with frequency on the order of 100's of MHz, and detection of the generated signals is done using a superconducting quantum interference device (SQUID), [16]. SQUID is a coil that is cooled to near 0°K, which makes it a superconductor. It is used as a magnetometer that can measure ultra-low fields on the order of atto-Tesla (10^{-18}T), [24]. In our discussion throughout this dissertation, for implementation of NMR sensors we will use laser sources for atoms' alignment (polarization) and detection instead of RF signals and SQUID. The polarization of atoms will be introduced later in section 2.4, while the detection will be discussed in section 2.6.

2.2.1 NMR Gyroscopes and Magnetometers

To explain how this phenomenon can be used to make NMR sensors (gyroscopes and magnetometers), let us go back to equation (2.7) and assume that we aligned all the atoms to the direction of the applied magnetic field. For NMR gyroscopes, if we rotated the whole frame with a frequency of $\vec{\omega_R}$, the observed precession will be

$$\vec{\omega}'_L = \gamma_I \vec{B}_0 \pm \vec{\omega}_R \tag{2.9}$$

For NMR magnetometers, if we applied an external magnetic field $\delta\vec{B}_z$, then the observed frequency of precession will be

$$\vec{\omega}'_L = \gamma_I \vec{B}_0 \pm \gamma_I \delta\vec{B}_z \tag{2.10}$$

In both cases, a net magnetic field will be generated either due to a rotation of the frame (in the case of gyroscopes) or due to an external magnetic field (in the case of magnetometers). This field is given by

$$\vec{\omega}'_L \;\; = \;\; \gamma_I \vec{B}'_0 \tag{2.11}$$

We assume we have a method of measuring the net magnetic field $\vec{B}'_0$. By substituting equation (2.11) for equation (2.9), the rotation rate of the NMR gyroscope is

$$\vec{\omega}_R \;\; = \;\; \gamma_I(\vec{B}_0 - \vec{B}'_0), \tag{2.12}$$

and from equations (2.10) and (2.11), the external magnetic field for the NMR magnetometer is

$$\delta\vec{B}_z = \vec{B}_0 - \vec{B}'_0, \tag{2.13}$$

where $\vec{B}_0$ is the applied magnetic field, $\vec{B}'_0$ is the measured field, and γ_I is a constant value for our atom species.

2.2.2 Dual Isotopes

We notice from equation (2.12) that the NMR gyroscope is dependent on the net field experienced by atoms and any fluctuations in that field will be identified as rotation. For this reason, NMR gyros require magnetic shielding. There are two types of magnetic shielding, passive shielding and active shielding. Passive shielding is achieved by placing the sensor inside a high permeability μ-metal shield, however, there are limitations to the passive shielding approach and an active shielding is necessary to achieve high-performance gyros, [31]. Active shielding is carried out by continuously measuring the field fluctuations and canceling them out. On the other hand, equation (2.13) shows that any rotation of the NMR magnetometer will be identified as a change in the magnetic field. To overcome this issue, we need to monitor the system rotation actively and cancel it out from the sensor's readout.

Active shielding of NMRG and active rotation cancellation for NMRM can be addressed by introducing another atom species with different gyromagnetic ratio to the gas mixture, in most cases another Xe isotope is introduced.

In the case of NMR gyros, the two isotopes will precess at two different frequencies, equation (2.7) becomes

$$\omega_1 = \gamma_1 B_0 \tag{2.14}$$

$$\omega_2 = \gamma_2 B_0 \tag{2.15}$$

When we apply a rotation rate to the sensor, the observed frequencies of the two isotopes

become

$$\omega_1' = \gamma_1 B_0 \pm \omega_R \tag{2.16}$$

$$\omega_2' = \gamma_2 B_0 \pm \omega_R \tag{2.17}$$

Solving the two equations (2.16) and (2.17) for B_0, we obtain

$$B_0 = \frac{\omega_1' - \omega_2'}{\gamma_1 - \gamma_2}, \tag{2.18}$$

Substituting equation (2.18) into equation (2.16), the rotation rate becomes

$$\omega_R = \frac{\gamma_1 \omega_2' - \gamma_2 \omega_1'}{\gamma_1 - \gamma_2}. \tag{2.19}$$

We note that ω_R is only dependent on the gyro magnetic ratios of the two isotopes, and their observed frequencies, and it is independent of B_0.

On the other hand, in the case of NMRM, when an external magnetic field δB_z is applied and assuming a parasitic system rotation is present, the observed Larmor frequencies of the two isotopes become

$$\omega_1' = \gamma_1 B_0 \pm \gamma_1 \delta B_z \pm \omega_R, \tag{2.20}$$

$$\omega_2' = \gamma_2 B_0 \pm \gamma_2 \delta B_z \pm \omega_R. \tag{2.21}$$

Solving equations (2.14), (2.15), (2.20) and (2.21) for δB_z, we obtain

$$\delta B_z = \frac{(\omega_1' - \omega_2') - (\omega_1 - \omega_2)}{\gamma_1 - \gamma_2}, \tag{2.22}$$

where ω_1' and ω_2' are the observed frequencies, while ω_1 and ω_2 are the reference frequencies

of the two isotopes. We can see that the external magnetic field of NMRM depends on the observed frequencies, the gyromagnetic ratios, and the reference frequencies of the two isotopes. With the two isotope approach, the parasitic rotation have been eliminated.

2.3 Choice of Atoms

2.3.1 NMR Elements

The key element in designing of NMR sensors is selecting proper atom species. This selection process depends on several factors. In this section, we will mention those factors and why they are important in the selection process. First, the gyromagnetic ratio of the species needs to be on the smaller side for more precise measurement of rotation, [125]. The gyromagnetic ratios for some elements (He, Ne, Kr, Xe, and Hg) are in the range of ($2\pi \times$ (1 - 32) Hz/μT). On the other hand, the elements like alkali metals have gyromagnetic ratios two order of magnitude higher (e.g., $2\pi \times 6998$ Hz/μT for ^{87}Rb), [116, 117]. Relaxation time is another factor for choosing atoms for implementation of NMR sensors. Relaxation times range from milliseconds, for elements such as alkali metals to several days in the case of ^{3}He, [40, 51]. The optimum range is tens of seconds for a millimeter size cell, [125]. Selecting atom species with non-zero nuclear spin is essential for the process of NMR gyro. Finally, the ability to polarize and detect the atoms optically using lasers is also essential for the selection process.

These factors help to develop elementary selection criteria for the NMR atom species. Xenon, and specifically (^{129}Xe), is a great candidate matching our criteria. It has a gyromagnetic ratio of ($2\pi \times 11.86\ rad.s^{-1}/\mu$T), [117], a relaxation time of 180s was reported for a cell size of 25mm^3, [49], and it has a nuclear spin of $\frac{1}{2}$, [121]. Nevertheless, Xe is an inert element and it is not possible to directly polarize Xe using a laser.

2.3.2 Alkali Metal

To overcome this problem, we introduce another atom species that can be polarized and detected using laser sources, and at the same time is capable to transfer that polarization to and from Xe atoms. This process of transferring the polarization to and from Xe is called spin exchange, and it is covered in more details in section 2.5. Choosing Alkali metals (Li, Na, K, Rb, Cs) is an excellent choice for this task, each one of them has a single valence electron in their outer shell, which makes it easier to model and understand their behavior. The criteria to choose between the alkali metals are melting point and availability of laser source to excite them. The melting points of Lithium, Sodium, and Potassium are relatively high (180°C-63°C) when compared to Rubidium and Cesium (39°C) and (28°C). High melting points require large heating power to convert alkali metals from solid to vapor phase, which consumes a lot of power and is not desirable for potential applications. So, starting with elements with low melting points is optimal to efficiently utilize the power budget of implementation. Nevertheless, (NA, K) are prevalent in table-top high-temperature magnetometers that are not limited by a power budget, [63, 28, 5]. Recent advancements in vertical-cavity surface-emitting lasers (VCSEL), [85], made it possible to access small size, low cost, and power-efficient laser sources at the Cs and Rb absorption wavelengths, [80], which is a breakthrough in NMR sensors miniaturization. Both Cs and Rb are used in miniaturized atomic sensors. In our implementation, we will focus on Rb.

Next, we will introduce the process to polarize the alkali metal atoms. This process is called "Optical Pumping."

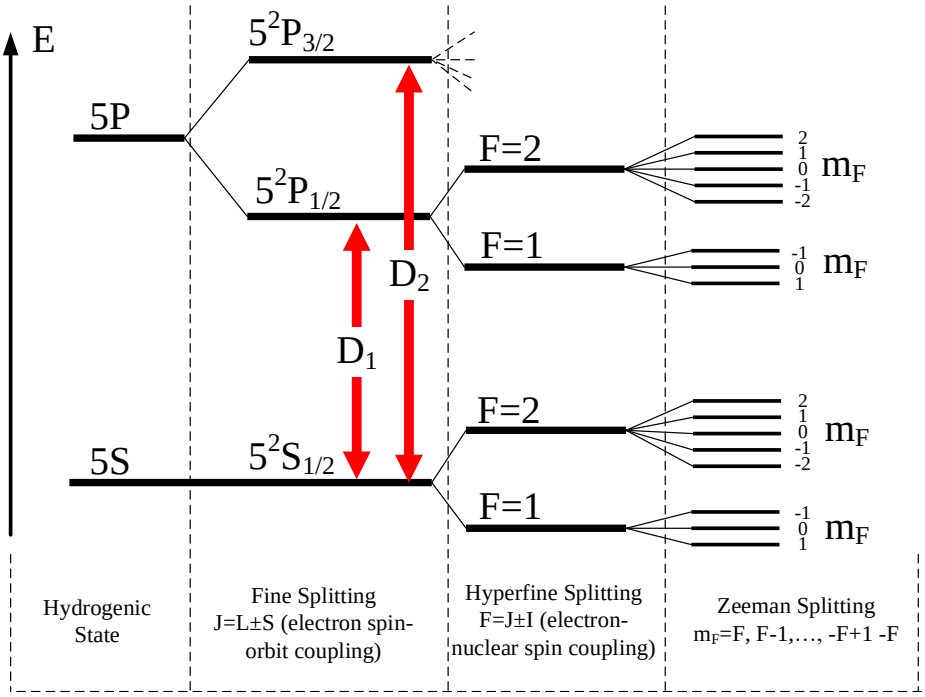

Figure 2.4: Energy Level Splitting in ^{85}Rb

2.4 Optical Pumping

As was discussed earlier, polarizing the alkali atoms can be achieved using an RF signal or optical method. Before we discuss the optical pumping process, we first need to introduce the energy level diagram of an alkali metal (e.g., ^{85}Rb), shown in Figure 2.4. The diagram consists of four parts. The first on the left is the hydrogenic state (5S, 5P); it can be considered as the orbit of the electron in our simplified model. Next, is the fine splitting resulting from the electron spin ($\vec{J}$), equation (2.1), denoted by ($5^2S_{1/2}$, $5^2P_{1/2}$, $5^2P_{3/2}$) in Figure 2.4. Next, the hyperfine splitting, which is a result of adding the nuclear spin to the electron spin, is introduced in equation (2.2) and denoted by F in Figure 2.4. Finally, the Zeeman splitting, which will occur whenever there is a magnetic field applied and is labeled by m_F in Figure 2.4.

Let us assume we have an ensemble of Rb atoms in an applied DC magnetic field.

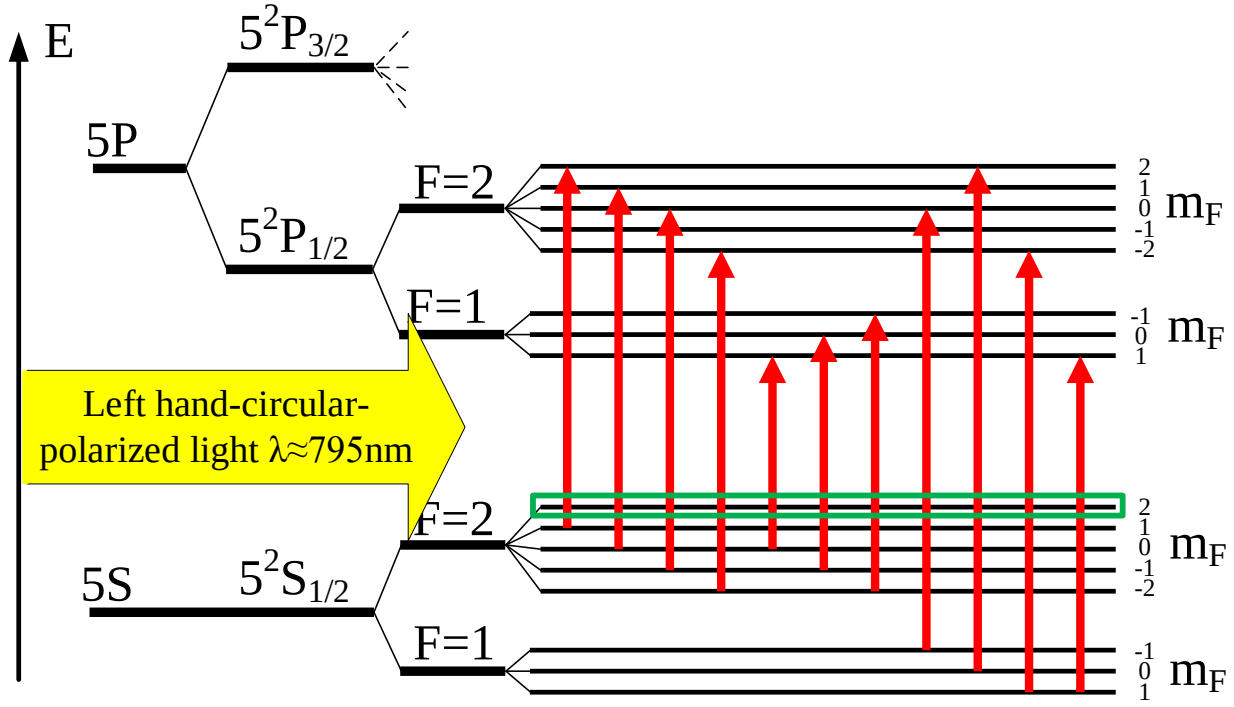

Figure 2.5: Expanded Zeeman splitting region showing atoms' behavior during the left-hand circular light excitation. Green box shows the eventual m_F state for all of the atoms

Those atoms will be distributed across the Zeeman states of $5^2S_{1/2}$ in Figure 2.4. Each one of those atoms will have a specific m_F number depending on its state. It could be any value of $(m_F = -2, -1, 0, 1, 2)$. Applying a left-hand circular polarized light with wavelength proportional to the energy difference between $5^2S_{1/2}$ and $5^2P_{1/2}$, (D_1 line in Figure 2.4), which is approximately 795nm for Rubidium, excites the atoms to one of the m_F states of $5^2P_{1/2}$. Naturally, they will be de-excited, but their original m_F number will increase by +1. These cycles of exciting and de-exciting will continue, and the m_F number will increase each time. Once the atom's m_F number reaches $m_F = 2$, that atom will no longer absorb the left-hand circular polarized light. After a certain amount of time, most of the atoms will be in the $m_F = 2$ state. At that point, we can say that the Rb atoms are optically pumped and their magnetic moments are aligned with the applied magnetic field. In other words, the atoms are polarized. Figure 2.5 shows the behavior of atoms during the left-hand-polarized light excitation.

The Rb atoms will stay in the pumped state for a while. Then, due to collision with other atoms and walls of the encapsulating cell, they will lose their polarization, and that is referred to as relaxation. Many factors contribute to the relaxation time constant, buffer gases and cell coatings are the most critical, [48, 132]. The buffer gas is the third atom species we introduce in the cell. Usually, the nitrogen gas is used. It serves the purpose of reducing the collisions between Rb atoms, which increases the relaxation time constant. As for cell anti-relaxation coating, Rubidium Hydride increases the relaxation time constant by a factor of four, [67, 68]. In general, those relaxation time constants are on the order of milliseconds.

Next, we will introduce the spin-exchange process that transfers the alkali metal polarization to Xe atoms.

2.5 Spin Exchange

Now that all of the Rb atoms are pumped, their spin state needs to be transferred to Xe atoms. The spin-transfer occurs according to the conservation of angular momentum law, where the angular momentum, or spin, can be transferred between particles but the total angular momentum is preserved, [129]. There are two mechanisms of spin transfer (spin-exchange), either by direct collision or by forming of temporary Van Der Waals molecules. In Direct collision, as the name implies, a Xe atom and a Rb atom collide and the spin-exchange happens. Figure 2.6-(a) shows the spin-exchange due to a direct collision. This direct contact, however, has a small chance of occurrence, [7]. On the other hand, Van Der Waals molecules formed as a result of buffer gas presence, which brings Xe and Rb atoms closer to each other and increases the interaction time between them, as shown in Figure 2.6-(b), [124]. The formation of Van Der Waals molecules contributes to a higher chance of spin-exchange. After the spin exchange takes place, the Rb atoms can absorb light

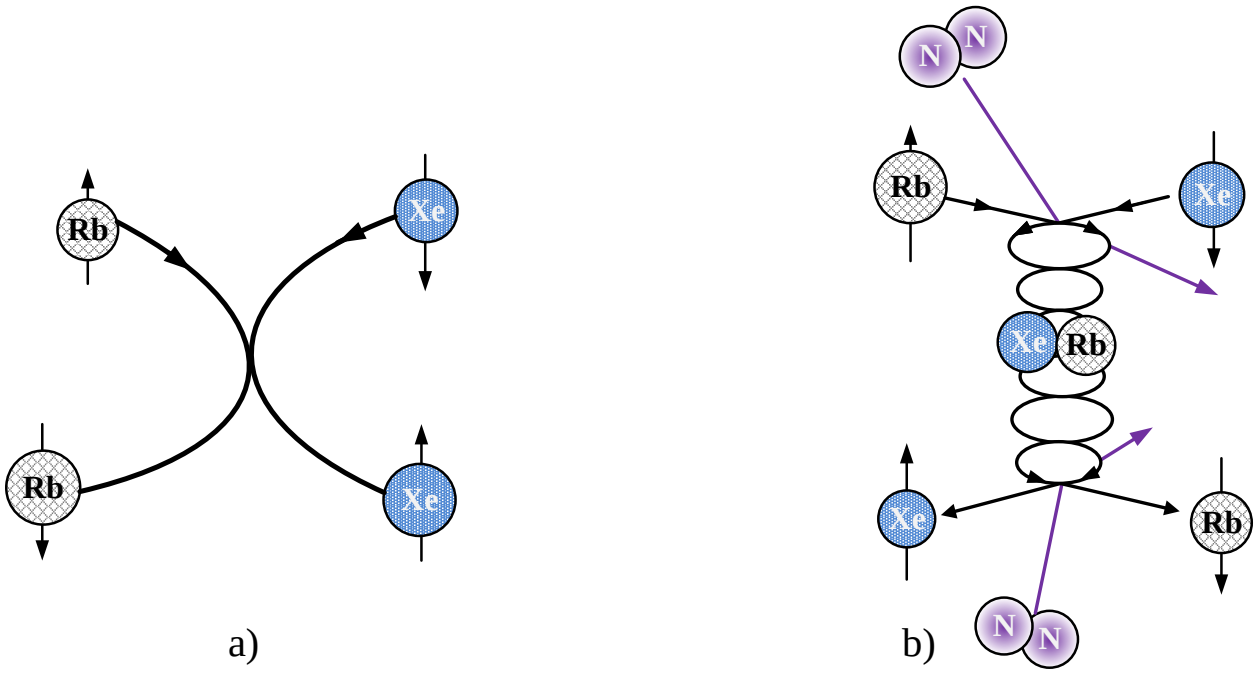

Figure 2.6: Sketch showing two mechanisms for spin exchange, a) Direct collision spin exchange of two particles with different initial spin, b) Van Der Waals spin exchange of Xe and Rb in the presence of N_2. The illustration is adopted from [49]

again and the optical pumping is repeated.

Since the Xe atoms are now polarized, if we rotated the frame of reference, Xe atoms will be able to measure rotation. The rotational information is in the magnetic field of those atoms. Multiple solutions can be used to measure those fields, SQUID is one option. Another option is placing an atomic magnetometer near the cell; as in [25]. And a third option is integrating the magnetometer in the same cell that contains the Xe atoms, which was demonstrated on a large scale in [26]. The integrated atomic magnetometer was reported to have an enhancement factor of 500x, if compared to a coil near the cell, [81].

Next, we will discuss the integrated atomic magnetometer and present two possible implementations of that magnetometer.

2.6 Integrated Atomic Magnetometer

Let us assume the spin-exchange optical pumping took place and the Xe atoms are now aligned and their magnetic moments $\vec{\mu}_I$ have added up together. The collective magnetic moments of all Xe atoms can be considered as a magnetization vector $\vec{M}_{Xe}$. We will discuss the behavior of this vector in an external field in more details in section 2.7.1.

$$\vec{M}_{Xe} = \sum \vec{\mu}_I \tag{2.23}$$

We assume our applied magnetic field $\vec{B}_0$ is in the $\hat{z}$-direction, which means that the magnetization vector will be pointing towards the $\hat{z}$-direction with a negligible component in the xy-plane as shown in Figure 2.7-(a). The xy-plane component of the magnetization vector $\vec{M}_{Xe}$ contains the rotational information. So, in order to maximize the detected signal, we need to deflect the magnetization vector $\vec{M}_{Xe}$ towards the xy-plane. Deflecting $\vec{M}_{Xe}$ towards the xy-plane can be carried out by applying an AC magnetic field, let us call it B_1, with a small amplitude and a frequency almost equal to the Larmor frequency of Xe signal, which was defined by equation (2.7). The direction of the AC field can be either along the $\hat{x}$-axis or $\hat{y}$-axis (for consistency of this discussion, we will assume the AC field is along the $\hat{x}$-axis, as shown in Figure 2.7-(b)). This field brings the Xe atoms' precession in phase, which maximizes the magnetization vector component in the xy-plane.

Now the magnetization vector has a component in the xy-plane (M_{xy}), we can measure the magnetic field produced by the Xe atoms. The Rb atoms in the cell will be used to transfer the spin from Xe atoms using the spin-exchange principle discussed in Section 2.5. To measure the spin of the Rb atoms, we can use one of two configurations: the Dehmelt detection, or the Faraday detection.

Next, we will explain the two methods and discuss advantages and disadvantages of

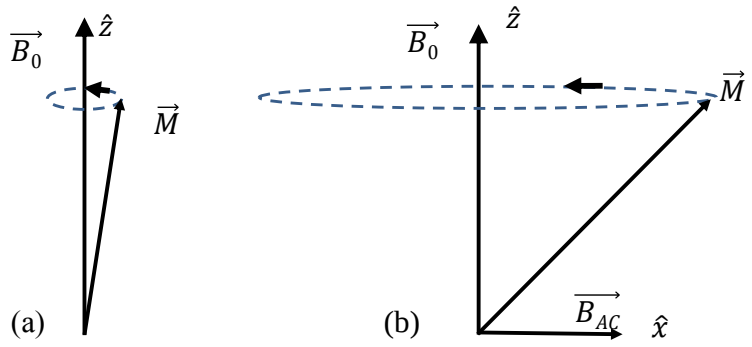

Figure 2.7: Xe magnetization vector with and without AC field

each method.

2.6.1 Dehmelt Detection

The setup now consists of a circularly polarized light to pump the atoms, a DC magnetic field $\vec{B_0}$ applied along the $\hat{z}$-axis that forms a magnetization vector $\vec{M}_{Xe}$, an oscillating magnetic field $\vec{B_1}$ along the $\hat{x}$-axis to deflect the magnetization vector. The applied DC magnetic field causes the Rb atoms to precess as well. However, their precession rate is typically at higher frequencies since their gyromagnetic ratio (γ_{Rb}) is three orders of magnitude higher than Xe. An RF field $\vec{B_C}$ with a frequency equal to the precession frequency of Rb is applied along the $\hat{z}$-axis and is used as a carrier magnetic field. The carrier magnetic field improves the signal-to-noise ratio by achieving the hyperfine interaction enhancement factor between Xe and Rb, [44]. Next, we will apply a circularly polarized light at 795nm along the $\hat{x}$-axis (probe light), and place a photo-detector right after the cell.

The Xe magnetization vector $\vec{M}_{Xe}$ has a component precessing in the xy-plane, and the Rb atoms are following that due to the spin-exchange. Looking from the $\hat{x}$-axis through the cell, we will be observing as if the magnetization vector is shrinking in $+\hat{x}$-direction and growing in -$\hat{x}$-direction, then shrinking in -$\hat{x}$-direction and growing in $+\hat{x}$-direction, and so

on. As the magnetization vector shrinks in $+\hat{x}$-direction, it appears to be un-pumped, and the circularly polarized light in the $\hat{x}$-direction will be absorbed, and when the magnetization vector flips its direction, it appears to be pumped so that the light will pass through. The light intensity hitting the photo-detector will be proportional to the x-component of the magnetization vector (M_x) rotation, [29].

The advantages of this detection scheme are that it requires only a single photo-detector for the probe beam, and it is possible to use the same laser source for pumping and probing. However, partially pumping the atoms by probe beam along the $\hat{x}$-direction alters the Rb polarization, which creates a magnetic gradient inside the cell. This gradient has a direct effect on the Xe atoms. Lowering the probe beam power reduces its interference with Rb atoms polarization. However, the signal would be limited by the photon shot noise, [33].

2.6.2 Faraday Detection

The Faraday detection setup is similar to the Dehmelt setup, but with a few differences. The setup consists of a circularly polarized light to pump the atoms, a DC magnetic field $\vec{B_0}$ applied along $\hat{z}$-axis to form the magnetization vector $\vec{M}_{Xe}$, an oscillating field applied to the $\hat{x}$-axis to deflect the magnetization vector, and a carrier field applied along the $\hat{z}$-axis to improve the signal-to-noise ratio. In the Faraday detection scheme, the probe beam is linearly polarized, a polarizing beam splitter and two photo-detectors are required right after the cell. Figure 4.13 shows the characterization setup utilizing the Faraday detection. The linearly polarized probe light enters the cell with a certain polarization angle, that angle changes as a result of the magnetic field as seen in Figure 2.8, [97].

We choose a wavelength that can interact with the Rb atoms, so the output signal is proportional to the Rb magnetic field. Linearly polarized light can be considered as two circular polarized light components added together with opposite handedness and different

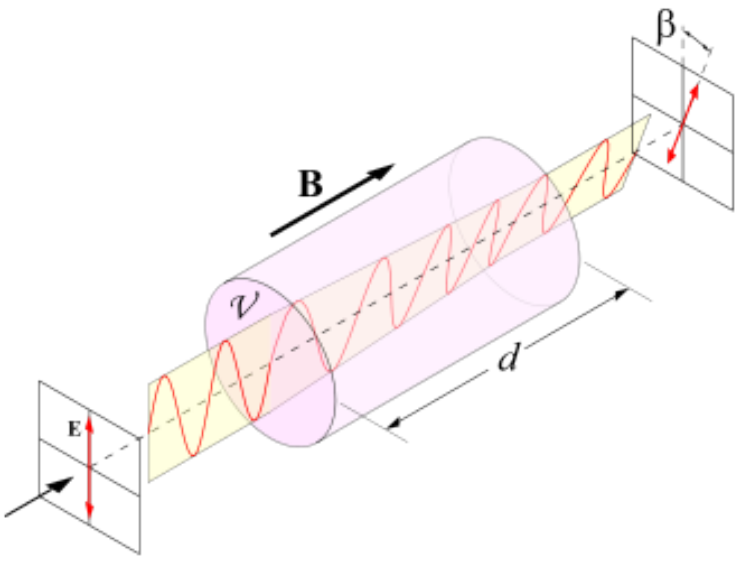

Figure 2.8: The Faraday rotation principle, initial polarization changes proportional to the magnetic field. Adopted from [87].

phase. Depending on the initial relative phase between the two components, the polarization angle is defined, Figure 2.9. When that light passes through the Rb cell, each one of the two light components will experience a different refractive index, which will cause the two components to travel at different speeds. The difference in travel speed of the two components results in a change of the initial phase difference, which will show as a change in the polarization angle of the exiting beam. An expanded overview of the use of the Faraday detection in magneto-optical experiments can be found in [18] and in references within.

The main advantage of the Faraday detection is that it sends a linear polarized light into the cell, which does not affect the Rb atoms as much as the circular polarized beam. As a result, a better performance was reported using the Faraday detection, [83, 64]. The disadvantage of such implementation is that it requires more optical components compared to the Dehmelt scheme, which makes it challenging when we try to reduce the NMR sensors size.

This was a brief review of the integrated atomic magnetometer, two detection schemes

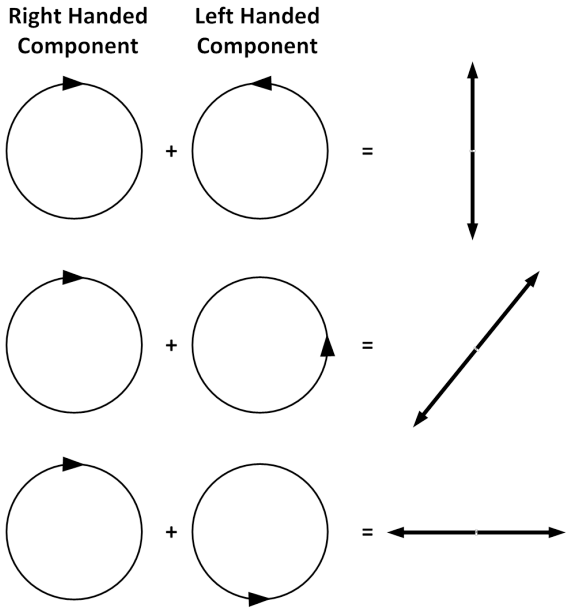

Figure 2.9: Relative phase difference between the left and the right handed components of the linear polarized light defines the polarization angle. Three cases are presented here in each case we observe polarization change as a result of the initial phase difference

were introduced and their advantages and disadvantages were discussed. A more detailed coverage of the topic can be found in [33].

2.7 NMR Sensors Dynamics

2.7.1 Bloch Equations

Bloch equations are a set of equations that model the interaction of the magnetization vector with magnetic fields [15]. When we introduced the magnetization vector, we assumed it is the summation of all the magnetic moments, equation (2.23). Since equation (2.6) describes the moments' motion, we can substitute equation (2.23) for equation (2.6) and we

obtain

$$\frac{d\vec{M}}{dt} = \vec{M} \times \gamma \vec{B}_0 \tag{2.24}$$

from now on we will talk about the Xe signal so we will omit the subscripts of $\vec{M}_{Xe}$ and γ_I. Equation (2.24) describes the rate of change of the magnetization vector in all three dimensions. We can expand this cross product to separate x, y, and z components.

$$\frac{dM_x}{dt} = \gamma(M_y B_z - M_z B_y) \tag{2.25}$$
$$\frac{dM_y}{dt} = \gamma(M_z B_x - M_x B_z) \tag{2.26}$$
$$\frac{dM_z}{dt} = \gamma(M_x B_y - M_y B_x) \tag{2.27}$$

Our assumption is $\vec{B}_0$ is in the $\hat{z}$-direction, so we can say $B_z = B_0$ in equation (2.25) and

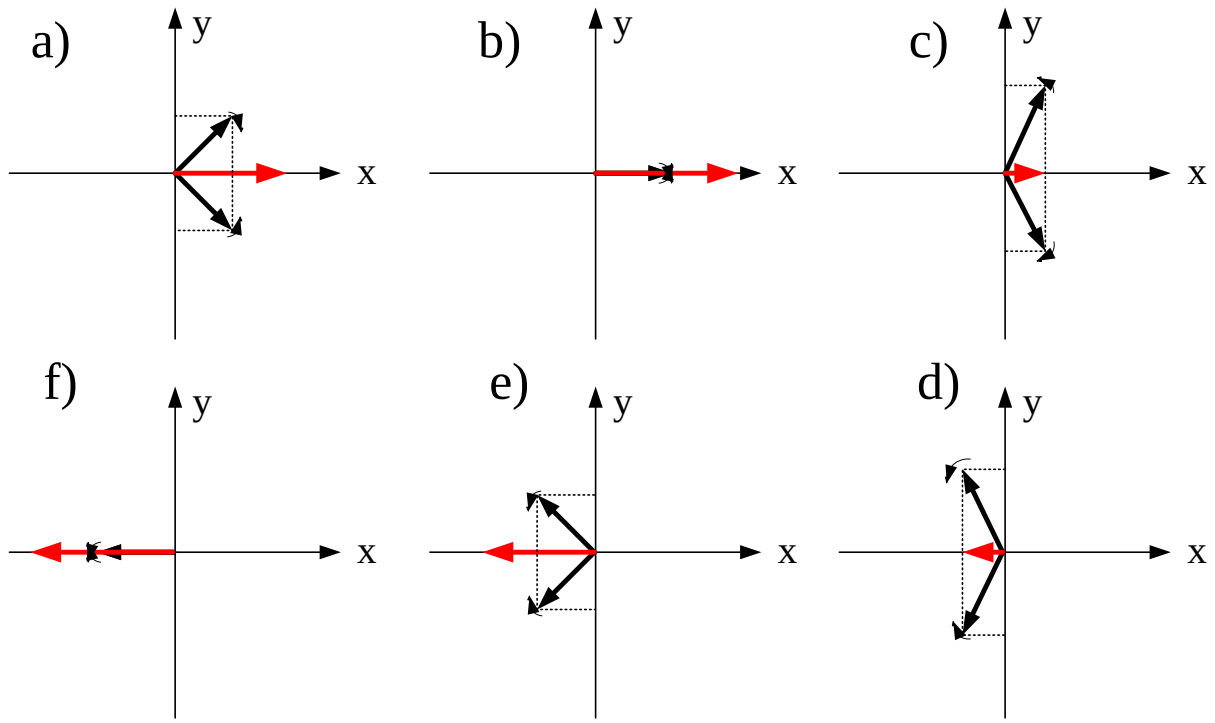

Figure 2.10: Oscillating field applied along the $\hat{x}$-axis can be visualized as two static fields rotating in opposite direction around the z-axis

equation (2.26). The oscillating filed $\vec{B_1}$ applied on the $\hat{x}$-axis can be visualized as two static fields rotating around z-axis in opposite directions, where the x-components add up and the y-components always cancel out, as illustrated in Figure 2.10. The x-component for both fields is $B_x = B_1 cos(\omega_a t)$, while the y-component for the clockwise field is $B_y = -B_1 sin(\omega_a t)$ and for the counter-clockwise is $B_y = B_1 sin(\omega_a t)$. Using the clockwise vector, along with our assumption $B_z = B_0$, we can re-write equations (2.25), (2.26) and (2.27) as follows

$$\frac{dM_x}{dt} = \gamma[M_y B_0 + M_z B_1 sin(\omega_a t)] \tag{2.28}$$

$$\frac{dM_y}{dt} = \gamma[M_z B_1 cos(\omega_a t) - M_x B_0] \tag{2.29}$$

$$\frac{dM_z}{dt} = -\gamma[M_x B_1 sin(\omega_a t) + M_y B_1 cos(\omega_a t)] \tag{2.30}$$

To simplify the set of equations (2.28), (2.29) and (2.30), we will introduce a rotating

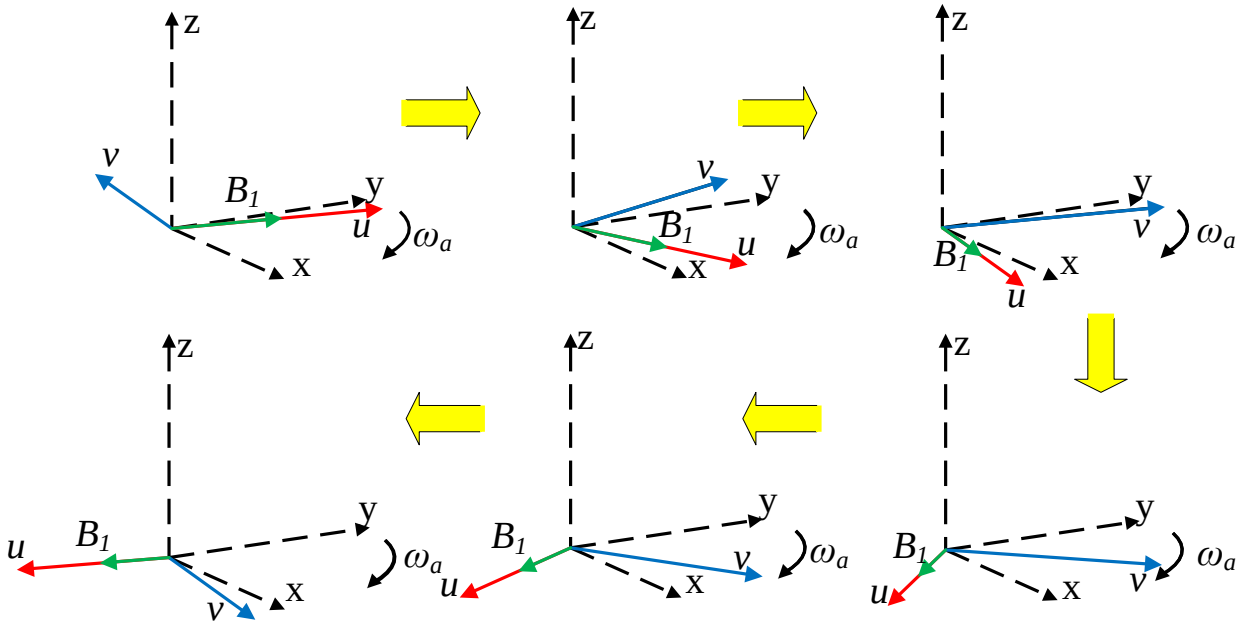

Figure 2.11: Rotating coordinate frame concept

coordinates system that rotates around the z-axis (u, v). Where u rotates in phase with B_1 and v is in quadrature with B_1. Figure 2.11 illustrates the concept of the rotating coordinate

frame. M_x and M_y are defined as

$$M_x = \quad u\cos(\omega_a t) + v\sin(\omega_a t) \tag{2.31}$$

$$M_y = \quad -u\sin(\omega_a t) + v\cos(\omega_a t) \tag{2.32}$$

The Bloch equations in the rotating coordinates becomes

$$\frac{du}{dt} = \quad \Delta\omega v \tag{2.33}$$

$$\frac{dv}{dt} = \quad -\Delta\omega u + \gamma B_1 M_z \tag{2.34}$$

$$\frac{dM_z}{dt} = \quad -\gamma B_1 v \tag{2.35}$$

where $\Delta\omega = \gamma B_0 - \omega_a$ is the mismatch between the applied oscillating field and the Larmor frequency of the Xe atoms. In the case of NMR gyroscope, if we apply a rotation rate to the system ω_R, then $\Delta\omega = \gamma B_0 - \omega_a \pm \omega_R$. In the case of NMR magnetometer, if we apply an external magnetic field δB_z, then $\Delta\omega = \gamma B_0 - \omega_a \pm \gamma\delta B_z$. Before we proceed with the solution to the above equations, we need to consider an important property of the magnetization vector, which is the relaxation.

2.7.2 Relaxation

As mentioned in section 2.4, Rb atoms lose their polarization due to collision with other atoms and with the cell walls, and we referred to that as relaxation. A similar phenomenon acts on the Xe atoms, however, the relaxation time constant for Xe atoms is 3-4 orders of magnitudes larger than Rb. Xe atoms have two relaxation constants that describe the Xe magnetization vector. The first relaxation time constant is identified as the longitudinal relaxation time constant T_1, and it is a measure of the time required for the M_z to return to the equilibrium condition of $M_z = M_0$. If we managed to flip the magnetization vector

direction such that it points to the -$\hat{z}$-direction instead of +$\hat{z}$-direction, then the rate of return to its original direction is governed by T_1. The other relaxation time constant is called the spin-spin or transverse relaxation time T_2, and it is a measure of how fast the M_{xy} will go to 0 once we stop the oscillating field. Collision of Xe atoms with the wall affects the longitudinal relaxation time T_1, while the magnetic field gradients across the cell disrupt the coherence of the Xe atoms, which reduces the transverse component of the magnetization vector and hence T_2, [123]. If there was a magnetic field gradient across the cell, that will mean different groups of atoms will be experiencing different net magnetic field, which leads to different Larmor precession frequencies of those atoms, [22, 23, 76]. When we try to sum up the magnetization components of those atoms, we find that T_1 is the upper limit for T_2. To model these effects we can write changes of the magnetization vector components due to each relaxation constant as

$$\frac{dM_x}{dt} = -\frac{M_x}{T_2} \tag{2.36}$$

$$\frac{dM_y}{dt} = -\frac{M_y}{T_2} \tag{2.37}$$

$$\frac{dM_z}{dt} = -\frac{M_0 - M_z}{T_1} \tag{2.38}$$

We then account for those effects in the set of equations (2.28), (2.29) and (2.30) directly. Then using the rotating coordinates we obtain the Bloch equations in the rotating frame:

$$\frac{du}{dt} = \Delta\omega v - \frac{u}{T_2} \tag{2.39}$$

$$\frac{dv}{dt} = -\Delta\omega u + \gamma B_1 M_z - \frac{v}{T_2} \tag{2.40}$$

$$\frac{dM_z}{dt} = -\gamma B_1 v + \frac{M_0 - M_z}{T_1} \tag{2.41}$$

For small changes in the magnetic field (either due to input rotation ω_R for NMRG or due to external magnetic field δB_z for NMRM) we can assume that there is no change in $u,\ v,\ M_z$ with respect to time and we then set the equations (2.39), (2.40) and (2.41) equal to zero

and solve. The analytical solution is found to be [15]

$$u = M_0 \frac{\gamma B_1 T_2^2 \Delta\omega}{1 + (T_2\Delta\omega)^2 + (\gamma B_1)^2 T_1 T_2} \tag{2.42}$$

$$v = M_0 \frac{\gamma B_1 T_2}{1 + (T_2\Delta\omega)^2 + (\gamma B_1)^2 T_1 T_2} \tag{2.43}$$

$$M_z = M_0 \frac{1 + (T_2\Delta\omega)^2}{1 + (T_2\Delta\omega)^2 + (\gamma B_1)^2 T_1 T_2} \tag{2.44}$$

The applied input to the NMR sensor (either a rotation to the NMRG or an external magnetic field to the NMRM) results in shift in the frequency $\Delta\omega$, and that can be found either from u which rotates in phase with oscillating field B_1 or from v which rotates in quadrature. A typical response of (v) and (u) due to changes in $\Delta\omega$ is shown in Figure 2.12. Note that u gives the direction of the sensor's input.

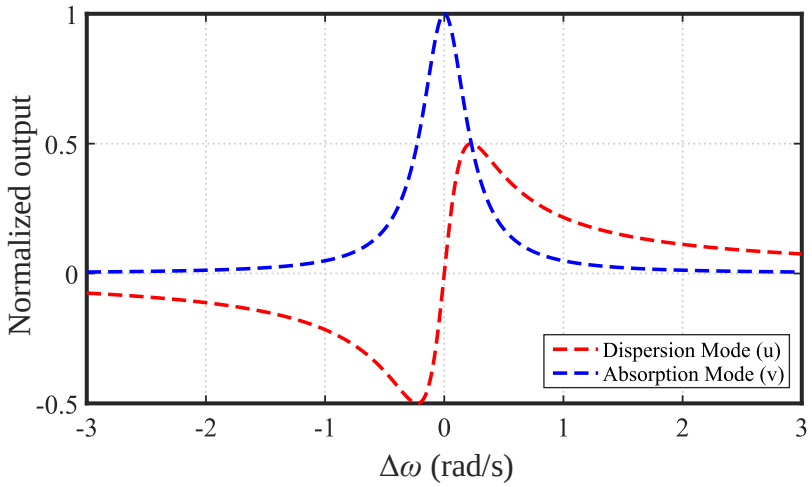

Figure 2.12: Typical normalized response of dispersion (u) and absorption (v) modes due to change in $\Delta\omega$, obtained from equation (2.42) and equation (2.43), respectively. T_1=10s, T_2=5s, γ= $2\pi\times 10\ rad.s^{-1}/\mu T$, $B_1 = 10nT$

2.8 Summary

This chapter summarized the principle of operation of Nuclear Magnetic Resonance gyroscopes and magnetometers. A short background using a simplified atom model was used to explain the mechanism of Nuclear Magnetic Resonance and how it can be utilized to measure different physical phenomena, rotation in the case of NMR gyroscopes, and external magnetic fields in the case of NMR magnetometers.

Figure 2.13 summarizes the operation of the NMR sensors. A spin-exchange optical pumping (SEOP) process is used to align Xe atoms, Figure 2.13-(a), [124]. In this process, a circularly polarized light beam polarizes (pumps) the Rb atoms. Circularly polarized light is fundamental for the optical pumping process because it has the angular momentum which can change the quantum state of the outer electrons of the Rb atoms to reach the pumped state ($m_F = -2$ or $m_F = 2$ by the right or left-handed polarized light, respectively), [33]. Then, direct collisions and formation of Van Dar Waals molecules (spin-exchange) transfer the polarization from Rb atoms to Xe atoms. This process adds up the magnetic moments of Xe atoms to form a net magnetization vector. An applied oscillating field B_1 at Larmor frequency along the x-axis synchronizes the atoms in phase so that the effective magnetization vector precesses around the B_0 magnetic field with a frequency ω_L, equation (2.7), Figure 2.13-(b).

For the NMR gyroscope, when a rotation rate of ω_R is applied to the whole system, the new observed frequency of the magnetization vector precession becomes

$$\omega'_{obs} = \omega_L \pm \omega_R \tag{2.45}$$

This phenomenon is illustrated in Figure 2.13-(c). The behavior of the Xe magnetization vector is transferred to the ensemble of Rb atoms through the same process of spin-exchange.

Subsequently, the Rb atoms are detected via a linearly polarized light. The rotational rate can be extracted from the frequency measurements.

The principle of operation for NMR magnetometer is similar to that of the NMR gyroscope. However, instead of detecting the applied rotational rate ω_R, NMR magnetometers detect the changes in the magnetic field along the z-axis, Figure 2.13. The observed frequency of the magnetization vector becomes

$$\omega'_{obs} = \gamma(B_0 \pm \delta B_z) \tag{2.46}$$

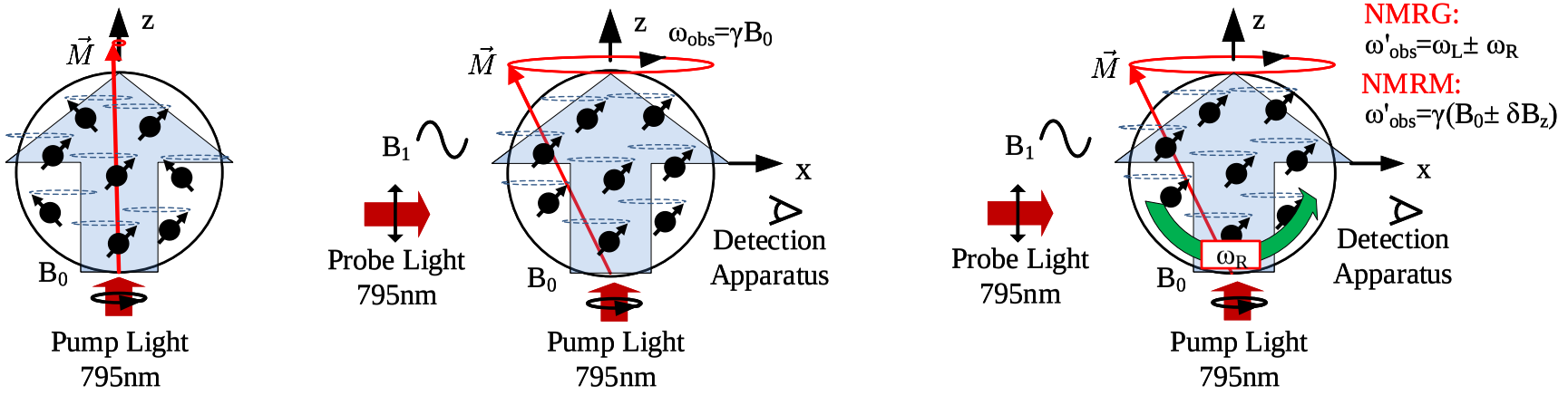

Figure 2.13: Principle of operation of Nuclear Magnetic Resonance Gyroscopes and Magnetometers. The illustration is adopted from [33].

Chapter 3

MEMS Components for NMR Atomic Sensors

In this chapter a miniaturization method for NMR atomic sensors based on the micro-fabrication of NMR sensors components on a wafer-level is introduced. We also discuss and analyze the contribution of fabrication imperfections to the overall performance of NMR atomic sensors. In Section 3.1, the essential building blocks of atomic sensors are listed. Section 3.2 presents a suggested miniaturized implementation of NMRG and NMRM using the micro-fabrication techniques. Section 3.3 presents an analytical model supported by experimental evaluation of sources of the fabrication imperfections. Finally, Section 3.4 talks about the projection of assembly errors on the device performance based on the developed model.

3.1 Essential Building Blocks

In this section, an overview of the essential building blocks required for realization of NMR-based systems is presented.

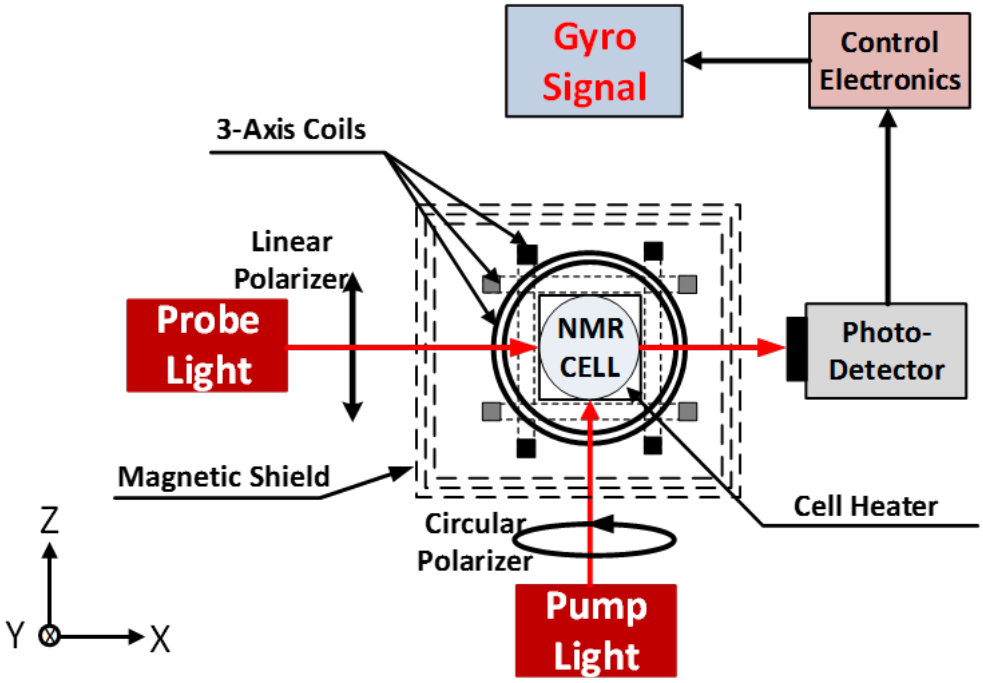

Figure 3.1: Functional Elements of Nuclear Magnetic Resonance Gyroscope

Figure 3.1 shows a diagram of the components required for NMR sensors. The atomic vapor cell is in the heart of the NMR sensors and encloses the noble gas and the alkali metal atoms. Alkali metals are usually in a solid-state at the room temperature and a cell heater is needed to raise temperature in order to vaporize the metal. Vaporization leads to increase in the alkali vapor density. Multi-axis magnetic field coils are needed to apply the static magnetic field B_0 along one axis, the oscillating field B_1 along a perpendicular axis, and an additional field along the third axis might be needed to cancel any residual fields inside the cell. Light sources and photo-detectors are needed for pumping and detecting the precessing alkali atoms. Optics, such as mirrors, lenses, and linear and circular polarizers are required to collimate the light, ensuring a proper polarization of the beams (circular and

linear polarization for the pump and probe beams, respectively). NMR sensors are sensitive to small magnetic fields, on the order of nano-Tesla. Knowing that the surrounding fields, such as the Earth's magnetic field, can be 3 to 4 orders of magnitudes larger, an NMRG requires a magnetic shield to eliminate those ambient fields. In the case of NMRM, no magnetic shield would be typically used. Finally, a set of control electronics that controls the fields and extracts the precession of the magnetization vector from the photo-detector signal is necessary, [45].

3.2 Miniaturization

In this section, we introduce our implementation of NMR sensors. We start with an approach for combining the 3-D folded MEMS and micro-glass blowing techniques. Next, we introduce the fabrication processes of each component and demonstrate fabricated prototypes. Our miniaturized implementation of NMR atomic sensors is sketched in Figure 3.2. The atomic cell is a glassblown micro-sphere filled with Rb, Xe, and buffer gases, for example N_2 and Ne. The cell is positioned on top of a cell heater and surrounded by two orthogonal pairs of Helmholtz coils. This assembly is encapsulated by a foldable backbone structure that houses 2 VCSEL's and 2 photo-detectors, all connected by through-wafer-vias to the outer-side of the backbone structure. Four 45° reflectors are included in the design of the backbone structure that route the light beams from VCSEL's through the cell to the photo-detectors. A 4-layer μ-metal shield protects the sensor from surrounding magnetic interferences (not shown).

Our approach starts with fabrication of a backbone, which is a double-folded structure with integrated reflectors and Helmholtz coils on a flat silicon wafer, Figure 3.3-(a). Then, the metallic reflectors are folded, and subsequently the coils are assembled in the middle of the backbone structure, Figure 3.3-(b). Next, the atomic cell is assembled in the middle

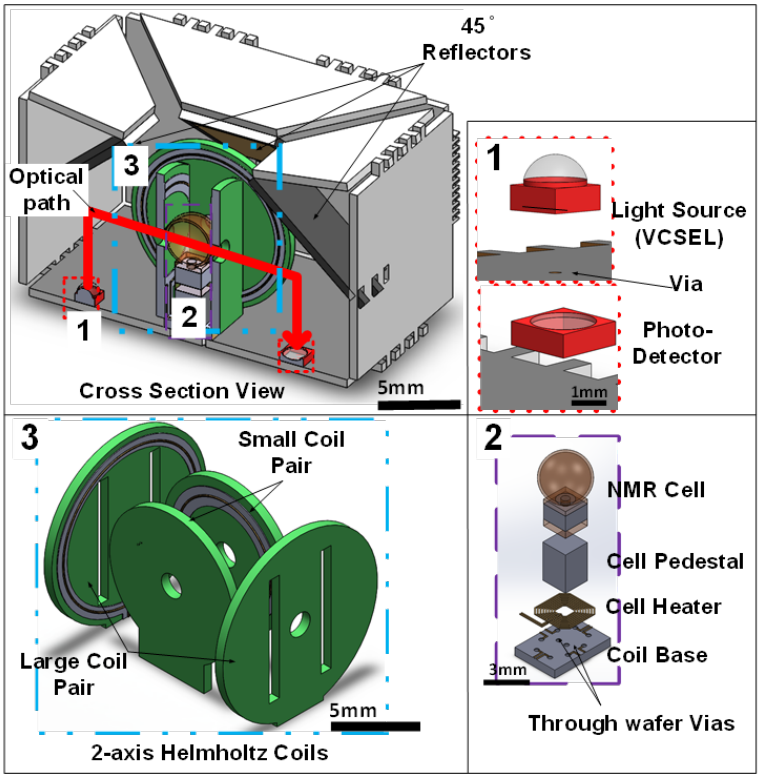

Figure 3.2: An implementation of NMR atomic sensors

of the folded Helmholtz coils, Figure 3.3-(c). After folding the coils, two Vertical Cavity Surface Emitting Lasers (VCSEL) and two photo-detectors are assembled, Figure 3.3-(d, e). The backbone structure is finally folded and placed inside multi-layer magnetic shields, Figure 3.3-(f, g). The fabrication process and the design descriptions for each of these components are discussed next.

The assembly of the folded coil and the glassblown cell in the middle of the folded structure is achieved via pick and place technique. Several alternative folding approaches were also explored, including a self-assembly triggered either by light, magnetic field, or resistive heating actuation of shape memory polymers, [77, 88, 38]. However, due to compatibility issues of those polymers with our wafer-level process and the sensor operation, we adopted a guided assembly technique using a folding mold, Figure 3.4. This folding method is compatible with a wafer-level assembly process.

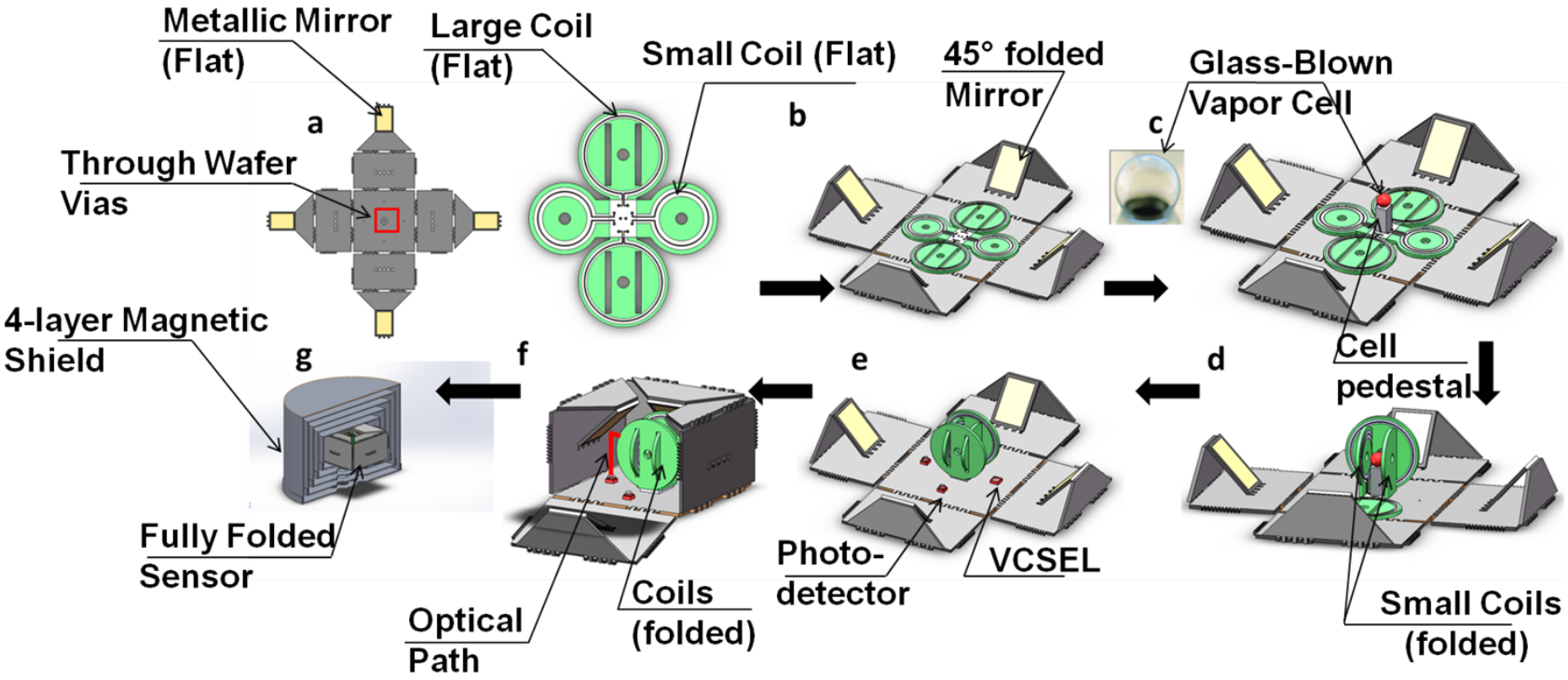

Figure 3.3: Conceptual drawing of the folded micro-NMRG. (a) Double-folded structure and coils fabricated on a flat wafer, (b) Initial folding of backbone structure with co-fabricated mirrors, (c) Assembly of glassblown micro cell, (d) Coils are folded, (e) VCSELs and photo-detectors are assembled, (f) Backbone structure is fully folded, (g) The sensor is placed inside magnetic shields (a cross-section view of the shields)

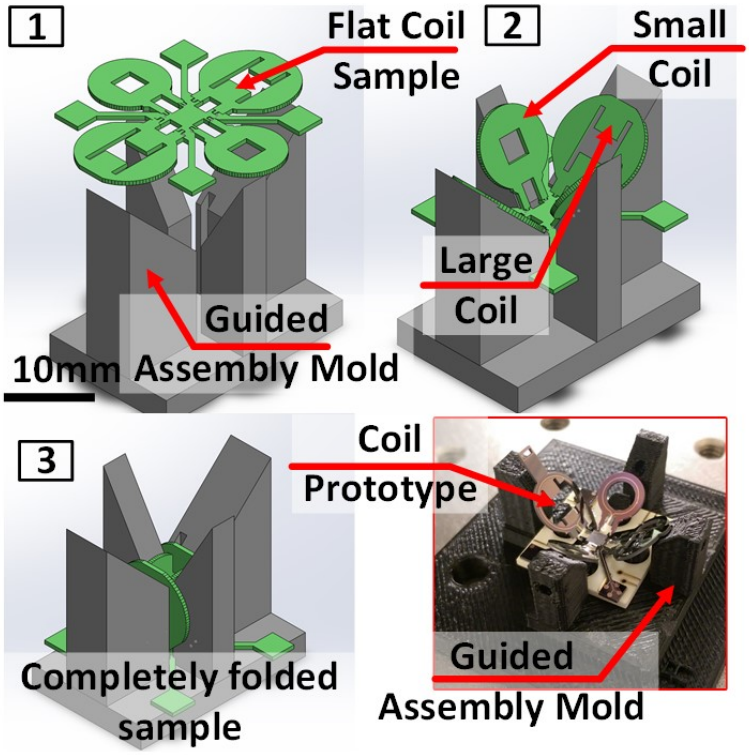

Figure 3.4: Sketch of the guided assembly process of the folded Helmholtz coils using a pre-defined mold, insert: a picture of a coil's sample inside a folding mold prototype created using 3D printing

3.2.1 Folded Helmholtz Coils and Integrated Cell Heater

The fabrication process of the folded coils with integrated cell heater starts with a 500μm silicon wafer coated with 3000Å of LPCVD silicon nitride, Figure 3.5-(a). The first metal layer (metal-1) of the cell heater was defined by evaporating 500/5000Å Cr/Au, followed by photo-lithography and wet metal etching using Cr TFE and Au GE8110 etchants from Transene Company for etching Cr and Au, respectively, Figure 3.5-(b). Note that a lift-off process can be used on this step. Next, a 14μm parylene film was deposited on top of metal-1, and subsequently etched using reactive ion etching (RIE) with a 1000Å Ti film as the hard mask, forming the flexible hinges, Figure 3.5-(c),[106]. Metal-2 was an evaporated and patterned 500/2500Å Cr/Au layer to form the Helmholtz coil traces, as shown in Figure 3.5-(d). Finally, the coils and hinges were defined using photo-lithography, followed by RIE-

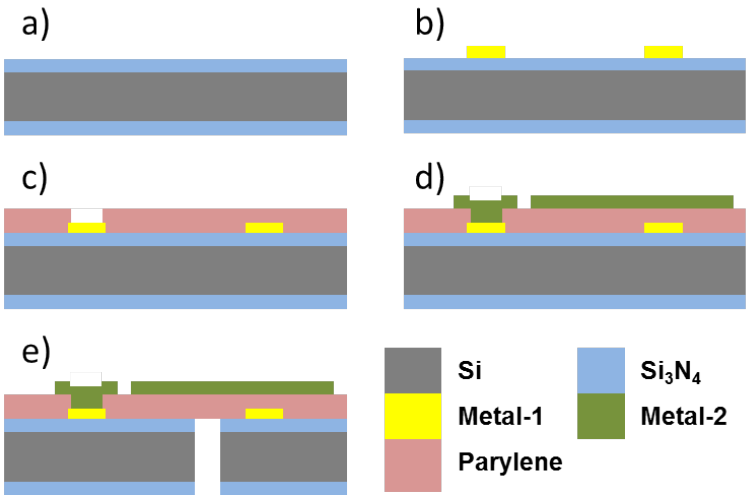

Figure 3.5: Fabrication process of the folded Helmholtz coils

DRIE-RIE etching sequence of the Si_3N_4-Si-Si_3N_4 layers, respectively, starting from the backside of the wafer, Figure 3.5-(e).

The generated field by an ideal Helmholtz coil at the center of the coil along the axis is a superposition of the field generated by two current loops separated by a distance equal to the radius of a single loop, [46],

$$B_z = \frac{\mu_0 N I R^2}{2\left[(z - R/2)^2 + R^2\right]^{3/2}} + \frac{\mu_0 N I R^2}{2\left[(z + R/2)^2 + R^2\right]^{3/2}}, \tag{3.1}$$

where μ_0 is the air permeability, N is the number of turns, R is the coil's radius. The field homogeneity is defined as

$$\eta_{B_z(ppm)} = \frac{\Delta B_z}{B_0} \times 10^6, \tag{3.2}$$

where ΔB_z is the difference between the field maximum and minimum across the cell, B_0 is the field value at the center of the coil.

The trade-offs in the coil's design are the size and homogeneity, both can be determined by the radius of the coil according to equations (3.1) and (3.2). The field homogeneity improves as the coil's radius increases relative to the cell. However, for a 1mm cell, a

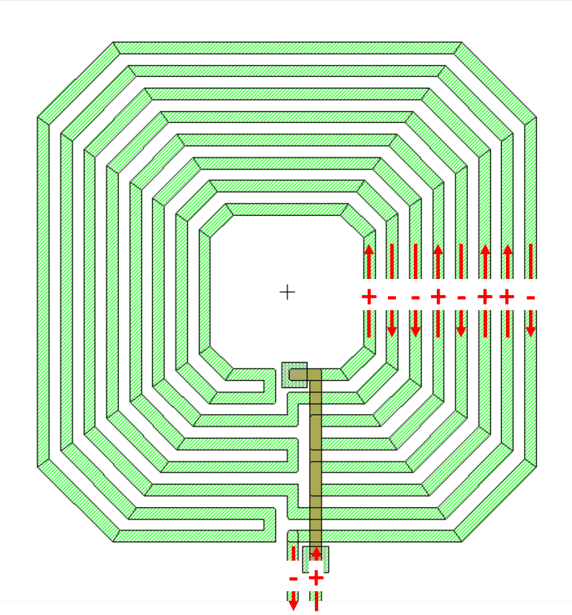

Figure 3.6: Heater layout illustrating the (+–+-++-) configuration. Sign convention, (+) is for counter clockwise and (-) for clockwise flow of current in the heater traces, [21].

coil of radius above 5mm does not provide a significant improvement in the magnetic field homogeneity, but increases volume of the coil, [46]. For example, homogeneity of an ideal Helmholtz coil with the radii of 3mm, 5mm, and 6mm across 1mm cell would be around 860ppm, 113ppm, and 55ppm, respectively. A coil of radius of 4.2mm was chosen for our design. The heater design utilized a multi-pole current carrying conductors with (+ - - + - + + -) configuration, illustrated in Figure 3.6. This created a 2^3 poles magnetic moment that resulted in a suppressed magnetic field from the heating current, [21]. In addition to using a magnetic field suppressing heater layout, a modulated heater current with a frequency of 100kHz was utilized (the frequency was intentionally selected far away from Xe resonance frequencies of ~100Hz to reduce an interference with Xe precession). The heater was placed 4.2mm below the cell and a thermally conductive micro-pedestal made from silicon was used to interface the cell to the heater. This distance was chosen to ensure placement of the cell at the center of symmetry coils and placement of the heater at the base of the coils, Figure 3.2-(2).

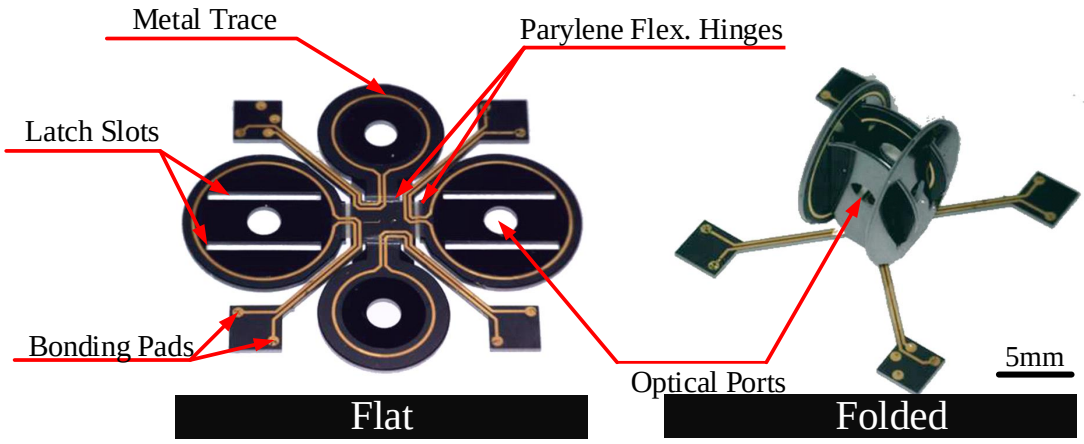

Figure 3.7: Fabricated sample of the folded Helmholtz coils: in the flat state (left), and in the folded state (right)

3.2.2 Folded Structure

The backbone of folded NMR sensors was fabricated using a process similar to the one used for coils, but with only one metal layer. The process is implemented on a 4-inch silicon wafer, but can be adopted for larger sizes. Flexible parylene hinges were defined on one side of the wafer, a metal layer of 500/5000Å Cr/Au was evaporated and patterned to form the metal reflectors on the other side of the wafer. The fabricated prototype of the double folded structure is shown in Figure 3.8, with one of the two optical paths illustrated.

The folded structure is the backbone of the sensor and the light reflectors integrated within. The design consideration is to provide four 45° reflectors in a compact design that route the pump and probe beams in and out of the cell. The angle of each reflector is determined by three panels that construct each side wall of the folded structure, the required relative angles between the panels to achieve 45° reflectors are listed in Table 3.1. The reflector panel was designed to be 8×6mm, to provide a mechanical support of the side wall and to ensure a large enough area for beam routing.

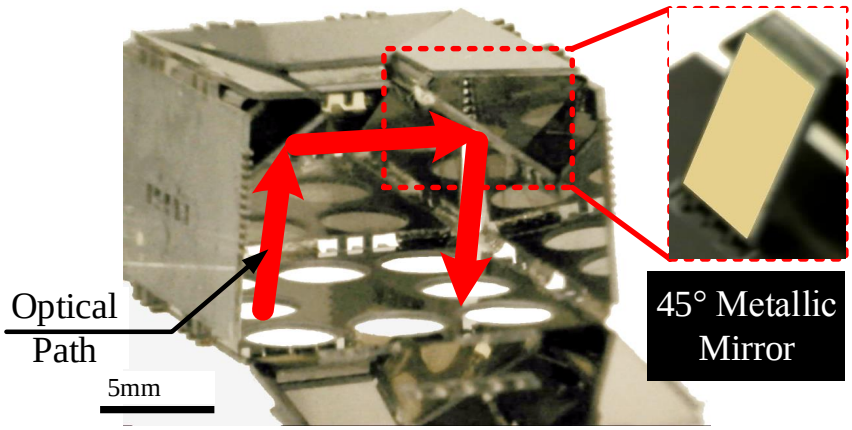

Figure 3.8: Fabricated folded structure with 45° metallic reflectors. Only one optical path is shown

3.3 Modeling and Experimental Evaluation

In this section, we introduce our analytical model for errors associated with 3D folding process, such as misalignment of components after folding and reinforcement against shock, vibration or thermal expansion. The analytical model was evaluated by experimental validation of each component. The fabrication process utilized lithography-based machining accuracy to define dimensions of the micro-components in 2-D. However, folding those components into a 3-D configuration introduced assembly errors. The considered components in this analysis were the folded Helmholtz coils and the double-folded backbone structure.

In calculating homogeneity, the volume of interest was a 1mm diameter glass-blown cell placed at the center of the two coils.

3.3.1 Folded Helmholtz Coil

Analytical Model

An Ideal Helmholtz coil consists of two identical current loops separated by a distance equal to the radius of each loop. Assuming there are two current loops perpendicular to the z-axis, with radius r_{coil} and their centers at locations of $(0, 0, -r_{coil}/2)$ and $(0, 0, r_{coil}/2)$. The field generated by this Helmholtz coil at any point (x,y,z) can be calculated using the Biot-Savart law as

$$\vec{B}_{HH}(x, y, z) = \vec{B}_1(x, y, z + r_{coil}/2) + \vec{B}_2(x, y, z - r_{coil}/2), \tag{3.3}$$

A model developed in [13] was adopted here to study the level of accuracy required for the folding process.

Misalignment errors in the structure are either due to the angular or linear shift of one current loop with respect to the other. To simplify the model, we assumed that the total misalignment is a superposition of angular and linear misalignments by each loop of the coil.

There are two angles of misalignment, as shown by the loop on the left of Figure 3.9: α_z is the angle of the loop with the y-axis and β_z is the angle with the x-axis. The loop's field due to the angular misalignments is

$$\vec{B}_1 = \vec{B}(u - u_0, v - v_0, w - w_0), \tag{3.4}$$

where $(\widehat{u}, \widehat{v}, \widehat{w})$ is a rotated coordinate frame and is related to the main frame $(\widehat{x}, \widehat{y}, \widehat{z})$ as

$$\begin{bmatrix} \widehat{u} \\ \widehat{v} \\ \widehat{w} \end{bmatrix} = \Big[T_z(\alpha_z, \beta_z) \Big] \times \begin{bmatrix} \widehat{x} \\ \widehat{y} \\ \widehat{z} \end{bmatrix}, \tag{3.5}$$

where T_z is the rotation matrix,[13], and is defined as

$$\begin{bmatrix} -\cos\beta_z & -\sin\alpha_z \ \cos\alpha_z \ \sin\beta_z & \cos^2\alpha_z \ \sin\beta_x \\ 0 & \cos\alpha_z & \sin\alpha_z \\ \cos\alpha_z \ \sin\beta_z & -\sin\alpha_z \ \cos\beta_z & \cos\alpha_z \ \cos\beta_z \end{bmatrix}, \tag{3.6}$$

where (u_0, v_0, w_0) is the center of the first loop projected on the rotated frame $(\widehat{u}, \widehat{v}, \widehat{w})$ and is defined as

$$\begin{bmatrix} u_0 \\ v_0 \\ w_0 \end{bmatrix} = \Big[T_z(\alpha_z, \beta_z) \Big] \times \begin{bmatrix} 0 \\ 0 \\ -r_{coil}/2 \end{bmatrix} \tag{3.7}$$

Assuming the second current loop is linearly shifted and its center is at $C_2'(x_0, y_0, z_0)$, as shown by the loop on the right in Figure 3.9. The generated field by the loop is then

$$\vec{B}_2 = \vec{B}(x - r_{coil}\Gamma_z \sin\psi_z, y - r_{coil}\Gamma_z \cos\psi_z, z - r_{coil}D_z - r_{coil}/2), \tag{3.8}$$

where D_z is a normalized mismatch in the z-direction, Γ_z and ψ_z are the shifts of coil's center C_2' along the y- and x-directions. In polar coordinates, the corresponding parameters can be defined as

$$D_z = \quad z_0/r_{coil} \tag{3.9}$$

$$\Gamma_z = \quad \tfrac{1}{r_{coil}}\sqrt{y_0^2 + x_0^2} \tag{3.10}$$

$$\psi_z = \quad \cos^{-1}\tfrac{y_0}{\sqrt{y_0^2+x_0^2}} \tag{3.11}$$

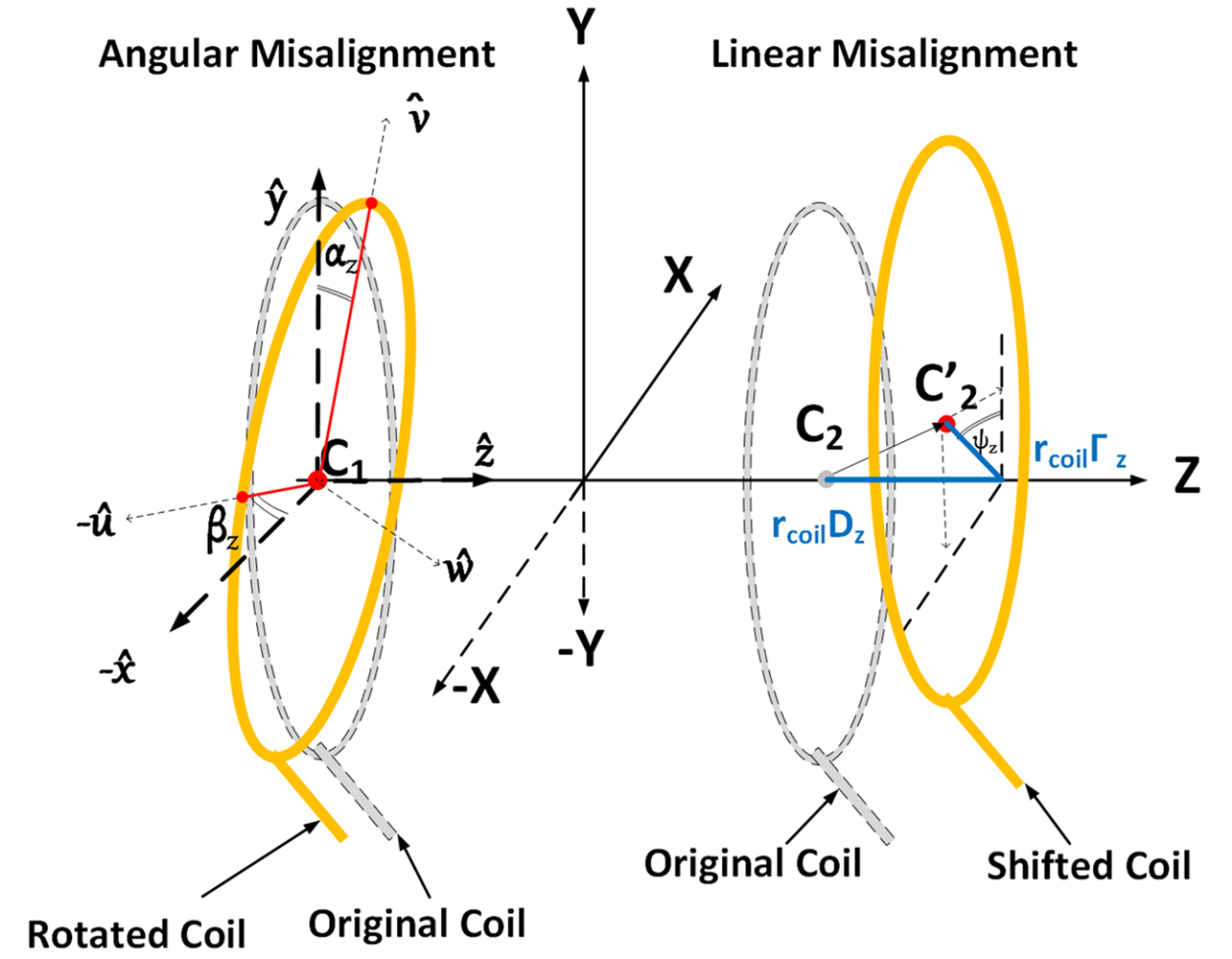

Figure 3.9: Sketch of angularly (left) and linearly (right) misaligned coils, (original location of the coils is illustrated with dashed lines and gray color)

From equations (3.4) and (3.8), the magnetic field of the misaligned Helmholtz coil becomes

$$\vec{B}_{HH}(x, y, z) = G_z \times \vec{B}_1 + \vec{B}_2, \tag{3.12}$$

where G_z is the transpose of T_z, which projects the field back to the main frame $(\widehat{x}, \widehat{y}, \widehat{z})$.

The homogeneity of the magnetic field along the z-direction is defined by equation (3.2).

The linear misalignment in the range from 0 to 1mm shows that the axial shift (along

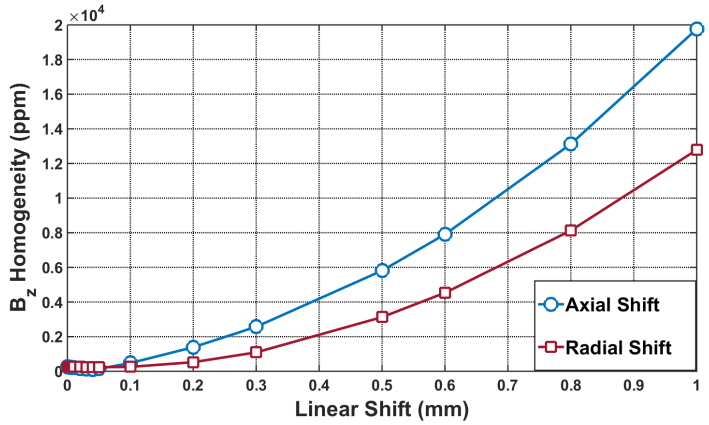

Figure 3.10: Analytical modeling of folded Helmholtz coils' homogeneity as a function of the linear shift in the axial (circular markers) and radial (square markers) directions

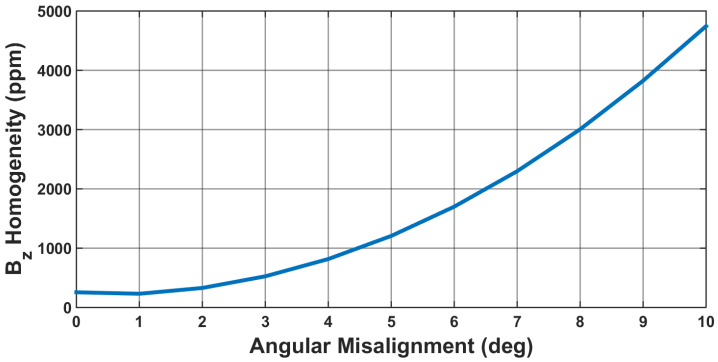

Figure 3.11: Analytical modeling of folded Helmholtz coils' homogeneity as a function of the angular misalignment along the x and y axes

the z-axis) has a larger impact on the homogeneity than the radial shift (along the x- and y-axis), Figure 3.10. The angular shifts α_z and β_z, on the other hand, show an identical effect on the field homogeneity in the z-direction, Figure 3.11.

Folded coils are defined by the locking slots at the bottom side and a locking latch at the top side, visible in Figure 3.2 and Figure 3.7. These components are typically defined with a few microns of tolerance. The folding is accomplished using a pre-defined mold for guided assembly, Figure 3.4. However, etching through a $500\mu m$ wafer introduces fabrication imperfections which could be up to $20\mu m$. This translates to 5 mrad angular misalignment or $20\mu m$ linear misalignment.

Projection of Imperfections to Performance

The resonance line width of Rb atoms in equations (2.42) and (2.43) is determined by the transverse relaxation time T_2, and they are related as, [33],

$$\Delta\omega = \frac{1}{T_2} \tag{3.13}$$

Optical pumping, spin exchange, spin destruction, and wall collisions are all the factors that contributes to broadening the resonance line, [110]. In addition, the field gradient inside the cell causes the Rb atoms to precess at different frequencies, which contribute to further broadening of the resonance line, [33]. By lumping all factors, except for the field gradient, and calling it $\Delta\omega_{setup}$, we can write the measured resonance line width $\Delta\omega_m$ as

$$\Delta\omega_m = \Delta\omega_{setup} + \Delta\omega_{gradient} \tag{3.14}$$

Now that the $\Delta\omega_{gradient}$ is known, equation (3.13) gives the relaxation time associated with the field gradient. The field gradient is then defined as

$$\Delta B_z = \frac{1}{\pi\gamma T_{2,gradient}} \tag{3.15}$$

Experimental Results

The experimental evaluation of this model was performed using a folded coil sample with the radius R_{coil}=3mm and a 2mm cubic cell. The sample was hand-folded which resulted in an angular, radial, and axial misalignments measured optically to be 5.2°, 0.87mm, and 0.6mm, respectively. The folded sample was placed inside a 4-layer magnetic shield with integrated 3 axes magnetic field coils (reference coils). The main field B_0= 4.7 μT was applied along the z-axis, that is the pump beam axis, and an RF field was applied along the

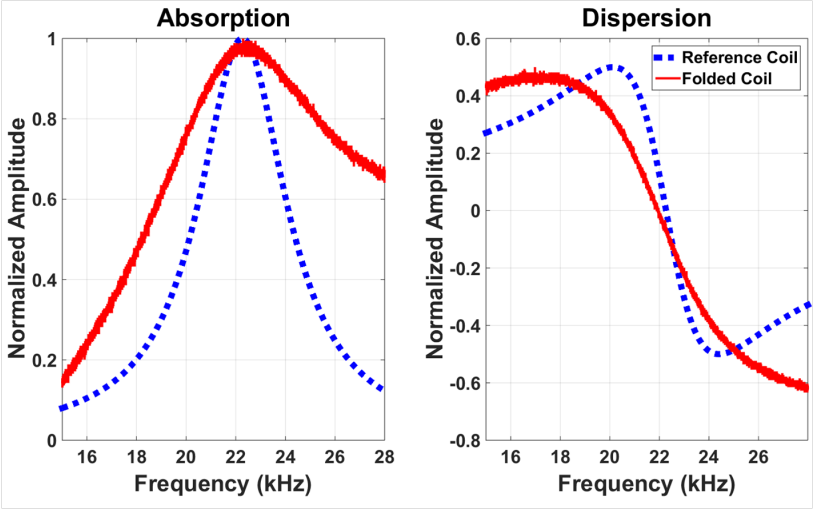

Figure 3.12: Normalized absorption and dispersion curves (experimentally measured) of both the folded coil sample (solid red) and the reference coil (dashed blue)

y-axis, which is the probe beam axis. The RF was swept from 15 kHz to 28 kHz to generate the Rb absorption and dispersion resonance lines.

First, the main field was applied using the reference coil to calculate $\Delta\omega_{setup}$ in equation (3.14), then repeated using the folded coil sample to estimate $\Delta\omega_{gradient}$. Figure 3.12 shows the normalized experimental curves for both cases. It was found that the broadening due to the field gradient was around 846Hz, which corresponded to the field non-homogeneity of $\eta_{B_z(exp)}$= 38585 ppm, according to equations (3.2), (3.13) and (3.15). The analytically estimated magnetic field non-homogeneity was derived to be $\eta_{B_z(model)}$= 37337 ppm, which is in a close agreement to what was measured experimentally. This result correlates to the optimal case with R_{coil}=4.2mm, N=5 turns, 1 mm cell. For the optimal case, we estimated non-homogeneity to be on the level of 345ppm.

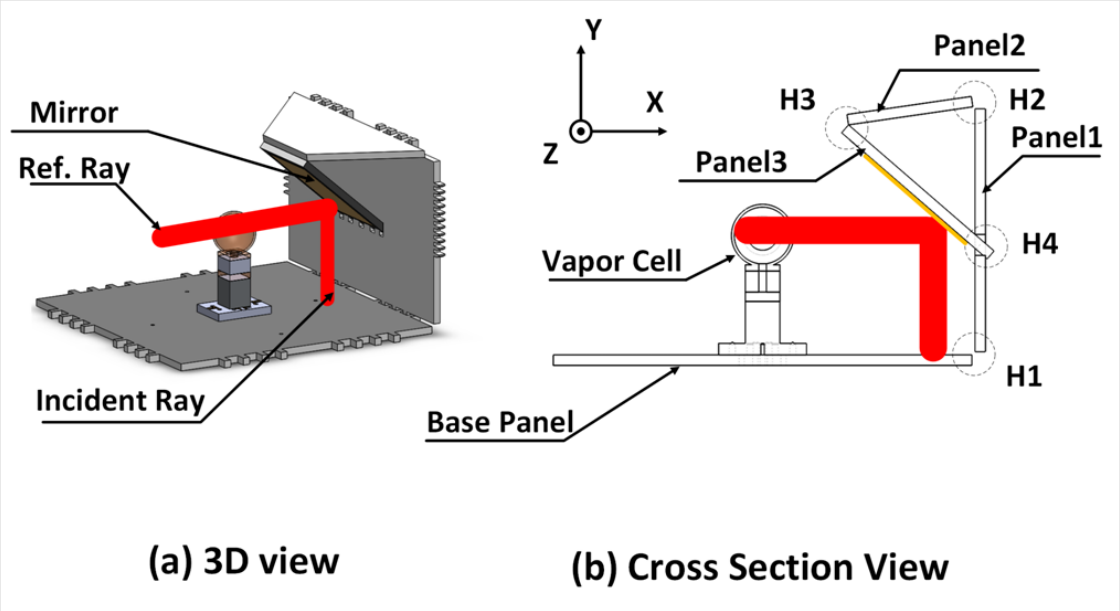

Figure 3.13: Cross sectional view of Folded Structure (only the base panel and one side of the folded structure are shown for clarity)

3.3.2 Folded Backbone Structure

Analytical Model

The folded structure's panels in Figure 3.13 are fabricated on the wafer-level (flat), then subsequently folded into 3D configuration. The folding procedure is performed by rotating panel 1 with respect to the base, panel 2 with respect to panel 1, and panel 3 with respect to panel 2, by utilizing three hinges marked as H1, H2, and H3 in Figure 3.13. The rotation of each panel can be modeled using three Euler's angles (ψ: about the z-axis, θ: about the y-axis and, ϕ: about the x-axis). The orientations of the normal vectors of each panel are calculated using the directional cosine matrix (DCM) in equation (3.16).

$$\begin{bmatrix} \cos\theta\cos\psi & -\cos\phi\sin\psi & \sin\phi\sin\psi \\ & +\sin\phi\sin\theta\cos\psi & +\cos\phi\sin\theta\cos\psi \\ \cos\theta\sin\psi & \cos\phi\cos\psi & -\sin\phi\cos\psi \\ & +\sin\phi\sin\theta\sin\psi & +\cos\phi\sin\theta\cos\psi \\ -\sin\theta & \sin\phi\cos\theta & \cos\phi\cos\theta \end{bmatrix}, \tag{3.16}$$

To achieve 45° mirrors for the current design, the angles of panels relative to each other are summarized in Table 3.1.

Table 3.1: Rotation of the normal vectors of the folded structure panels relative to the adjacent panel

Angle	**Base-Panel1**	**Panel1-Panel2**	**Panel2-Panel3**
ψ	90	109.5	115.5
θ	0	0	0
ϕ	0	0	0

The normal unit vector to the base panel is defined as $\vec{v_B} = [0\ 1\ 0]'$. Thus, the normal unit vectors to the other corresponding panels are defined as

$$\vec{v_1} = [DCM_{B,1}]\vec{v_B}, \tag{3.17}$$

$$\vec{v_2} = [DCM_{1,2}]\vec{v_1}, \tag{3.18}$$

$$\vec{v_3} = [DCM_{2,3}]\vec{v_2}, \tag{3.19}$$

where $[DCM_{i,j}]$ is the directional cosine matrix that describes the j^{th} panel rotation relative to the i^{th} panel. The normal unit vector to the mirror is $\vec{v_m} = -\vec{v_3}$ and the unit vector of the incident ray is $\vec{v_I} = \vec{v_B}$. The reflected ray's unit vector becomes

$$\vec{v_R} = [DCM_{I,R}]\vec{v_I}, \tag{3.20}$$

where the Euler's angles for the $[DCM_{I,R}]$ are ($\psi_{I,R} = \pi - 2(\pi - \beta)$, $\theta_{I,R} = 0$ and, $\phi_{I,R} = \pi/2 - \eta$). β and η are the angles made by the mirror's unit vector and the y- and z-axis respectively, Figure 3.13.

Latches on the sidewalls (panels) of the folded structure ensure the proper alignment of the structure's parts with respect to each other. Similar to the folding process of coils, a predefined mold would be used for folding and permanent enforcement. Since the NMR sensors operation requires heating the cell, a potential misalignment might occur due to thermal expansion of the enforcement material. Our study of different enforcement materials on similar structures concluded that the effect of enforcement material's thermal expansion is inversely proportional to the size of the folded structure, [74].

For example, the coefficient of thermal expansion (CTE) of an AuSn alloy is 16 PPM/°C, a 100°C temperature difference would result in 0.16% volume expansion of the enforcement material. Since the hinge volume is $2mm^3$, and assuming there is 20% more alloy on one of the hinges between the base and panel 1, the excess would result in 6.3mrad misalignment of panel 1 relative to the base panel, which is translated to $50\mu m$ misalignment of the beam with respect to the cell, according to equations (3.17)-(3.20).

Projection of Imperfections to Performance

Displacement of the pump beam would result in reduction of the pumping rate, which would reduce the number of polarized Rb atoms. Misalignment of the probe, on the other hand, reduces the number of interrogated atoms. Both scenarios result in a drop of the signal-to-noise ratio (SNR). Since the used beams for pumping and probing are Gaussian beams, the drop in SNR is expected to follow the Gaussian function:

$$y = ae^{-x^2/2c^2}, \tag{3.21}$$

where y is the SNR of the magnetometer, a is the SNR value in the perfectly aligned state, x is the displacement of the beam relative to the cell, c is the width of the Gaussian curve which determines the relation between the SNR decay and the beam displacement.

Experimental Results

To verify experimentally the effect of reflector misalignment with respect to the cell, a sample reflector of the folded structure was placed on a 6-axis optical mount and its angle was controlled to create a displacement of the light beams (pump and probe) relative to a 2mm cell. Figure 3.14 illustrates the experimental setup. Figure 3.15 shows the relationship of the normalized magnetometer's sensitivity to displacement of the beam. As predicted by the model, the drop in the magnetometer sensitivity follows the Gaussian function. We found that SNR is more sensitive to the probe beam displacement than to the pump beam. This is explained by the optical power on the pump beam to be higher than the probe beam.

3.4 Prediction of Performance

As discussed in previous sections, the folding error can be either due to the folded coils, which affects the relaxation time T_2 of Xe atoms, or due to the folded structure, which affects the Signal-to-Noise Ratio (SNR) of the electron paramagnetic resonance (EPR) magnetometer, [20].

Assuming a closed loop system with the white noise limiting the photo-detector, the Angle Random Walk (ARW) of the NMRG is predicted by the relation, [42],

$$ARW = \frac{3600}{T_2 \times SNR\sqrt{\Delta f}}[^\circ/\sqrt{hr}], \tag{3.22}$$

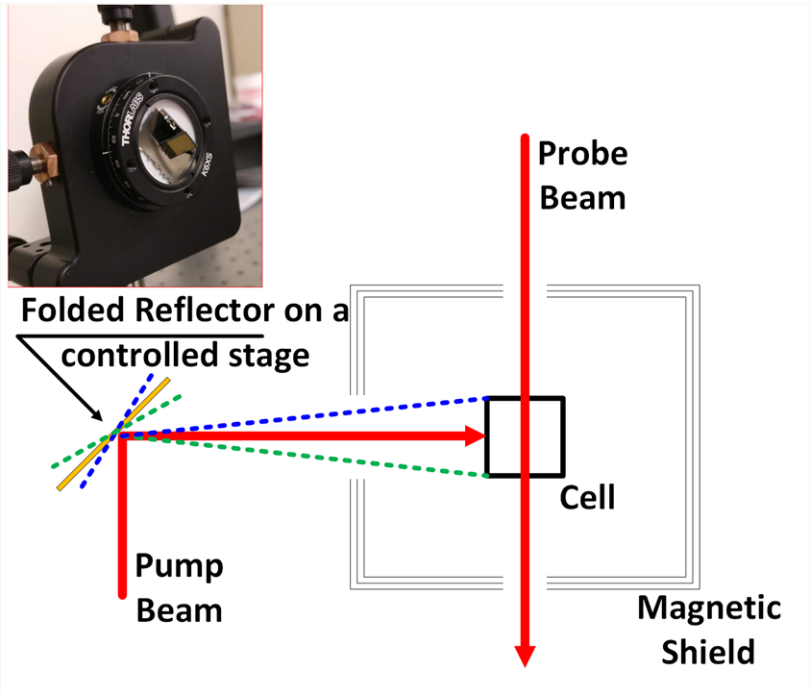

Figure 3.14: Sketch illustrating the experimental setup used for measuring the effect of pump beam displacement relative to the cell on the magnetometer sensitivity

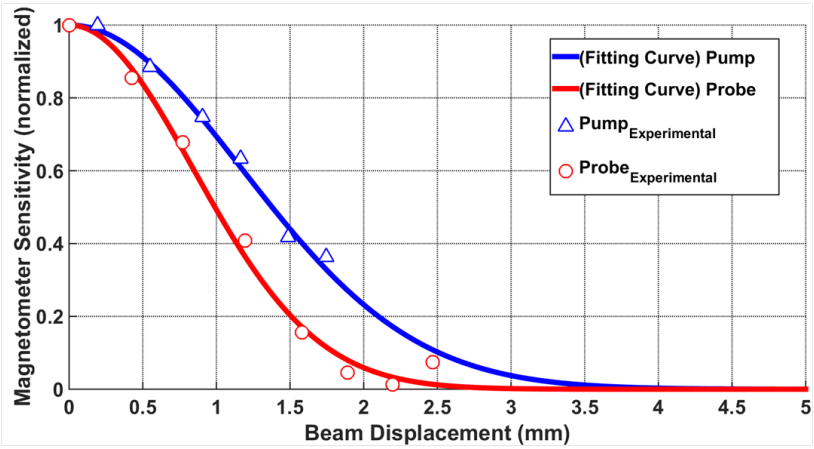

Figure 3.15: Normalized Magnetometer Sensitivity (experimentally measured) vs beams displacement relative to the cell (pump: triangles, probe: circles)

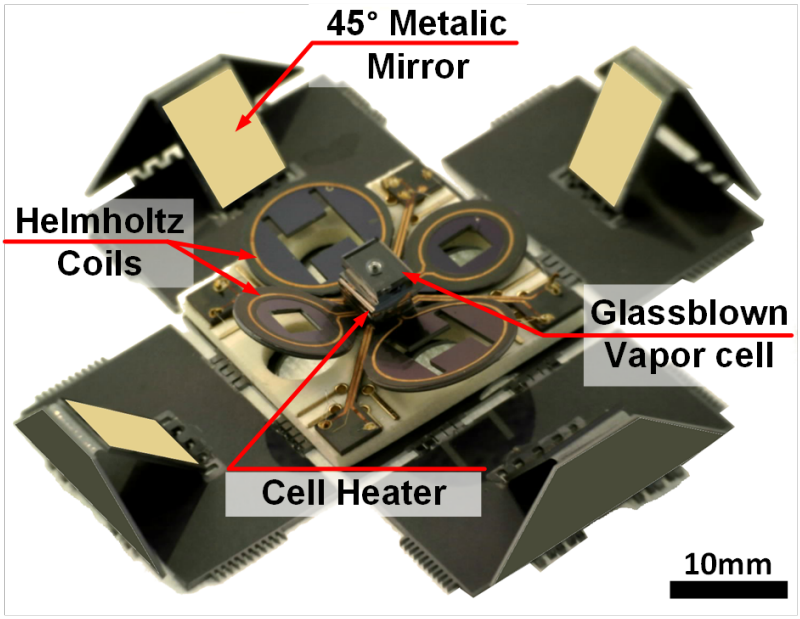

Figure 3.16: Partially folded NMR sensor prototype showing all components of the system

where T_2 is the transverse relaxation time, SNR is the signal to noise ratio, Δf is the bandwidth of the phase noise in Hz.

On the other hand, the fundamental sensitivity limit of the NMRM is related to two factors, EPR magnetometer SNR and Xe atoms relaxation time T_2. The fundamental sensitivity can be defined as, [20],

$$\delta B_n = \frac{1}{2\pi\gamma_{Xe}T_2} \times \frac{\delta B_e}{P \times dB_n/dP}, \tag{3.23}$$

where γ_{Xe} is the gyromagnetic ratio of Xe atoms, δB_e is the noise floor of the EPR magnetometer, P is the percentage of polarized Xe atoms, dB_n/dP is the magnetic field produced by Xe atoms per unit polarization.

The fundamental sensitivity of EPR magnetometer of a cell with an internal diameter of 1mm containing Rubidium and a buffer gas is limited by the atomic shot noise to approximately $120\text{fT}/\sqrt{Hz}$, [33].

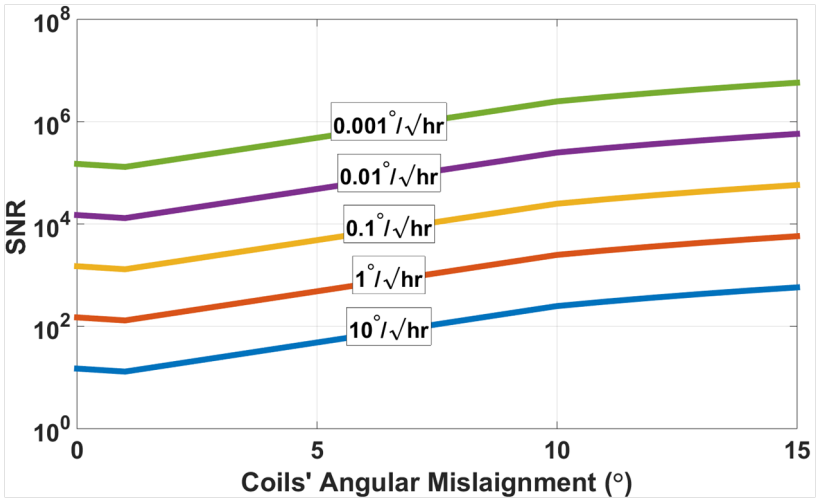

Figure 3.17: NMRG ARW as a function of SNR and coils' angular misalignment

Assuming ^{129}Xe transverse relaxation time T_2=20s, the effect of the angular misalignment of the coils on the NMRG ARW and the NMRM fundamental sensitivity is presented by Figure 3.17 and Figure 3.18, respectively. Similarly, curves with circular markers in Figure 3.19 and Figure 3.20 represent NMRG ARW and NMRM sensitivity, respectively, due to linear axial misalignments, while the curves with triangular markers in Figure 3.19 and Figure 3.20 represent linear radial misalignments. The general trend in both figures is that as the misalignment increases the required SNR to achieve a certain ARW value increases. For example, SNR of 150 can achieve ~$1°/\sqrt{hr}$ with perfectly aligned coils, while 5° angular misalignment increases the SNR requirement by a factor of 4 to achieve the same $1°/\sqrt{hr}$.

To visualize the impact of the folded structure misalignment on the device performance, we assumed a constant SNR=5000. Using equations (3.22), (3.23) and extrapolating the experimental points presented by Figure 3.15, the NMRG ARW and NMRM sensitivity are depicted by Figure 3.21 and Figure 3.22, respectively, under different combinations of the relaxation time (T_2) and the folded structure misalignment. The curves with circular markers of Figure 3.21 and Figure 3.22 represent cases when the misalignment occurs on the pump side and the curves with triangular markers are on the probe side of NMRG and NMRM, respectively.

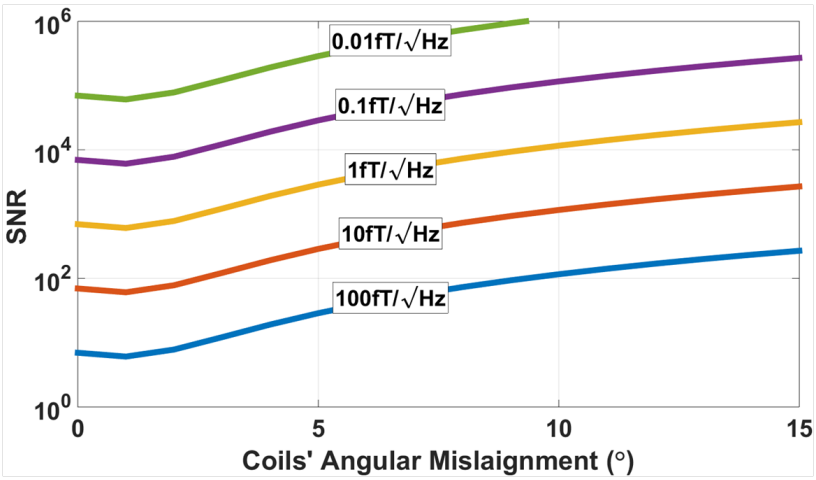

Figure 3.18: NMRM sensitivity as a function of SNR and coils' angular misalignment

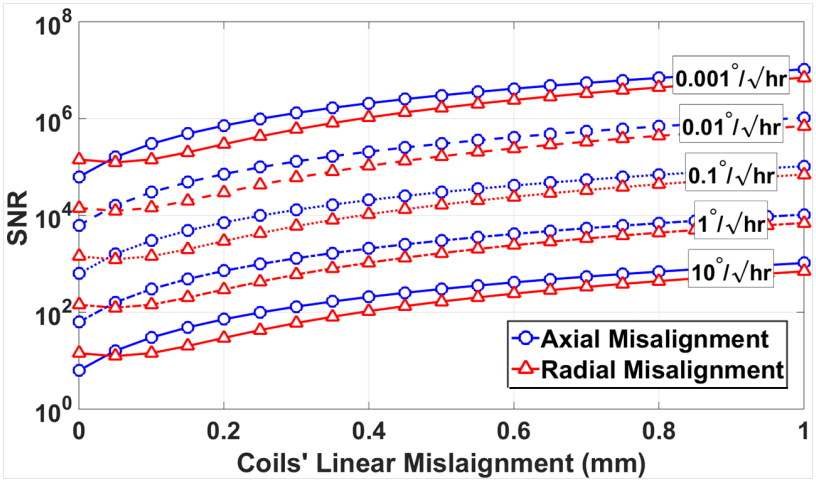

Figure 3.19: NMRG ARW as a function of SNR and coils' linear misalignment (axial: circular markers, radial: triangular markers)

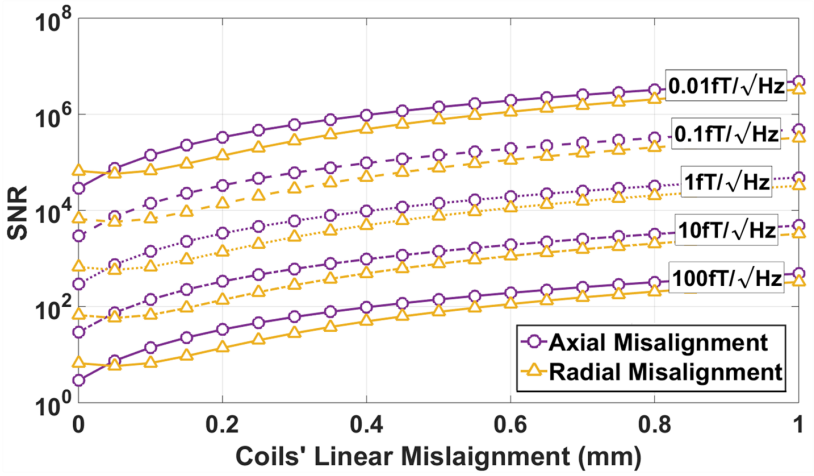

Figure 3.20: NMRM sensitivity as a function of SNR and coils' linear misalignment (axial: circular markers, radial: triangular markers)

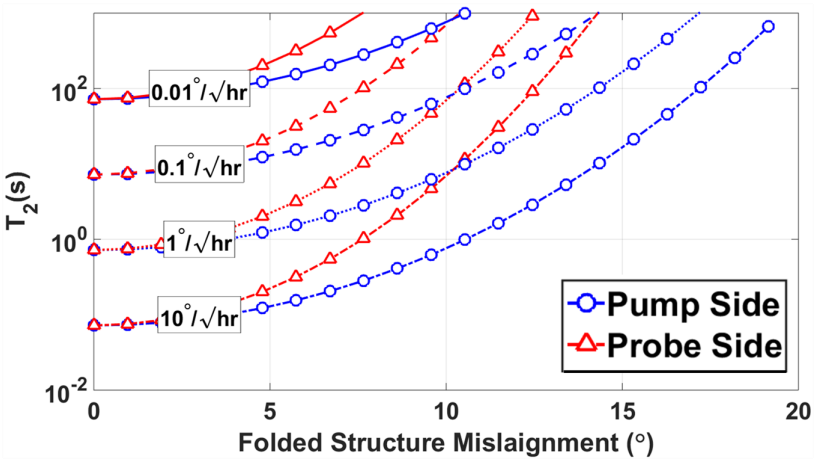

Figure 3.21: NMRG ARW as a function of Relaxation time (T_2) and Folded Structure misalignment (Pump: circular markers, Probe: triangular markers)

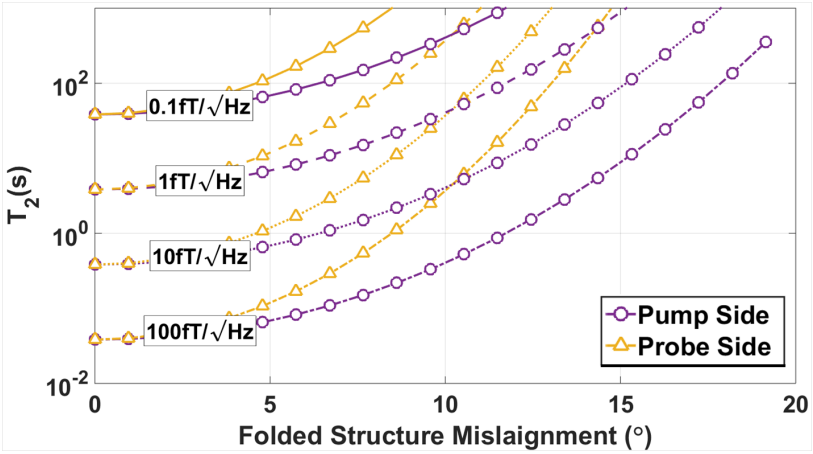

Figure 3.22: NMRM sensitivity as a function of Relaxation time (T_2) and Folded Structure misalignment (Pump: circular markers, Probe: triangular markers)

The developed error model and the phenomenological analytical model suggests that the introduced design with 5 mrad angular misalignment between the coils and the folded mirrors and 100μm linear misalignment between folded coils can achieve NMRG's ARW ~0.1°/$\sqrt{hr}$ and NMRM fundamental sensitivity better than 10 fT/$\sqrt{Hz}$.

3.5 Conclusion

In this Chapter, we presented an approach for implementation of MEMS components for NMR sensors utilizing a batch fabrication process, with minimum assembly requirements. We evaluated the performance boundaries of our suggested design by estimating possible fabrication imperfections and projected their effect on the device performance. Our error analysis method is general and could be applied to other implementations. The analysis suggested that the presented folded MEMS approach is a strong candidate for implementation of at least a tactical-grade level of performance micro-NMRG and a femto-Tesla level of performance micro-NMRM.

Chapter 4

Design Considerations for Micro-Glassblown Atomic Vapor Cells

This chapter presents a design process for miniaturized atomic vapor cells using the micro-glassblowing process. It discusses multiple design considerations, including cell geometry, optical properties, materials, and surface coating. In Section 4.1, the overall design approach of miniaturized cells is briefly described. Then, in Section 4.2, the geometrical aspect of the cell fabrication is discussed, where we introduced analytical and finite element models and, subsequently, supported results of analysis by experimental validation. In Section 4.3, the optical modeling and simulation results of the fabricated cells backed up by experimental validation presented. Section 4.4 presents our study of materials and cell wall coating on the performance of atomic cells.

4.1 Design

Glassblowing of miniaturized cells on a wafer-level is based on anodic bonding a glass wafer to a silicon wafer with pre-etched cavities under atmospheric pressure conditions. The wafer stack is then heated up to a temperature higher than the softening point of the glass; the combination of glass softening and pressure build-up in the pre-etched cavities creates axisymmetric spherical shells, Figure 4.1, [34].

After the glassblowing step, the cells are rapidly cooled down to preserve their shape and to prevent any crystallization of the glass, [82]. This rapid cooling puts a thermal shock on the cell walls and builds up stresses across the geometry. Additionally, the cooling process results in a pressure drop inside the cells, which creates a pressure difference across the cell walls. Depending on the pressure difference and wall thickness, breakage might happen at the thinnest part of the cell.

For analysis, we use a multi-step approach for designing miniaturized glassblown cells. The design process starts with an analytical model presented in [34], which estimates dimensions of the resulting geometry of cells. Next, a finite element model predicts a more realistic geometry of the cell using isothermal flow simulation in COMSOL. The resulting geometry is then exported to solid mechanics simulation, which estimates the maximum stress on the cell walls and predicts whether the cell can survive the force generated by the pressure difference across its walls. Finally, the model is exported to optical simulation software to simulate the optical behavior of the cells.

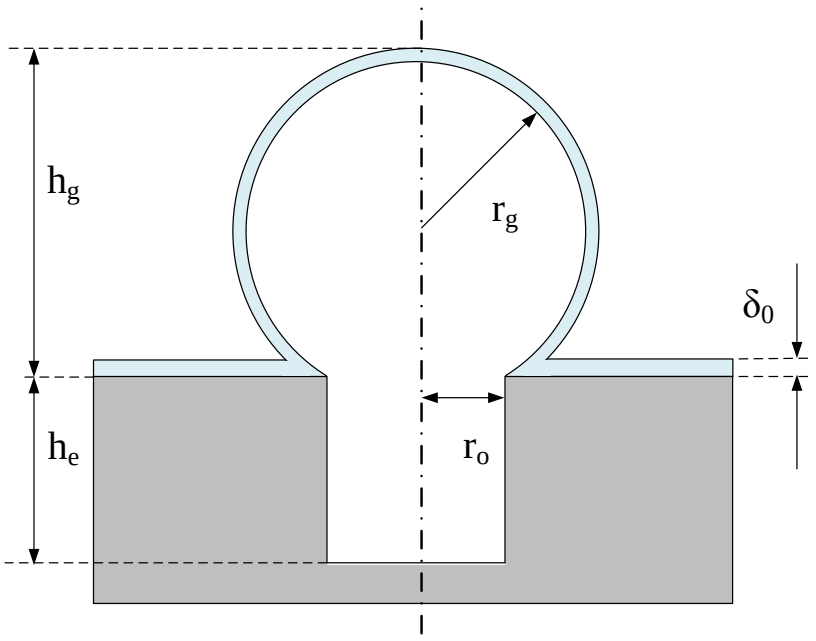

Figure 4.1: Sketch of cross sectional view of a glassblown cell

4.2 Geometry

In this section, we present an analytical model and FEM model, and in light of the two models we discuss the parameters that influence the geometry of the cells, such as their size, sphericity, and wall thickness. Subsequently, we present experimental characterization that validates the simulation results.

4.2.1 Analytical Model

The height h_g and the inner radius of the cell r_g, shown in Figure 4.1, are given by equations (4.1) and (4.2), respectively, [34]

$$h_g = \frac{\left[\left(3V_g + \sqrt{r_o^6\pi^2 + 9V_g^2}\,\right)\pi^2\right]^{2/3} - r_o^2\pi^2}{\pi\left[\left(3V_g + \sqrt{r_o^6\pi^2 + 9V_g^2}\,\right)\pi^2\right]^{1/3}} \tag{4.1}$$

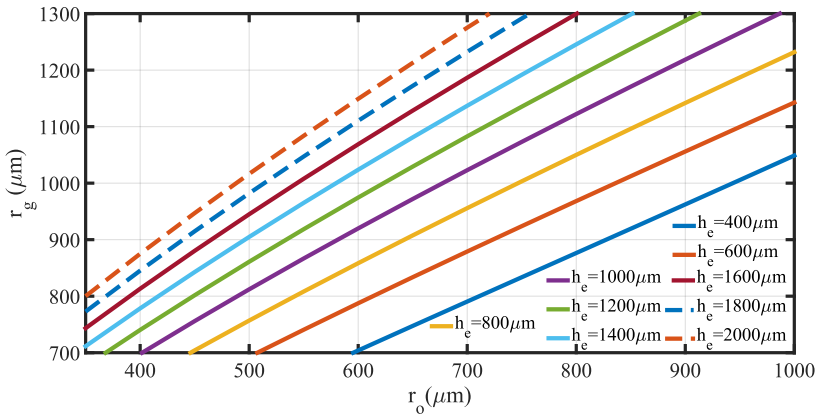

Figure 4.2: Radius of glassblown cell r_g vs. the cavity radius r_o for different cavity depths h_e, ranging from $600\mu m$ to $2000\mu m$

$$r_g = \frac{h_g^2 + r_o^2}{2h_g}, \tag{4.2}$$

where V_g is the inner volume of the cell and is defined as

$$V_g = h_e \pi r_o^2 \left(\frac{T_f P_s}{T_s P_f} - 1 \right), \tag{4.3}$$

where T_f and T_s are temperatures of the glassblowing furnace and the cavity sealing measured in Kelvins, P_f and P_s are the pressure values (in Torr, for example) during the glassblowing and the cavity sealing, respectively, r_o is the radius of the etched cavity and h_e is the etched cavity depth. The average thickness of the cell wall can be estimated as [34],

$$\delta = \frac{\delta_0 r_o^2}{h_g^2 + r_o^2}, \tag{4.4}$$

where δ_0 is the initial glass layer thickness, as shown in Figure 4.1.

The glassblowing process parameters (r_o and h_e) can produce a wide variety of cell sizes and sphericity levels. Figure 4.2 depicts a selected subset of these parameters. In this paper, our target application for the glassblown shells is miniaturized atomic cells, so a cell radius, r_g, on the order of 1mm is desired. A range of the cavity radii r_o, that produces a cell with $r_g = 1$mm, is from 488μm to 945μm. However, as it was noted in [34], a smaller r_o is

recommended to achieve higher sphericity cells.

The increase in cell sphericity reduces its asymmetry. Cells with high asymmetry have shown larger quadrupole splitting in ^{131}Xe frequency, [130]

4.2.2 Sphericity

The cell sphericity is defined as the ratio of the effective volume to the surface area of the exposed part of the cell above the glass wafer surface level, [122]. It is calculated as

$$\Psi = \frac{\pi^{1/3}(6V_g')^{2/3}}{A_g}, \tag{4.5}$$

where V_g' ans A_g are the volume and the surface area of the exposed part of the cell, which is above the glass wafer surface level, and both are calculated as

$$V_g' = \frac{\pi}{3}h_{g|exp}^2(3r_g - h_{g|exp}), \tag{4.6}$$

$$A_g = \pi h_{g|exp}(4r_g - h_{g|exp}), \tag{4.7}$$

where $h_{g|exp}$ is the height of the exposed part of the shell, defined as

$$h_{g|exp} = h_g - \delta_0 \tag{4.8}$$

Note, h_g is defined from the silicon /glass interface to the top of the cell, as shown in Figure 4.1.

There are several approaches to produce cells with higher sphericity. These include controlling the process pressure, either by increasing the initial cavity pressure (P_s), [133], or reducing the glassblowing furnace pressure (P_f), [9], or both. Another approach is to

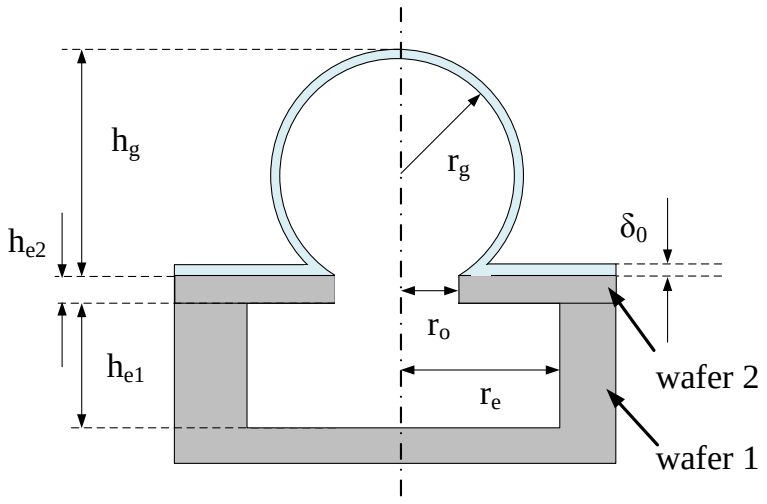

Figure 4.3: Sketch of cross sectional view of a glassblown cell using a dual-wafer approach to build the Si cavity

increase the initial volume of the cavity while keeping the cavity radius r_o small, as it was suggested in [34]. In this process, a stack of two wafers was used to build the Si cavity. The first one is a thick Si wafer, 1mm for example, where large cavities are etched. The second wafer is a thin wafer, 100μm for example, bonded to the first wafer and smaller openings are etched through, Figure 4.3. This approach allows for larger volume without sacrificing sphericity and relaxes the requirement on the depth of etching. The inner volume of the cell becomes

$$V_g = [h_{e1}\pi r_e^2 + h_{e2}\pi r_o^2]\left(\frac{T_f P_s}{T_s P_f} - 1\right), \tag{4.9}$$

where h_{e1} and r_e are the cavity depth and radius of the wafer 1, and h_{e2} is the wafer 2 thickness.

To improve sphericity, one can reduce the glass thickness to increase the exposed part on top of the glass surface. However, that would create thin shells, and the pressure difference across the shell walls will create compressive stress that is larger than the compressive strength of the glass material, which would lead to breaking of the cell. To estimate the maximum cell volume, we created a finite element model, which is discussed next.

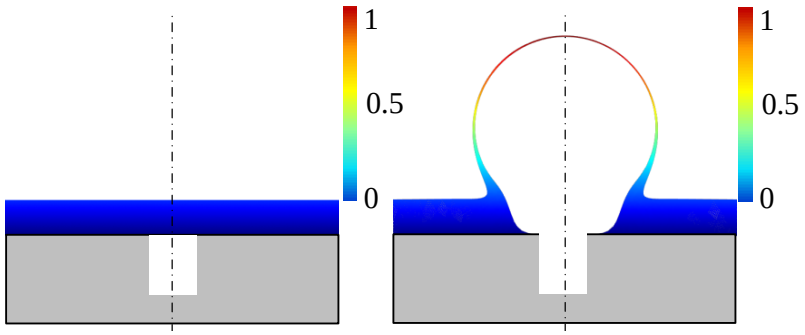

Figure 4.4: FEM Simulation shows a cross sectional view of the sample before and after glassblowing.The scale bar represents the normalized displacement of glass during the glassblowing preocess.

4.2.3 Finite Element Model

The glass wall thickness is not uniform in this process, [34], and since this parameter is essential to accurately predict the light interaction with the cell walls, we used a finite element model using COMSOL Fluid Flow physics to estimate the wall thickness distribution in addition to the maximum volume of the cells. The developed model was adopted from our previous work, [8]. The shape of the glassblown cell at different time steps is predicted with a Newtonian isothermal fluid flow model with an adaptive re-meshing in COMSOL Multiphysics FE Package. In this model, the instantaneous volume and pressure of the cell and the cavity were calculated at each time step of the simulation, and once the equilibrium-state is reached the deformation of the glass layer stops. Figure 4.4 shows snapshots of initial and final geometry of cell's cross-section during the glassblowing.

The resulting geometry from the fluid flow model was exported to a solid mechanics simulation, and the pressure difference after cooling was calculated and applied to the cell's outer surface to estimate the maximum stress value and location. The model predicted that the maximum stress was always concentrated at the top part of the cell and that it is because the shell's minimum thickness is at the top, which matches what was experimentally demonstrated earlier in [34].

4.2.4 Glass Thickness δ_0

Using a combination of the FEM model and compressive strength of the Borosilicate glass (100 MPa), we estimated the maximum cell volume that would survive the glassblowing process. This process was repeated for different ratios of the glass thickness δ_0 to the cavity opening r_o. Sphericity of the exposed part of the cell was calculated using equation (4.5). The trend in Figure 4.5 shows that as we increase the glass thickness relative to the cavity radius, sphericity of the maximum cell size drops following closely a quadratic line equation

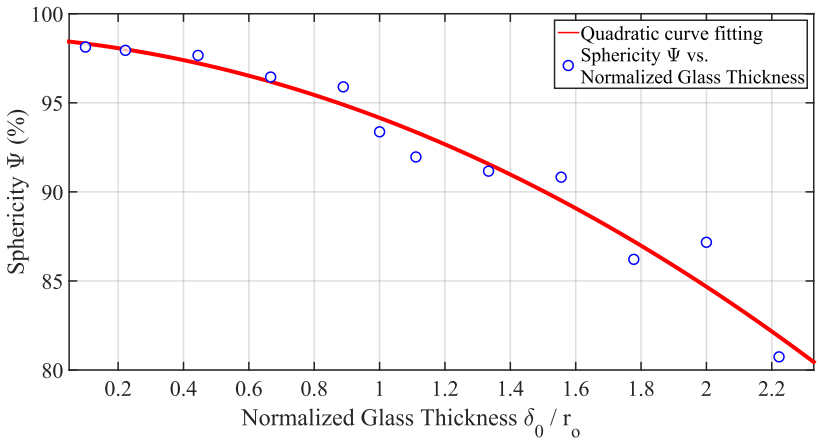

Figure 4.5: Sphericity of the maximum cell volume vs. the normalized glass thickness estimated using FEM modeling. Normalized glass thickness is the ratio of the glass thickness δ_0 to the cavity radius r_o.

$$f(x) = ax^2 + bx + c, \tag{4.10}$$

where, x represents a normalized glass thickness (δ_0/r_o), and coefficients a, b and c (with 95% confidence bounds) are -2.55±2.14, -1.83±5, and 98.53±2.57, respectively. Additionally, increasing the normalized glass thickness increases the thickness variation of the cell walls from top to bottom. On the other hand, the normalized radius of the maximum cell volume, that would survive the glassblowing and the subsequent cooling, was found to increase quadratically with the increase of the glass thickness relative to the cavity radius r_o. Normalized radius is the radius of a three-point circle fitted to the top and two sides

of the exposed part of the cell divided by the cavity opening r_o. The equation parameters of the curve fitting line in Figure 4.6, a, b and $c$are -0.29±0.16, 1.98±0.4, and 1.516±0.2, respectively, with 95% confidence bounds.

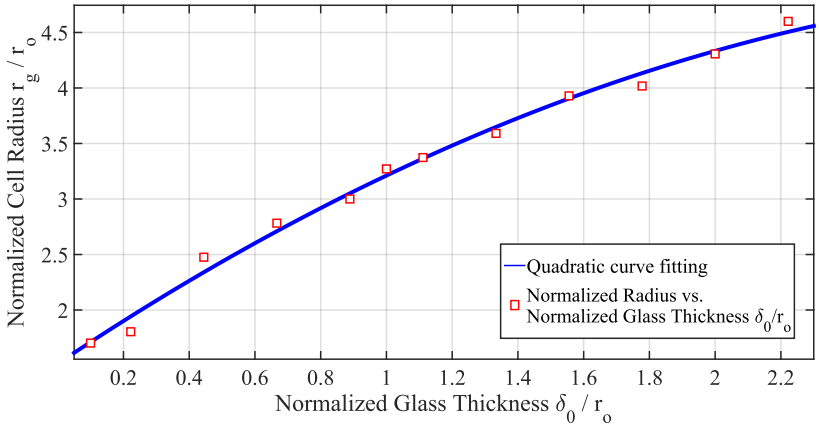

Figure 4.6: Normalized radius of the maximum cell volume (r_g/r_o) vs. normalized glass thickness ($\delta 0/r_o$), estimated using FEM modeling.

From Figure 4.5 we deduce that in order to achieve a high sphericity level, one should use a glass thickness, that is $1/10^{th}$ of the cavity radius r_o. From Figure 4.6, r_o should be on the order of 1.7× of the desired cell radius r_g. For example, if a cell of radius 1mm is desired, the cavity opening radius r_o should be 588μm and the glass thickness δ_0 should be ≈ 59μm, to achieve ≈98% sphericity. From equation (4.4), the average thickness of the resulting shell will be ≈6.5μm. While this combination of parameters would survive the pressure difference due to glassblowing, from a practical point of view, it might not survive other steps of the process, such as backside opening and subsequent wet cleaning.

4.2.5 Characterization of Geometry

To validate the model, we fabricated two samples on a 1mm thick wafer, and 350 μm glass (Pyrex) thickness, the Si cavity radii for the samples were 225μm and 300μm, while the etch depth was 700μm. The measured cell radius and height of these cells are presented

in Table 4.1. Visual inspection shows that an agreement between the fabricated cell and the geometry predicted by the FEM simulation, in terms of the cell height and radius, is within 95%.

Table 4.1: comparison between simulated and experimentally measured parameters of two fabricated samples, (all measurements are in (mm))

	Simulation		Experiment	
	Radius	Height	Radius	Height
Cell 1	0.78	1.33	0.79	1.34
Cell 2	0.93	1.67	0.98	1.71

4.3 Optical Properties

In this section, we present an optical simulation model and discuss optical properties of the glassblown cells. The optical properties of interest for the atomic cells are light transmission through the cell and variation in optical polarization. Both parameters are critical for designs of NMR sensors.

4.3.1 Simulation

The optical simulation was performed using Monte Carlo ray tracing method, [54]. In this method, the light beam is broken down to a large number of individual rays and the interaction of those rays with different parts of the miniaturized cell is then integrated using Monte Carlo integration to predict the behavior of the whole beam within the cell. The simulation shows that due to the changes of the cell wall thickness (thinner at the top and thicker at the base, Figure 4.4), different parts of the beam experience different diffraction angles. The bottom part of the cell is usually the thickest, which causes the beam at that section to diffract downward and be trapped in the cell, bundle "A" in Figure 4.7-(top). The

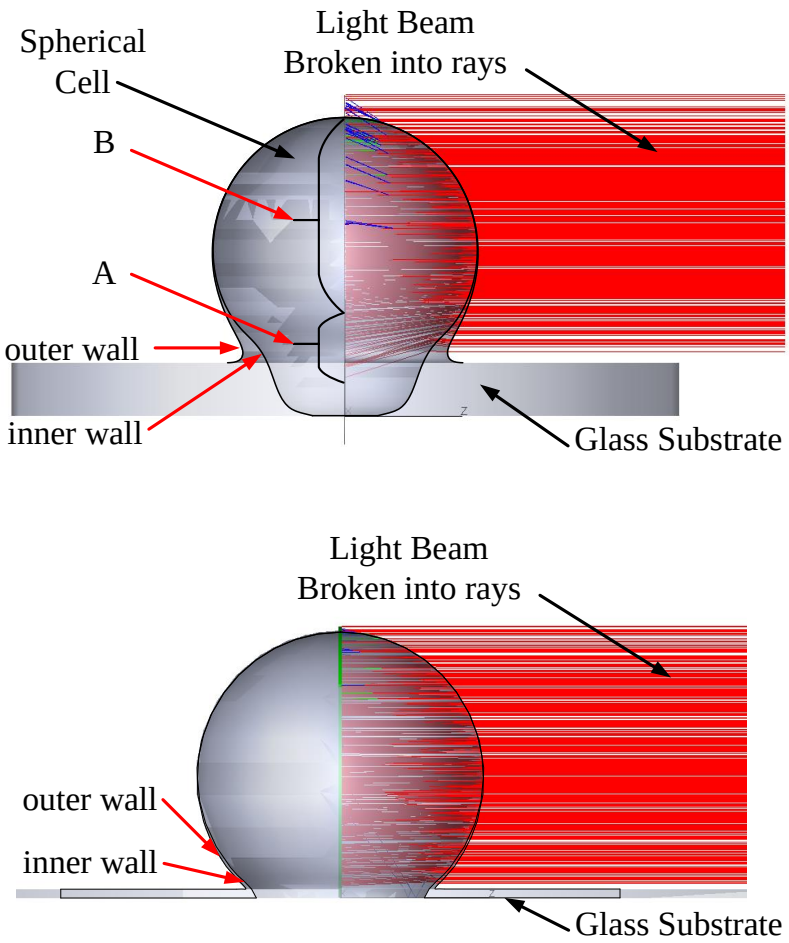

Figure 4.7: Cross-section illustration showing the interaction of the optical beam with the cell. Top: 89% sphericity, Bottom: 98% sphericity. Ray bundle (A) in the top illustration experience the most diffraction and are trapped into the cell

mid-section of the beam transmits through the cell; however, it still experiences downward bending, as it propagates out of the cell, bundle "B" in Figure 4.7-(top). Additionally, the beam polarization was analyzed by grouping individual rays into pockets and averaging their polarization parameters (ellipticity and azimuth angle). The polarization maps in Figure 4.8 show that the cell preserves the azimuth angle and ellipticity for the majority of the transmitted beam, Figure 4.8-a) and Figure 4.8-b), respectively, and the degree of polarization is within 95%. This polarization distortion is negligible and it does not affect the operation of sensors.

The simulation also shows that cells with small normalized glass thickness and high sphericity pass the light beam through with minimal diffraction, Figure 4.7-(bottom).

4.3.2 Optical Characterization

We measured the optical properties of the fabricated samples, discussed in Section 4.2.5. The experimental setup consisted of a laser beam, a linear polarizer, and a quarter wave plate, creating a circularly polarized light that enters the sample. The transmitted light then propagates to a polarimeter (Thorlabs PAX 5710). The power and polarization of the optical beam were measured before and after the transmission through the samples. The beam radius was $\approx 0.5\times$ of the cell radius. Table 4.2 shows a comparison between the measured and simulated optical transmission and polarization of the two fabricated samples. The simulation results are consistent with the well-known 4% per surface loss at an air/glass interface. The discrepancy between the measured and simulated values can be a result of the parasitic glass bubbles on the samples due to defects that could have blocked a part of the transmitted light and changed its polarization.

As mentioned earlier, micro-glassblown cells have multiple in-plane and out-of-plane ports. Even though in-plane ports provide optical paths for light transmission through the

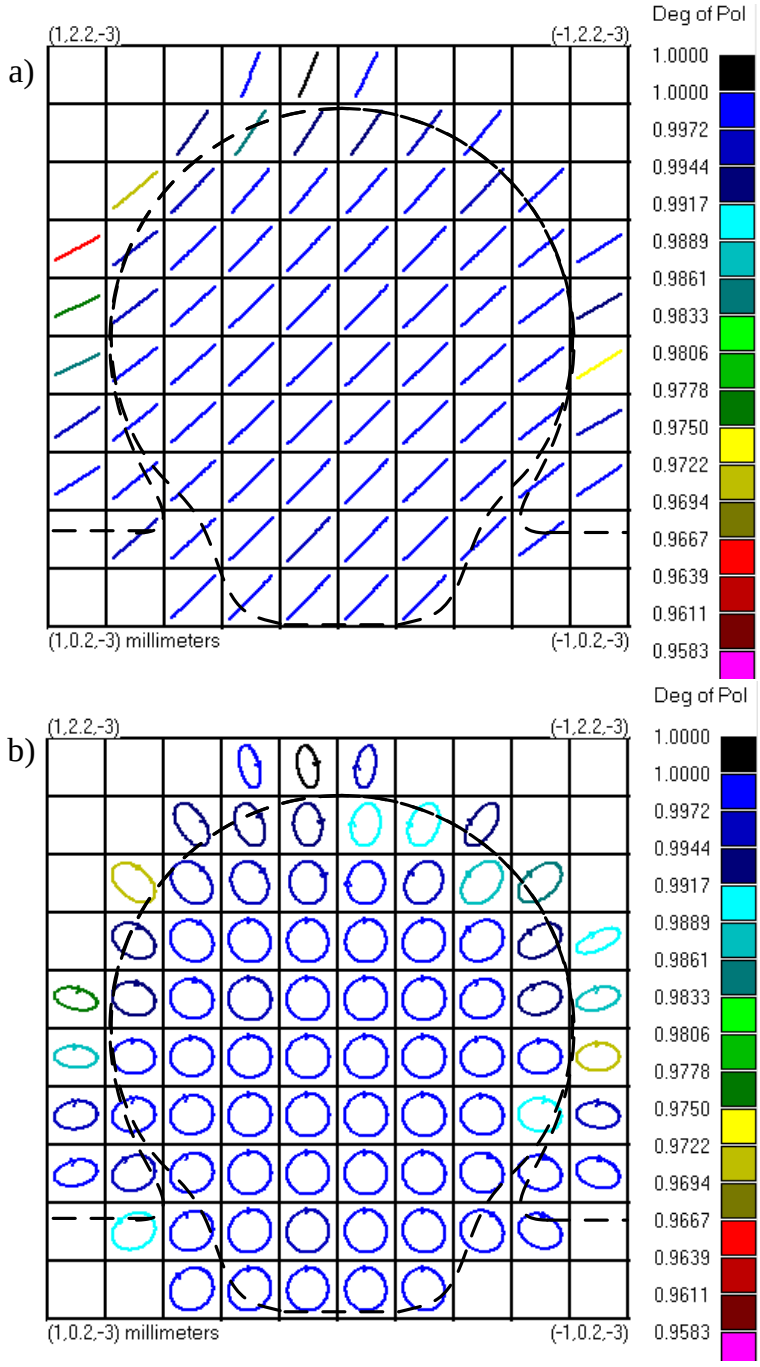

Figure 4.8: Simulation results of the transmitted beam polarization for two cases: a) +45 linearly polarized light, b) right circular polarized light. Dashed lines represent the outer borders of the cell. Only the beam pockets on edges of the cell experience polarization changes, either in the polarization angle or ellipticity, while the majority of the beam's polarization is unchanged.

Table 4.2: Comparison of optical properties of two cells

	Power Transmission		Polarization (ellipticity)	
	Simulation	Experiment	Simulation	Experiment
Cell 1	86.2%	80.6%	1.43°	1.3°
Cell 2	86.2%	83.1%	1.55°	3.8°

cell, the cells are not perfectly symmetric around them, and the beam would experience a downward bending, as discussed earlier. On the other hand, the cells are axisymmetric around the out-of-plane port, but their transmission is limited by the glassblowing cavity opening r_o, which is on the order of 1/2 of the cell radius r_g. To estimate the optimal orientation of light coupling to atomic sensors, we used the optical magnetometer scale factor as a metric to compare different orientations. The first configuration is in-plane (horizontal) pumping and probing, Figure 4.9-(a); the second configuration is out-of-plane (vertical) pumping and horizontal probing, 4.9-b). Figure 4.10 shows the Rubidium magnetometer response of the two configurations; the vertical pumping improved the magnetometer scale factor by 2×.

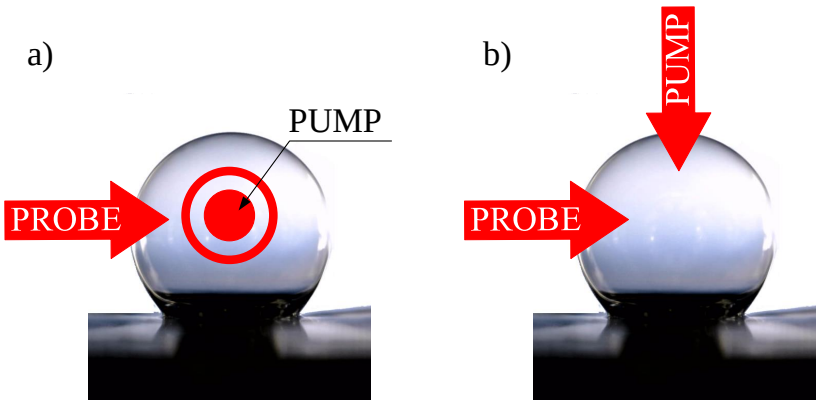

Figure 4.9: Illustration of two different orientations of pumping and probing; (a) in plane pumping and probing, (b) out-of-plane pumping and in-plane probing

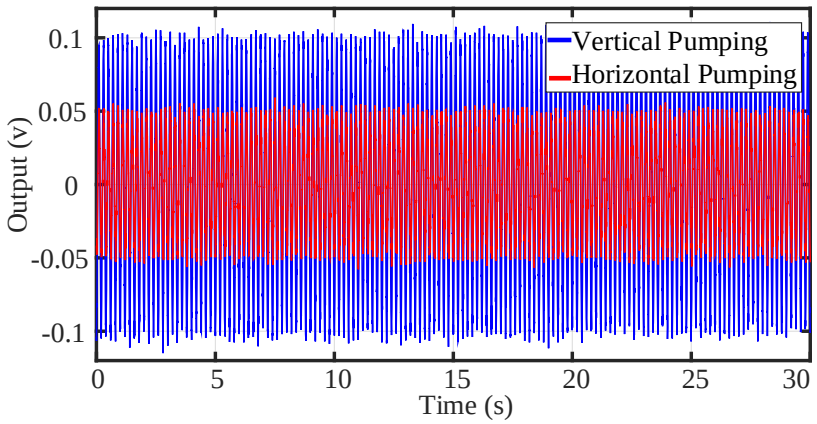

Figure 4.10: Experimental results of Rb magnetometer signals for vertical (blue) and horizontal (red) pumping. The figure shows that vertical pump improved the Rb magnetometer scale factor by 2×.

4.4 Filling and Coating

In this section, the filling and coating process of miniaturized spherical atomic cells are discussed. We briefly introduce the fabrication and filling process followed by a study on different wall materials and coating and experimentally measured their effect on the nuclear spins relaxation.

4.4.1 Background

The transverse relaxation time of the noble gas atoms is directly related to the performance of NMR sensors. For gyroscopes, for example, the angle random walk (ARW) is predicted to depend on T_2 time as follows, [42],

$$ARW = \frac{3600}{T_2 \times SNR\sqrt{\delta f}}[^\circ/\sqrt{hr}], \tag{4.11}$$

where T_2 is the transverse relaxation time of the Xe atoms, SNR is the signal-to-noise ratio of the electron paramagnetic resonance (EPR) magnetometer, and δf is bandwidth of the phase noise in Hz. The fundamental sensitivity limit of an NMR magnetometer (NMRM)

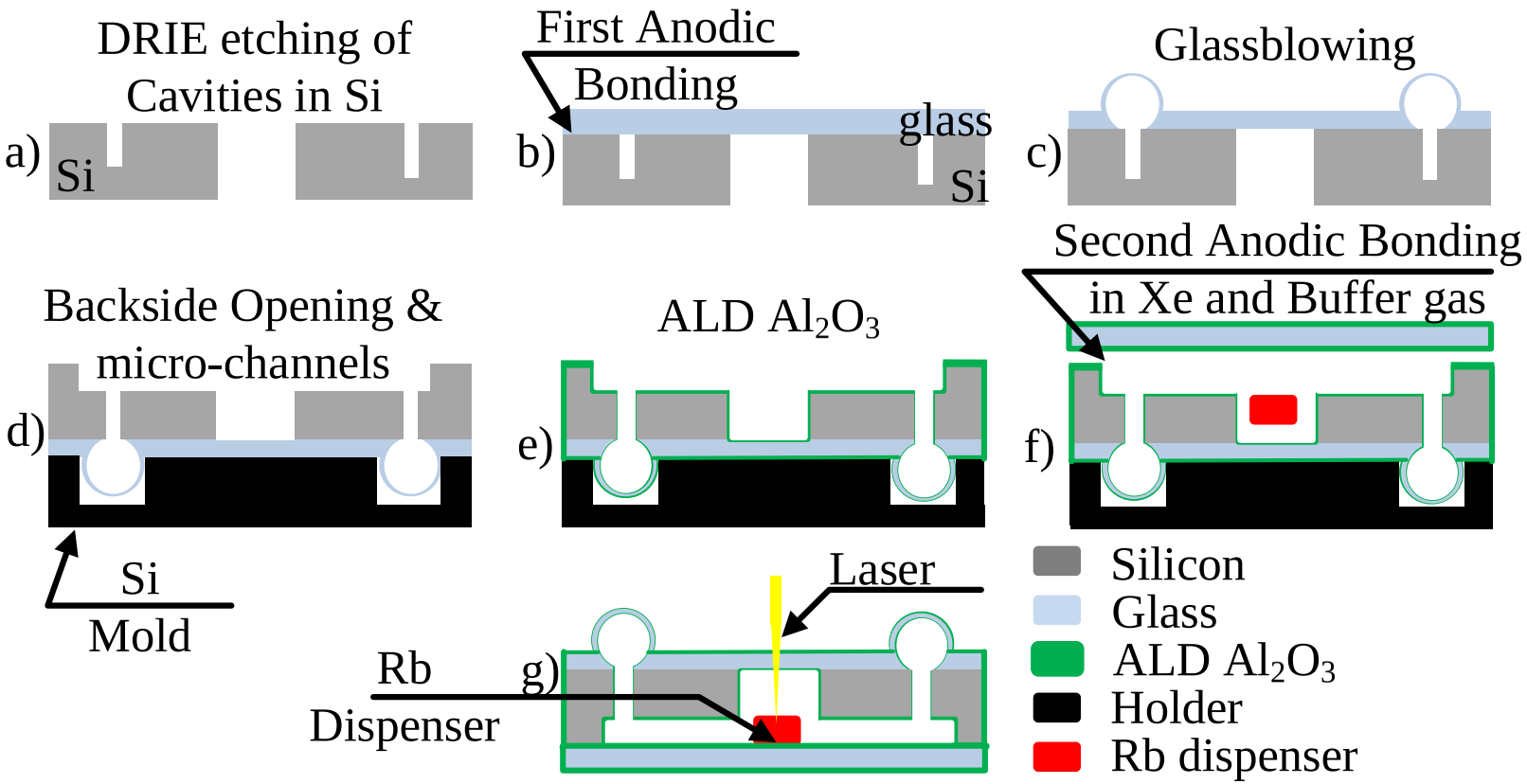

Figure 4.11: Description of the process flow: (a) DRIE etching of 700μm and through wafer cavities in 1mm Si wafer, (b) first anodic bonding of glass to the etched Si wafer, (c) glassblowing of cells, (d) cell back-side opening and channel definition using DRIE etching, (e) Atomic Layer Deposition (ALD) of 10nm Al_2O_3, (f) loading the Rb dispenser and performing the second anodic bonding in a noble gas and buffer gas filled chamber, (c) dispensing alkali metal through micro channels by laser heating of Rb source

depends on the T_2 time as, [20],

$$\delta B_n = \frac{1}{2\pi\gamma T_2} \times \frac{\delta B_e}{P \times dB_n/dP}, \tag{4.12}$$

where δB_e is the noise floor of the EPR magnetometer, P is the percentage of polarized Xe atoms, dB_n/dP is the magnetic field produced by Xe atoms per unit polarization, taking into consideration the "enhancement factor" of direct interaction with the alkali metal vapor, [111]. Several factors can affect the relaxation time of the noble gas atoms in atomic vapor cells, summarized as, [76],

$$\frac{1}{T_{2|total}} = \frac{1}{T_{2|coll}} + \frac{1}{T_2'} + \frac{1}{T_{2|\Delta B}} + \frac{1}{T_{2|wall}}, \tag{4.13}$$

where, $T_{2|total}$ is the effective transverse relaxation time, $T_{2|coll}$ is the relaxation time due to collisions with alkali metal atoms, T_2' is the relaxation time due to self-collision of Xe atoms, $T_{2|\Delta B}$ is the relaxation time due to magnetic field in-homogeneity inside the cell, and $T_{2|coll}$ is the relaxation time due to collisions of atoms with cell walls. In mm-sized cells, the wall collisions and spin exchange relaxation are dominant, [56], and therefore special care needs to be taken during the cell construction.

4.4.2 Fabrication and Filling Process

There are multiple filling approaches to introduce alkali metal and buffer gas in the miniaturized cells. The approaches have been discussed widely throughout the literature, [36, 35, 50, 80, 66, 61, 101]. The approach that we adopted in this paper for filling cells using an on-chip alkali metal dispenser was introduced previously for planar cells in [32] and [89]. A recent study that reviewed those approaches, [59], comes to the conclusion that a filling process like the one suggested here, which combines an on-chip dispensing alkali source with

high-temperature anodic bonding, has excellent MEMS compatibility, internal atmosphere quality, and process repeatability.

The fabrication process starts by etching 700 μm cavities in a 1 mm thick Si wafer, Figure 4.11-(a). Next, the first anodic bonding seals the etched cavities under atmospheric pressure, Figure 4.11-(b). After placing the wafer stack in a high-temperature furnace at 850 °C for Borosilicate glass (Pyrex) and 1000 °C for Aluminosilicate glass (ASG) for 5-7 minutes, spherically shaped glass shells are formed, [34], Figure 4.11-(c). The formation was due to two effects: the trapped air inside the cavities builds up the pressure due to the temperature increase, and the glass transitions from a solid state to a viscous state.

The next steps in the process are to open the backside of Si wafer and to define 100μm deep micro-channels using Deep Reactive Ion Etching (DRIE), Figure 4.11-(d). Subsequently, the cell coating was applied via atomic layer deposition (ALD) of 10 nm aluminum oxide (Al_2O_3) to the opened cells and the capping wafer, Figure 4.11-(e).

The second anodic bonding took place after the alkali dispenser pills have been placed in the central cell, with the ALD Al_2O_3 as an intermediate layer between the backside of the Si wafer and the capping glass wafer, Figure 4.11-(f). The wafer alignment for bonding was performed inside a chamber with a noble gas and a buffer gas at pressures of 250-350 Torr, Figure 4.11-(f). After the bonding process was complete, each dispenser was activated by focusing a 3.5-4W laser for 15 seconds, which released the alkali vapor to satellite cells, Figure 4.11-(g).

4.4.3 Design of Experiment

The study aims to test the effects of different materials and surface coatings on relaxation time of Xe atoms by isolating all factors that affect the relaxation, except for the effect of

wall interactions. Three samples were fabricated. The first (PXE01) was fabricated using Borosilicate glass (Pyrex) and was utilized as a baseline in our study; the second (PAXE01) was made with Pyrex and coated using Atomic Layer Deposition (ALD) of 10nm Aluminum Oxide (Al_2O_3); the third (HXE02) was fabricated using Aluminosilicate glass (ASG). To isolate other factors beside cell walls, the samples were filled with similar amounts of noble and buffer gases, and were tested under the same conditions of temperature and magnetic field levels. Optical heating was used to minimize any interference from resistive heaters.

The pressure values at room temperature were 65 Torr, 45 Torr, and 300 Torr for natural Xe, Ne, and N_2, respectively. A data fitting of the Rb absorption curve (obtained by sweeping the wavelength of the VCSEL beam passing through the cell) was used to confirm the amount of noble and buffer gasses inside the cell. Measurements showed a reduction of the N_2 gas pressure by 20%-30%, which was attributed to absorption by the getter material in the Rb pill. The experimentally measured relaxation time (T_2) of ^{129}Xe and ^{131}Xe isotopes were used to compare cells. The cells were heated optically using a 2.5W laser source at 1550nm, focusing only on the Si part of the cell substrate. We used the free induction decay (FID) method to estimate the relaxation rate using a dual beam scheme, one for pumping and another for detection, Figure 4.13. The FID experiment was performed by applying a static magnetic field B_0 along the pump axis, the z-axis in this case, which will cause the nuclear spins to precesses at their Larmor frequency ω_L about the z-axis, then applying a $\pi/2$ pulse with a frequency ω_a equal to the ω_L of the isotope of interest on a perpendicular axis to the pump axis, the y-axis here. The pulse would abruptly deflect the magnetization vector of the nuclear spins to the xy-plane. A signal proportional to the nuclear spins as they re-align to the pump axis is detected along the y-axis, and an exponentially decaying sinusoidal wave was measured at a frequency equal to the Larmor frequency ω_L and a decay constant proportional to the transverse relaxation time T_2 of the isotope of interest. The detection was carried out by the probe beam which detected precession of the Rb about the effective field caused by the Xe and the applied field.

4.4.4 Gas Content Measurement

Buffer and noble gasses contribute to the Rb transition line by broadening the light absorption spectrum and shifting the frequency of absorption by specific values for each gas, reported in [107] and [102]. The absorption data were fitted to a Voigt profile, which is a convolution between a Gaussian and Lorentzian functions, [127]. The Gaussian function accounts for Doppler broadening, while the Lorentzian function estimates broadening due to collisions with the buffer gas. An approximated Voigt profile is defined as, [127],

$$F(x) = ax + b - \sum_{i=1}^{8} \left[\eta / \left(1 + \left(\frac{x - x_i}{0.5\Gamma_i} \right)^2 \right) + (1 - \eta) \exp \left(\frac{x - x_i}{c\Gamma_i} \right)^2 \right], \tag{4.14}$$

where a and b are parameters of a line, c= $1/(2\sqrt{\ln 2})$, and η is the Lorentzian constant and its value is between 0 and 1. For each of the four ground transitions of ^{85}Rb and ^{87}Rb, x_i is the center frequency of that transition in MHz, Γ_i is the Voigt width of that peak in MHz. The Voigt width is related to the Gaussian and the Lorentzian widths as follows, [95],

$$\Gamma_V = 0.5346\ \Gamma_L + \sqrt{0.2166\ \Gamma_L^2 + \Gamma_G^2}, \tag{4.15}$$

where Γ_V, Γ_L, Γ_G are the Voigt, the Lorentzian, and the Gaussian widths, respectively.

The Rb dispenser that was used in our process consisted of a pure alkali metal and a getter material (SAES St 101). Once the dispenser is activated, the alkali metal is released, and the getter material absorbs active gasses, such as O_2, H_2, CO, and N_2. To estimate the amount of remaining N_2 gas, we filled an additional cell with 300 Torr of only N_2 gas. We split a laser beam in half and passed the two beams, one through a reference cell with only natural Rb and the other through our fabricated cell, with Rb and other gasses. By sweeping the laser wavelength, we obtained two Rb light absorption spectrum curves, one

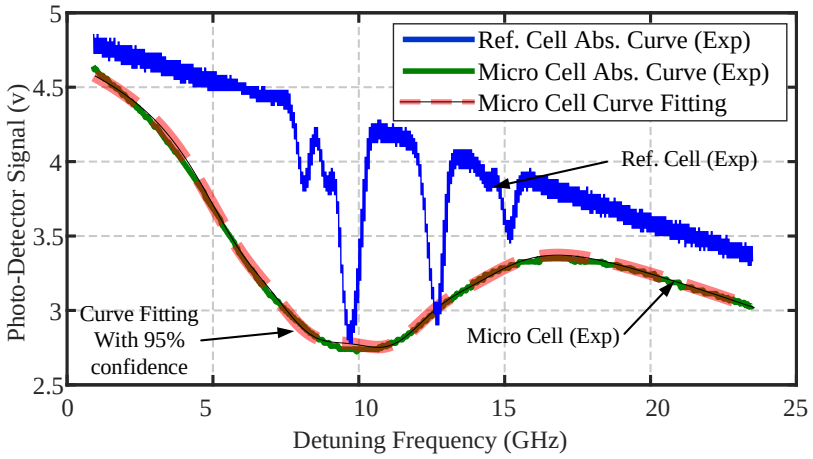

Figure 4.12: Measured Rb absorption curve for the reference cell (blue) shows multiple distinguishable absorption peaks. Measured absorption of a micro cell (green), the cell was filled with 300 Torr of only N_2 and Rb, which broadened and shifted the peaks. In curve fitting to the micro cell spectrum (dashed red), the width of the curve represents 95% confidence bounds, which confirmed a close fit to the experimentally measured data.

for the reference cell, where the two ground transitions of each isotope ^{85}Rb and ^{87}Rb can be distinguished, the other is for the fabricated cell, where these transitions are broadened and shifted due to the N_2 gas, [107, 102]. Starting with the Rb light absorption spectrum of the reference cell and substituting for the broadening and frequency shift rates of N_2 in an iterative curve fitting, we were able to find the N_2 pressure that matched Rb light absorption spectrum curve of the fabricated sample. Fig. 4.12 shows the experimentally obtained Rb absorption curves for the reference cell, microcell with only Rb and N_2, and the curve fit that satisfies the estimated N_2 gas pressure inside the cell. We measured the N_2 gas after two weeks of activation and found that the getter material in the Rb pill was saturated after absorbing 20% of the N_2 gas, [108]. Note that this particular getter absorbs gasses at different rates. The relative sorption rates of H_2, O_2, N_2 compared to CO are 50×, 6×, 0.5×, respectively, [98]. Absorbing other active gases faster than N2 ensures a clean environment inside the cell.

It should be noted that this method of estimating the gas inside the cell has uncertainty associated with the spin destruction cross-section between Rb and other gases, which affect

the broadening and frequency shift constants. The spin destruction cross-section used in our curve fitting was adopted from [107] and [102].

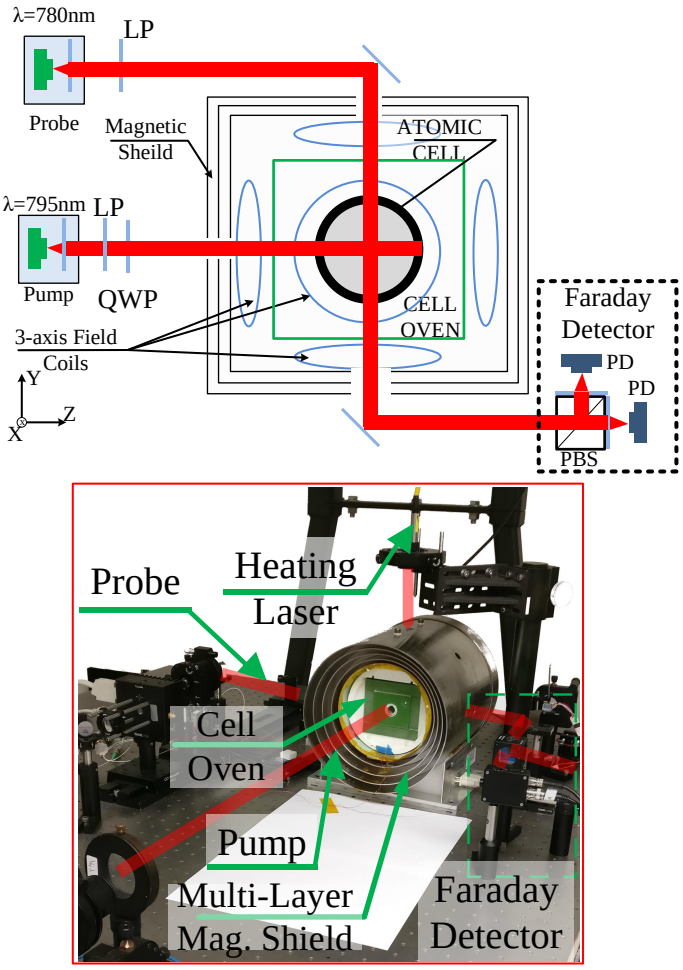

Figure 4.13: Top: Dual beam optical setup for characterization of cells. (LP: linear polarizer, QWP: quarter wave plate, PBS: polarizing beam splitter, PD: photo detector, Faraday Detector: a balanced polarimeter used to detect Faraday rotation). Bottom: Picture of the experimental setup showing the pump, probe, and the heating laser beams, as well as the nested magnetic shields and the cell oven.

4.4.5 Experimental Setup

The atomic cell was placed in a miniaturized oven made from a thermally insulating material, all housed by a nested 4-layer μ-metal shield with integrated 3-axis magnetic field

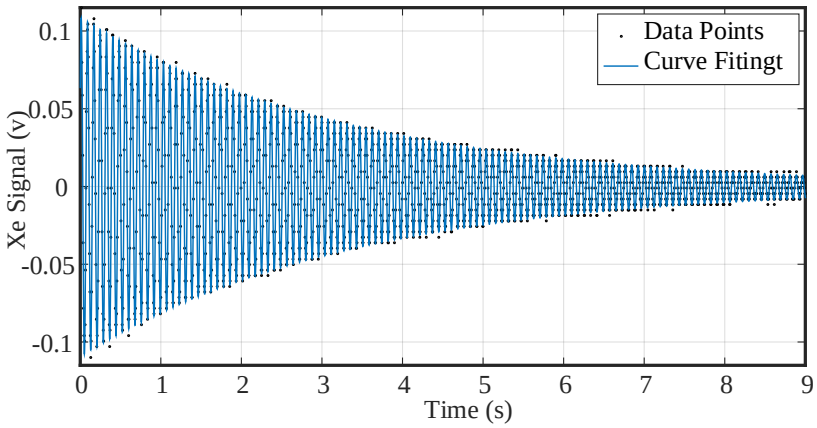

Figure 4.14: Example of FID signal of ^{131}Xe isotope recorded from a sample PAXE01 (Pyrex coated with 10nm ALD Al_2O_3).

coils. The pump beam of 2.5mW with a circularly polarized light locked on Rb D1 line (795nm) along the z-axis. A DC field of 3.5μT and an RF field of 17.8kHz with an RMS amplitude of 3.5μT were applied along the z-axis. The probe beam was a linearly polarized beam of 1mW set off resonance from D2 line (780nm) and was applied along the y-axis. The produced RF signal was used as a reference for the lock-in amplifier that demodulated the output of the Faraday detector at the probe side (Faraday Detector is a balanced polarimeter used to detect Faraday Rotation). A $\pi/2$ pulse at the frequency of the Xe isotope of interest was applied along the y-axis to obtain the FID signal, which was fitted to an exponentially decaying sine wave to extract the relaxation time T_2. Figure 4.14 shows an example of the FID signal for ^{131}Xe of PAXE01.

4.4.6 Coating

Alkali metals, like Rb, react with glass cells at elevated temperatures, which leads to a consumption of the metal. One method to reduce this interaction is by passivating the glass walls of the cells. In [128], it was shown that a 20nm layer of Al_2O_3 can reduce the interaction between alkali metals and cell glass walls by 100x. It was also found that anodic bonding, the process used for fabrication of the cells, worked with ALD Al_2O_3 as an intermediate

layer.

ALD is a thin film conformal coating technique, the reaction of two chemicals in a gas phase with a surface creates one atomic layer, for example, Trimethylaluminum (TMA) and H_2O creates Al_2O_3. The process is self-limiting to a single atomic layer per cycle. The coating is achieved by repeating deposition cycles until the desired thickness is reached. In our study, we used a commercial ALD deposition system by Cambridge Nanotech to deposit 10 nm of Al_2O_3, on both samples and the capping wafer. The deposition parameters are summarized in Table 4.3.

Table 4.3: Summary of ALD Al_2O_3 deposition parameters

	pulse time(s)	**purge time(s)**	$\mathbf{N}_{cycles}$	**N_2 rate [sccm]**	**Temp (°C)**
TMA	0.015	10	100	20	200
H_2O	0.05	10	100	20	200

4.4.7 Results

Table 4.4 summarizes the studied parameters and the average relaxation time of ^{129}Xe and ^{131}Xe isotopes in the range from 115°C to 140°C. We observed that Atomic Layer Deposition (ALD) of 10 nm Al_2O_3 on the cell walls increased the transverse relaxation time of the ^{131}Xe isotope by a factor of 4.7x, when compared to cells without coating. When using Aluminosilicate glass (ASG) instead of Borosilicate glass (Pyrex), we observed a similar effect on the relaxation time of ^{131}Xe isotope, demonstrating an increase of T_2 by a factor of 3.2x. We did not observe the quadruple frequency splitting with the ^{131}Xe in any of the micro-glassblown cells. We believe this is due to symmetry of the cells and the fact that the active area of the cell is made from the same material, which agrees with conclusions in [31]. On the other hand, ALD coating of Al_2O_3 was found to reduce the relaxation time of the ^{129}Xe

isotope by a factor of 2x, while the ASG glass did not show a significant difference in T_2 of ^{129}Xe, as shown in Table 4.4.

Table 4.4: summary of cells used in this study and the corresponding relaxation times of each isotope

Cell	**PXE01**	**PAXE01**	**HXE02**
Glass	Pyrex	Pyrex	ASG
Coating	n/a	10nm Al_2O_3	n/a
^{129}**Xe** T_2**(s)**	1.4	0.79	1.2
^{131}**Xe** T_2**(s)**	0.74	3.55	2.35

4.4.8 Discussion

Reduction of the relaxation time of the ^{129}Xe isotope in PAXE01 (ALD Al_2O_3 coated cell) is believed to be due to a magnetic field gradient inside the cell created by non-uniform pumping of Rb atoms. This pumping non-uniformity is a result of different beam bending angles as it transmits through the cell, which was discussed earlier in section 4.3. Vertical pumping and in-plane probing of the same sample showed an increase of relaxation time to 1.22s, which is on par with PXE01, and that supports our hypothesis.

To analyze improvements of the relaxation time constant of ^{131}Xe, we performed Fast Fourier Transform (FFT) to the FID signal of ^{131}Xe of the three cells at temperature of 135°C. Subsequently, the FFT data were fitted with a triplet of Lorentzian functions. Table 4.5 summarizes the data fitting results. We observed two phenomena. The first observation is that the ALD Al_2O_3 coating and ASG glass suppressed quadrupole splitting by reducing the splitting frequency between the three peaks by 100× and 2.2×, respectively. The second observation is that ALD coating of AL_2O_3 and the use of ASG glass material reduced the width of the central peak by 3.2× and 2.5×, respectively. Figure 4.15 shows FFT of FID signals of the three cells.

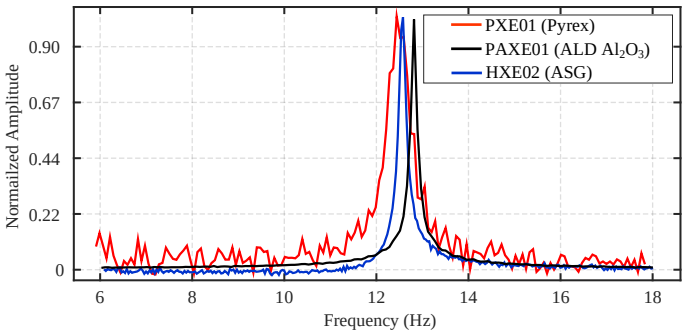

Figure 4.15: FFT of the ^{131}Xe FID signal of PXE01(red), PAXE01(black), and HXE02(blue).

Table 4.5: Data fitting results of FFT of the ^{131}Xe FID signal to triplet Lorentzian peaks for three cells.

	Splitting (mHz)	Central Peak width (mHz)	Fitting RMSE
PXE01	153	509	4%
PAXE01	1.5	161	0.4%
HXE02	69.5	195	1.2%

4.5 Conclusion

This Chapter discussed different design considerations of micro-glassblown spherical cells for atomic sensors applications. These aspects included geometry, optical properties, material selection, and surface coating. We studied cell inner wall coating as well as cell glass materials. We found that 10nm ALD Al_2O_3 suppressed the quadrupole splitting of ^{131}Xe by 100× and reduced the central frequency peak width by 3×, which was observed as 4.7× increase in the relaxation time. We also found that using ASG glass instead of Pyrex suppressed the quadrupole splitting of ^{131}Xe by 2.2× and reduced the central frequency peak width by 2.5×, which was observed as 3.2× increase in the relaxation time. We concluded that the ALD Al_2O_3 coating and the ASG glass did not have a significant impact on the T_2 of ^{129}Xe. In light of the experimental results and analytical models of NMRG ARW, [42], the NMRM fundamental sensitivity δB_n, [20], and assuming the same SNR values, the Al_2O_3 coating is projected to reduce the NMRG ARW and NMRM δB_n by more than fourfold.

Chapter 5

Reconfigurable Analog Emulator: a Tool for Development of NMR Atomic Sensors

This chapter presents an analog emulator for NMR atomic sensors. The emulator represents the spin dynamics of atoms in an applied magnetic field that are governed by Bloch equations. The principle of operation and the mathematical model that is represented by the emulator were described in Chapter 2. The first section of this chapter presents a design flow of the emulator and its sub-blocks. The second section presents an experimental evaluation of emulator functionality.

5.1 Emulator Design

In this section, we introduce the emulator design and highlight its main building blocks. The emulator is set to represent a mathematical description of the magnetization vector

dynamics, captured by equations (2.28), (2.29) and (2.30), to a circuit representation. In our implementation, a magnetic field amplitude of 1 micro-Tesla corresponds to 1 volt. Each component of the magnetization vector is represented by a single analog computer that solves the corresponding differential equation, Fig. 5.1-(insert). These computers were interconnected to represent the three components of the magnetization vector, Fig. 5.1.

5.1.1 Emulator building blocks

Each analog computer is composed of multiple sub-blocks, these are multipliers, scalar gains, a summing block, an integrator, and a feedback network. The emulator inputs are the constant magnetic field B_0, the oscillating field $B_1 \sin \omega_a$, and the amplitude of the magnetization vector M_0. Next, we will briefly describe theses blocks for the X-axis sub-circuit.

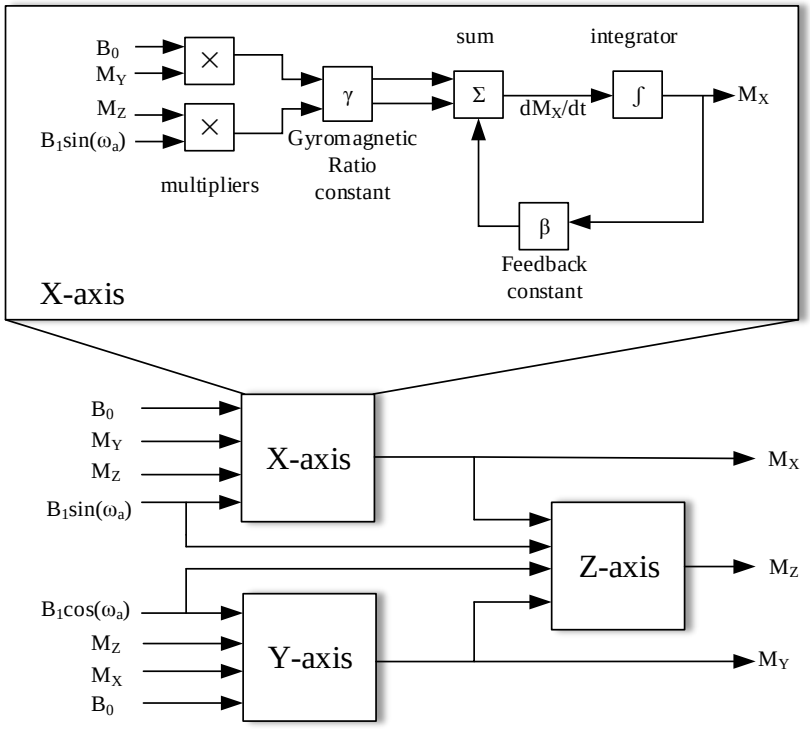

Figure 5.1: Block diagram representation of Bloch equations, where the output of X, Y, and Z represent the magnetization vector components. Insert shows a block diagram example of the X-axis component.

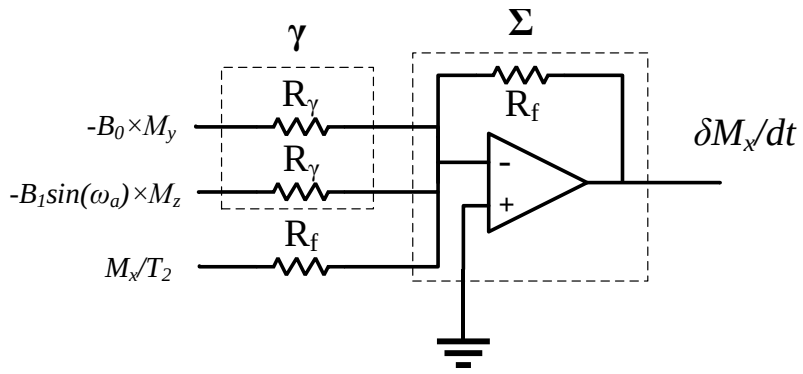

Figure 5.2: Circuit schematic of Σ and γ blocks in Fig. 5.1-insert

Off-the-shelf analog multipliers (TI-MPY634) were used to multiply the inputs B_0 and $B_1 \sin \omega$ by the magnetization vector components M_y and M_z. The output of the multipliers was then connected to the scalar gain γ (gyromagnetic ratio). Scaling the outputs of the multipliers by γ was carried out by selecting the input and the feedback resistors of the summing amplifier (R_γ and R_f in Fig. 5.2), such that the amplifier gain is

$$A_v = -\frac{R_f}{R_\gamma} = -\gamma \tag{5.1}$$

After the scalar gain, the signals were passed to the summing block (Σ in Fig. 5.2), which was an inverting summing op-amp. The output of the summing op-amp, which is the time derivative of the X-axis component of the magnetization vector, was passed to an integrator to calculate the time integral of the signal.

An Ideal op-amp integrator is shown in Fig. 5.3-(a), and its output is described as

$$V_{out} = -\frac{1}{R_{in}C_{int}} \int_0^T V_{in} dt, \tag{5.2}$$

where R_{in} is the input resistance and C_{int} is the negative feedback capacitor. However, due to nonidealities in op-amps, a slight input offset voltage (VOS) will saturate the op-amp, and a manual discharge of the capacitor would be required. A practical integrator design includes a large resistor in parallel with the feedback capacitor, as seen in Fig. 5.3-(b). The practical

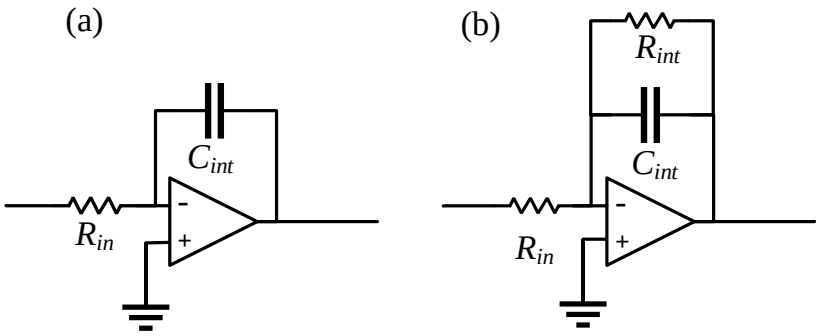

Figure 5.3: Ideal and non-Ideal integrator circuit

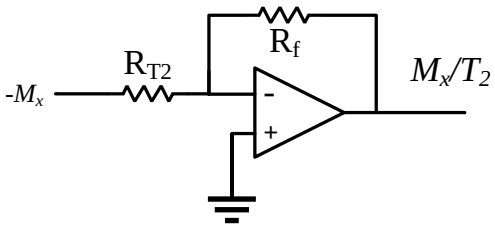

Figure 5.4: Circuit schematic of β block in Fig. 5.1-insert

integrator has a frequency response similar to that of a low-pass filter. The integrator has a lower cut-off frequency below which it works as a constant gain, that prevents the op-amp from saturating due to DC input offset voltage. A critical aspect of integrator design is the RC constant. It is essential to consider the RC constant to avoid systematic errors in calculations.

Once the signal has been integrated, the output was connected to the feedback network β and fed back to the summing op-amp. Simultaneously, the integrated output was connected as an input to the Y-axis and the Z-axis circuits. The feedback scaling of the X-axis and Y-axis circuits was accomplished by selecting the feedback and input resistors of the β network, such that $R_{f_2}/R_{T_2} = T_2^{-1}$, as shown in Fig. 5.4.

The complete schematic of the emulator is shown in Fig. 5.5. For M_z, the β network is a differential op-amp that outputs the relaxation term of equation (2.30). Note that the output of the emulator sub-circuits are inverted outputs and an optional inversion step can

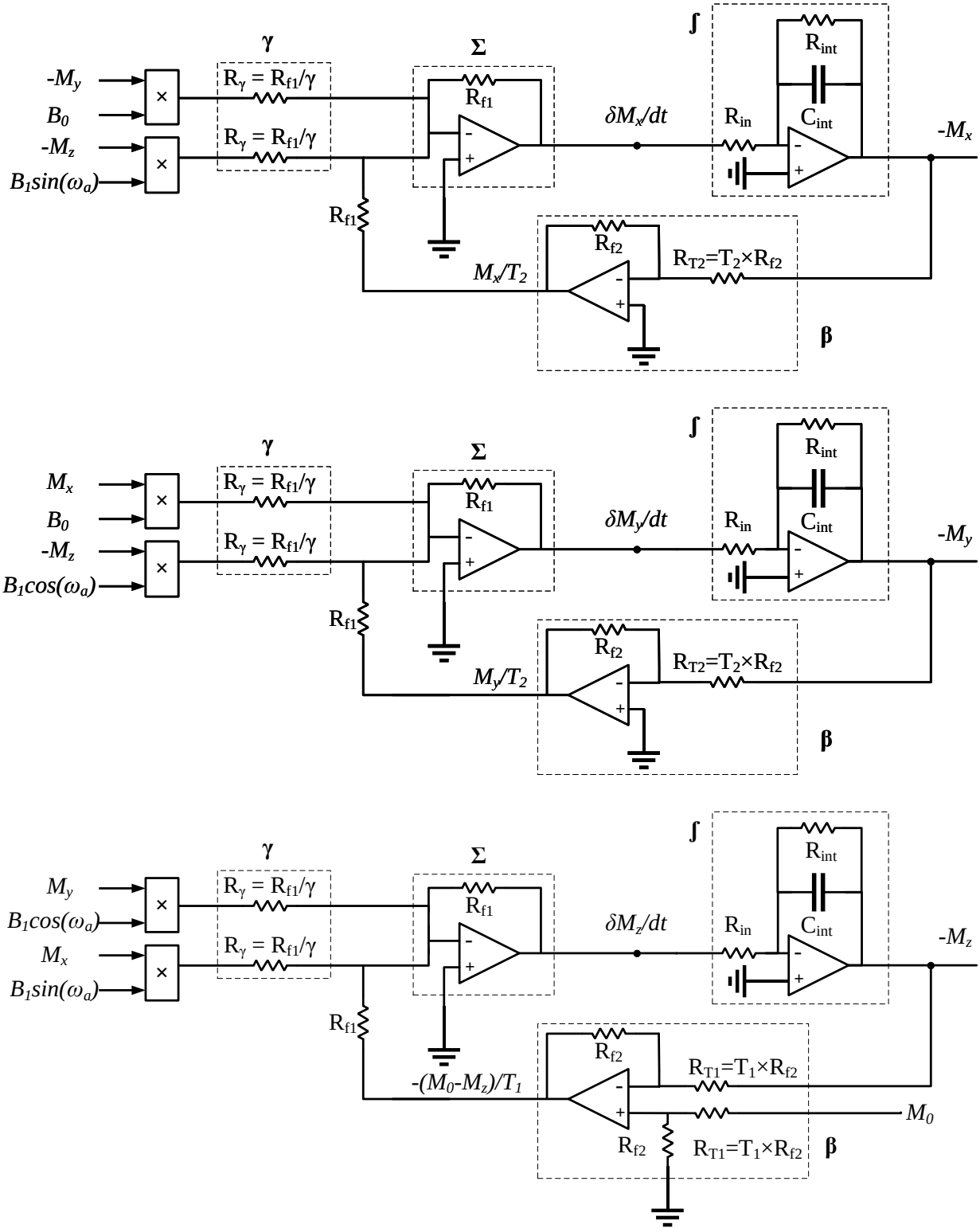

Figure 5.5: Schematic diagram of the emulator showing M_x, M_y, and M_z circuits

be carried out by choosing the inverting input of the multiplier.

5.1.2 Emulator voltage gain and feedback constant

In NMR systems, M_0 is the magnitude of the magnetization vector, and it is representative of a number of polarized atoms in the system, as shown by the analytical solution of equations (2.42), (2.43) and (2.44). For the emulator, this can be viewed as the voltage gain of the output to the input (M_x, for example, and B_1). This voltage gain is controlled by the M_0 constant in the feedback network of M_z circuit in Fig. 5.5.

The relaxation terms in equations (2.28), (2.29) and (2.30) are representations of how long the atoms can preserve their polarization. By analogy, the negative feedback networks β in M_x, M_y, and M_z control the loss of the signal in the emulator circuits. The β networks in M_x and M_y circuits are proportional to the transverse relaxation time constant T_2, while the feedback network β in M_z is proportional to the longitudinal relaxation time constant T_1.

5.2 Experimental Results

In this section, we present an experimental validation of the NMR sensor emulator, discuss its noise characteristics, and compare it to an actual NMR system. We show the validation of equation (2.7), absorption and dispersion modes, predicted by the analytical solution equations (2.42) and (2.43), relaxation time control, emulator voltage gain control, and steady-state response (if the forcing was continuously applied) of the emulator to different drive B_1 amplitudes. We characterized the emulator noise by interfacing it with a simplified control loop implemented on a digital platform dSPACE. Finally, we show the absorption and dispersion curves of the NMR sensor emulator and an actual NMR system. The emulator

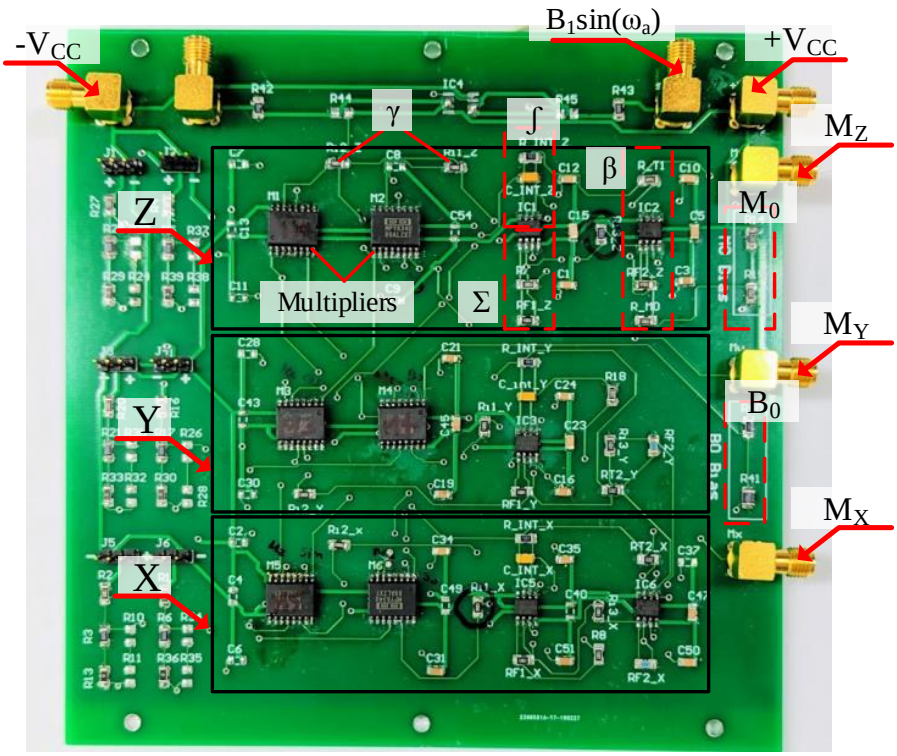

Figure 5.6: PCB prototype of emulator showing input and output ports and (X, Y, Z) sub-circuits

parameters used in the experimental validation are summarized in Table 5.1.

5.2.1 Validation

Larmor Frequency

The frequency response of the emulator was obtained using the signal spectrum analyzer by applying a constant B_0 value and sweeping the frequency of the drive signal $B_1 \sin(\omega_a)$. Fig. 5.7 shows an example of the emulator frequency response of M_x for $B_0 = 4V$ and γ= 10 $rad.s^{-1}/V$. This experiment was repeated for different values of the static field B_0 from 1V to 14V. We were able to verify the linear relationship between the applied B_0 and the observed frequency, and the slope of the line was equal to the set value of γ. Fig. 5.8 shows the Larmor relationship for three different γ values.

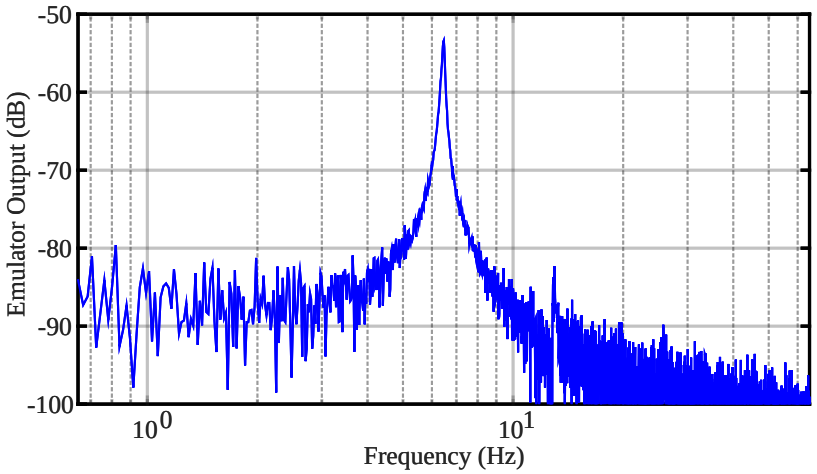

Figure 5.7: Example of the emulator frequency response. B_0=4V, $B_1 = 2mv_{pp}$, $\gamma = 10\ rad.s^{-1}/V$, T_2=2s.

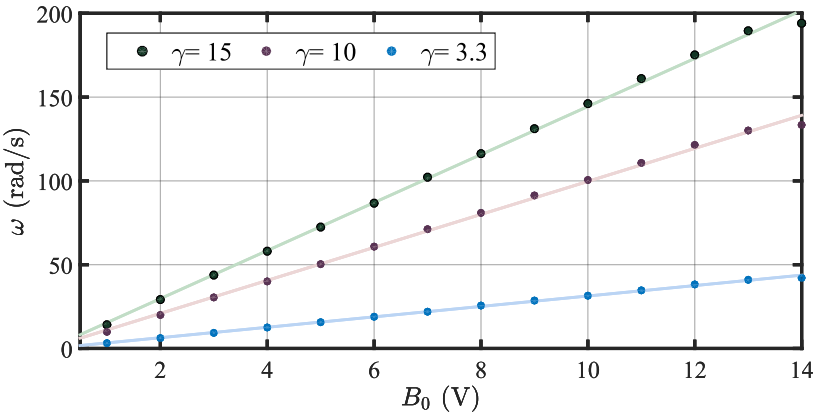

Figure 5.8: Measured frequency response of the emulator in response to B_0 change for different gyro-magnetic ratio values

Table 5.1: Summary of parameters used in emulator design for experimental validation

Parameter	**unit**	**value**
R_{int}	Ω	1 M
R_{in}	Ω	100K
C_{int}	μF	10
γ	$rad.s^{-1}/V$	10
T_1	s	10
T_2	s	2
R_{F1}	Ω	1k
R_{F2}	Ω	1k
M_0	V	12
B_0	V	7.714
B_1	mv	1
Op-amp	ADA4077	
multiplier	Ti MPY634	

Absorption and Dispersion

The general behavior of the magnetization vector in a rotating frame was predicted by equations (2.42) and (2.43). To verify that the emulator resembles the analytical model, we applied a small driving signal B_1=10mv and swept its frequency from 9Hz to 13.5Hz. The emulator output M_x was connected to a lock-in amplifier to demodulate M_x at the frequency of the swept signal. Fig. 5.9 shows that the experimentally measured absorption and dispersion curves of the emulator (solid lines) and the analytical model prediction (dashed lines) are in a close match.

Relaxation time T_2

NMRG emulator provides the option to set different values for relaxation time, by changing the gain of the feedback network, β in Fig. 5.1, as it was described in the previous section. To measure the emulator's relaxation time we conducted an experiment similar to the Field Induction Decay (FID), which is used in NMR, where a constant B_0 and a

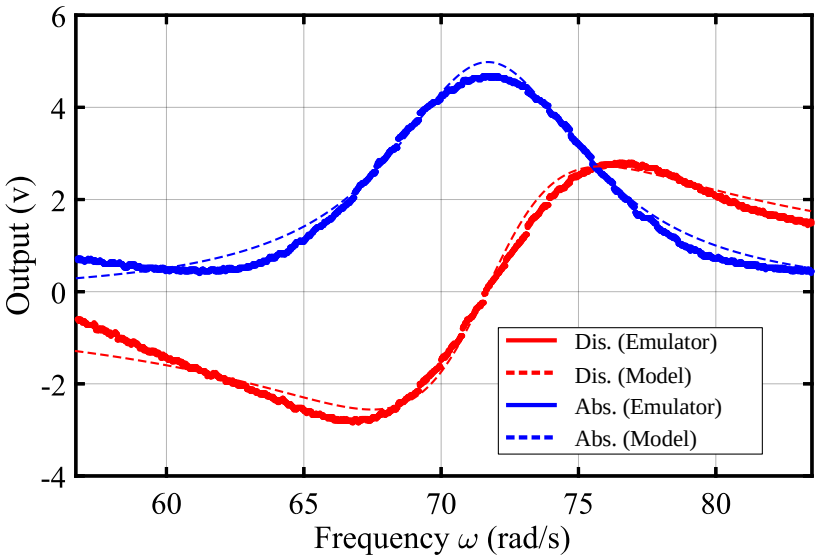

Figure 5.9: Absorption and Dispersion modes obtained experimentally from the emulator. B_0=7.71V, γ =10, T_1=10s, T_2=2s.

sinusoidal B_1 with a frequency equal to the Larmor frequency are applied. After 30s, B_1 was switched off and the transient output of the emulator (M_x or M_y) was recorded and then fitted to an exponentially decaying sinusoidal wave to extract T_2. Fig. 5.10 shows an example of the emulated FID signal.

This experiment was then repeated for different T_2 settings, (T_2=2, 4, 14, and 32s) and corresponding envelopes of the decaying signals are presented in Fig. 5.11.

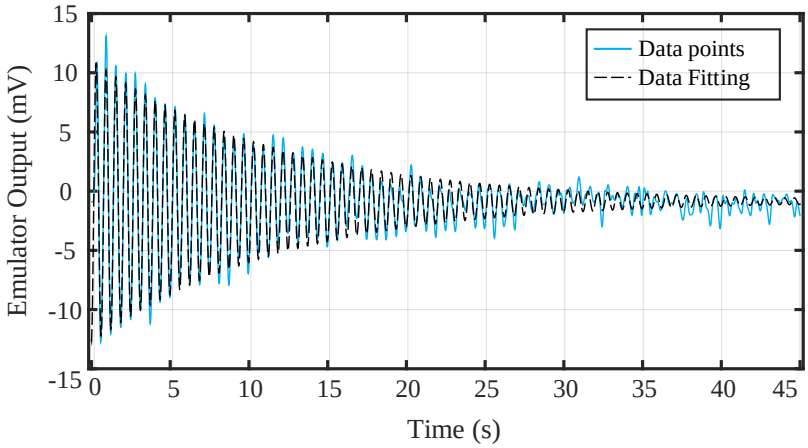

Figure 5.10: Emulated FID signal showing an exponentially decaying sinusoid, T_2=11s.

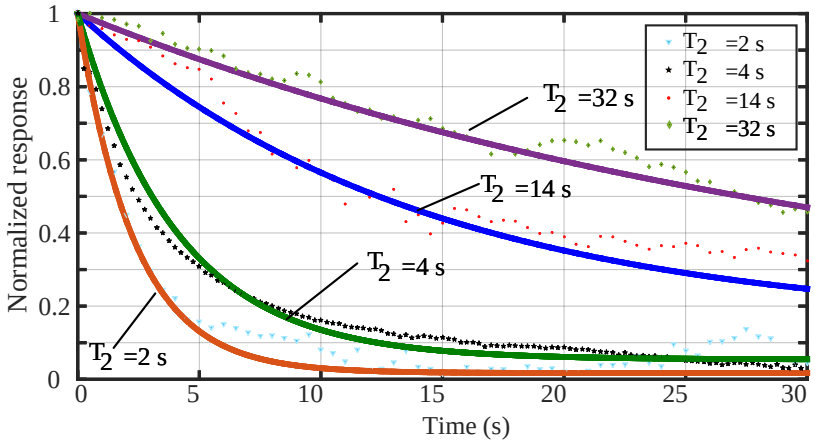

Figure 5.11: Measured relaxation time of the emulator for different T_2 settings. T_2=2s (orange), T_2=4s (green), T_2=14s (blue), and T_2=32s(purple).

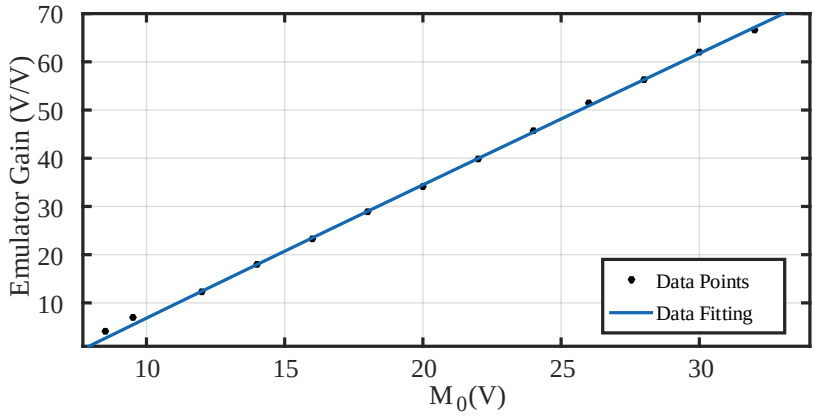

Figure 5.12: Emulator voltage gain vs. M_0. This voltage gain is the ratio of the emulator output M_x to its input B_1.

Emulator gain

As described in the previous section, the emulator gain can be adjusted by modifying the value of M_0. A constant B_0 and an oscillating $B_1 \sin(\omega_a t)$ were applied to the emulator. Using the signal spectrum analyzer, we swept the frequency of the drive signal (B_1) and extracted the voltage gain of the emulator (this gain is the ratio of the emulator output M_x to its input B_1). Fig. 5.12 shows the experimentally measured voltage gain vs. M_0.

Transient response

The driving field amplitude of B_1 plays a crucial role in determining the amplitude of the xy-plane component of the magnetization vector. With the goal to maximize the amplitude of the xy-component of the magnetization vector and to minimize the time required to reach the steady-state, we studied the transient of M_x under different B_1 values. Fig. 5.13 shows the emulator transient response of M_x for B_1 amplitudes of 1mv, 2mv, 3mv, 5mv, and 10mv, illustrating an increase in steady-state amplitude as well as ringing of the M_x with the increase of B_1 amplitude, as predicted by the model.

5.2.2 Noise Characteristics

The next step of the emulator design was to test its noise characteristics. We implemented a simplified version of the control loop presented in [45] on dSPACE digital platform to drive and control the emulator. Fig. 5.14 shows a block diagram that highlights main parts of the control loop. The control loop supplies the emulator with input signals B_0 and $B_1 \sin \omega_a$ and it reads the emulator's outputs M_x, M_y, and M_z. At the control loop input, a phase-locked loop (PLL) locks onto the emulator frequency ($\omega_a = \gamma B_0$). The voltage-controlled oscillator (a sub-block of the PLL) generates the $B_1 \sin \omega_a$ signal that drives the

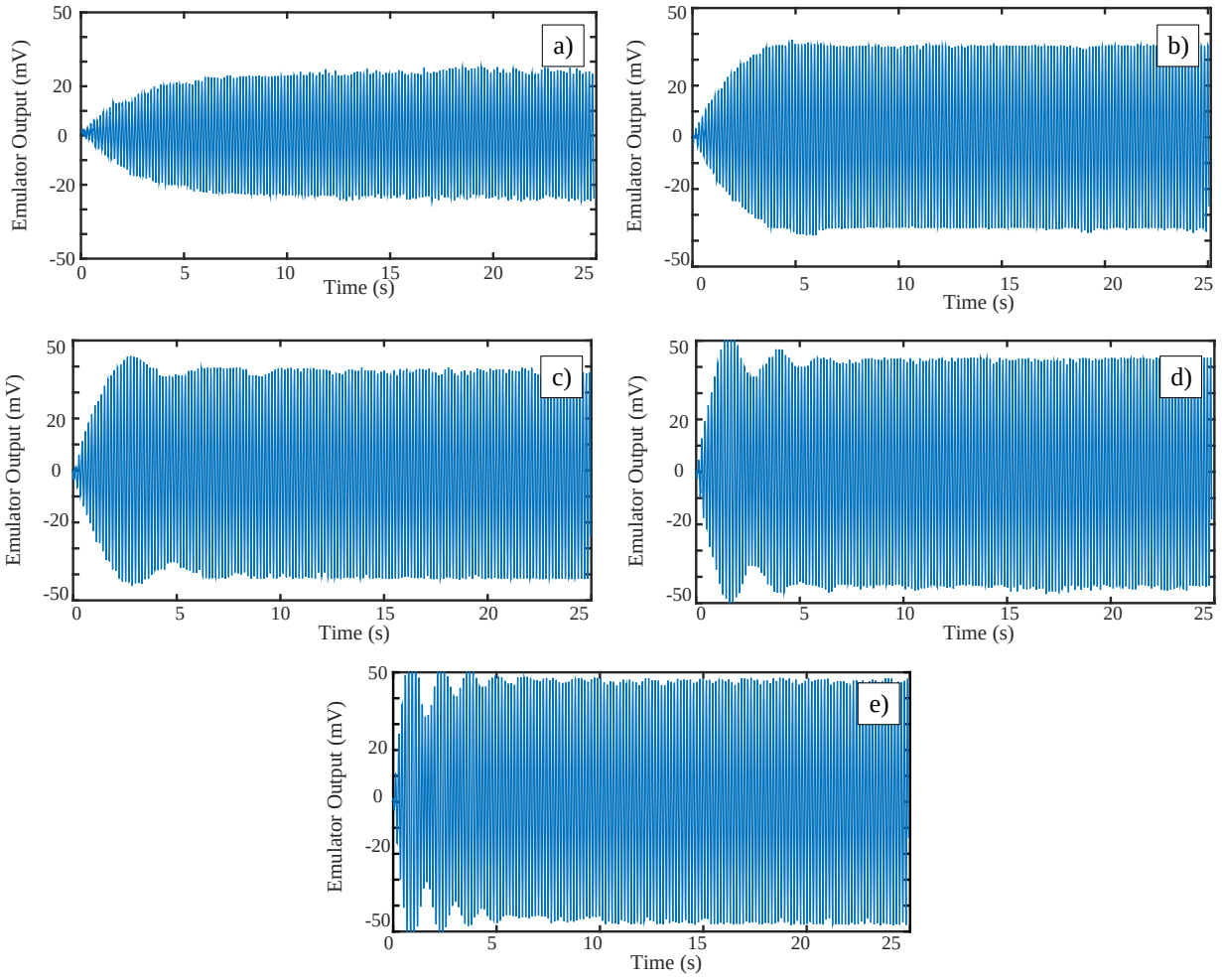

Figure 5.13: Emulator response (M_x) to different B_1 amplitudes, a) B_1=1mv, b) B_1=2mv, c) B_1=3mv, d) B_1=5mv, e) B_1=10mv. Increasing B_1 increases steady-state amplitude and ringing.

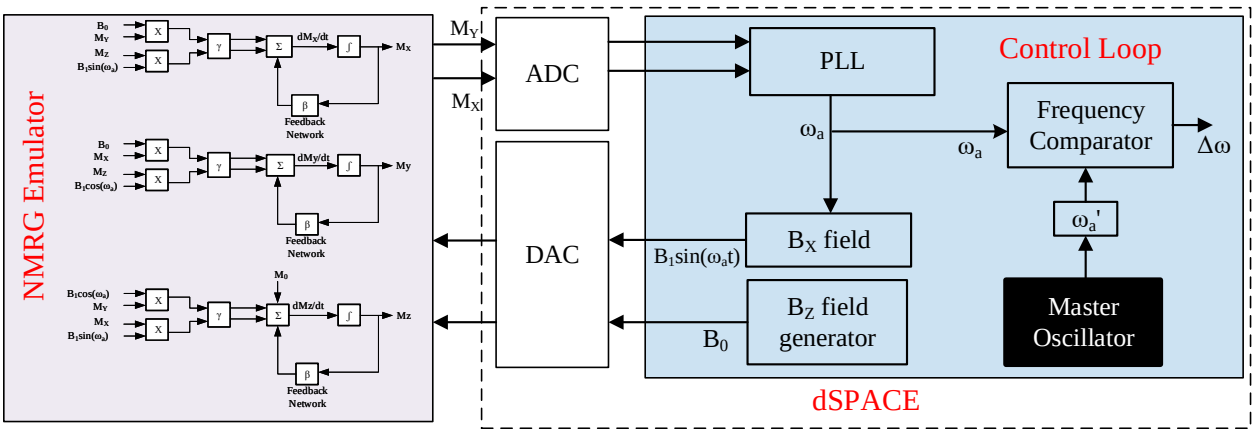

Figure 5.14: Block diagram shows emulator circuit and the control loop implemented on dSPACE, the control loop was reproduced from [45].

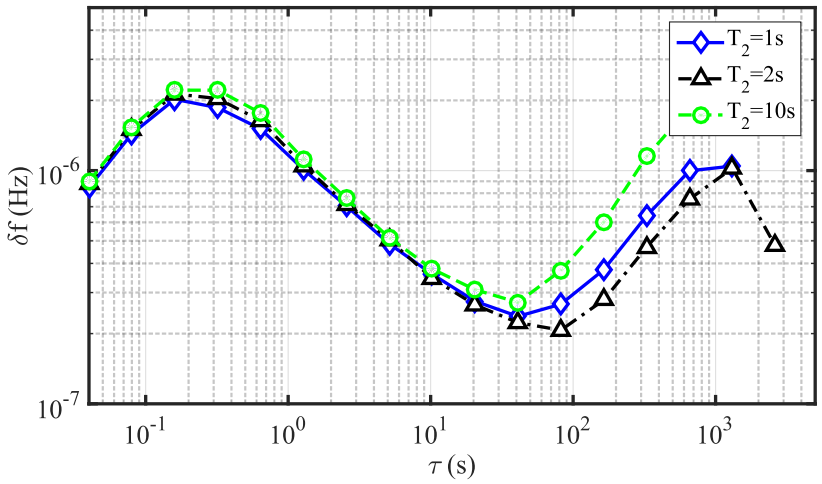

Figure 5.15: Allan deviation plot (ADEV) for different T_2 settings. T_2=1s (blue diamond), T_2=2s (black triangles), T_2=10s (green circles). For all 3 curves, M_0=12V

emulator at resonance. A frequency comparator was used to detect the frequency shift, $\Delta\omega$ in Fig. 5.14, of the emulator vs. a reference frequency set by the master oscillator.

The frequency stability of the emulator was measured for different Signal-to-Noise Ratio (SNR) and T_2 values. SNR was modified by changing the M_0 value, while T_2 was modified by changing the gain of the β block in M_x and M_y circuits, as was described in Sec. 5.1. Allan deviation (ADEV) plots of $\Delta\omega$ for different T_2 and SNR settings are presented in Fig. 5.15 and Fig. 5.16, respectively. Both figures show a negligible deviation of the emulator's noise profile for different SNR and T_2 settings. The noise floor of the emulator frequency was within

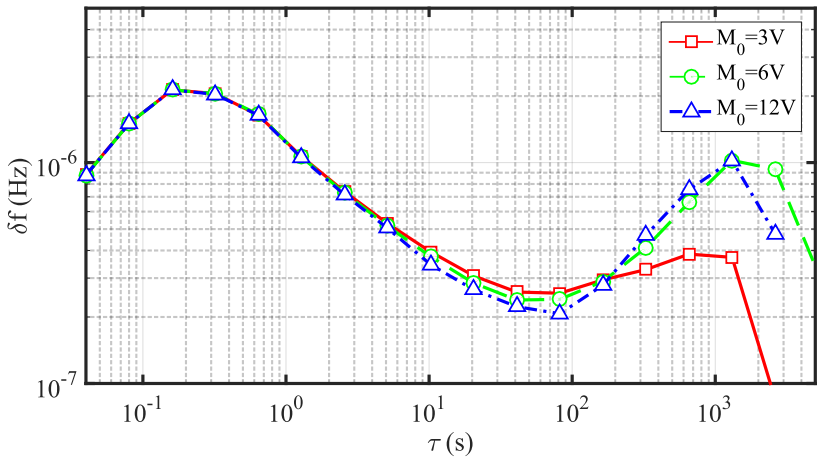

Figure 5.16: Allan deviation plot (ADEV) for different SNR settings. M_0=3V (red squares), M_0=6V (green circles), M_0=12V (blue triangles). For all 3 curves, T_2=2s

1μHz. The noise characteristics of the emulator make of a good candidate for visualization and analysis of the noise propagation through the system from other components of the atomic sensor, such as laser sources, photodetectors, and current generator.

5.2.3 NMR Emulator vs. NMR system

The final experiment of the NMR sensor emulator presented in this chapter was a comparison between its functionality and an actual NMR system. The absorption and dispersion modes were generated experimentally from a physical NMR system for ^{131}Xe that was precessing at $\omega_{Xe} = 2\pi \times 12.4$ rad/s. The relaxation time T_2 for ^{131}Xe in this system was 3s, [93], Fig. 5.17-(solid lines). The same experiment was repeated for the NMR sensor emulator by setting its γ constant close to γ_{131}, $\gamma \approx 2\pi \times 3.52\ rad.s^{-1}/V$ and applying B_0=3.5V, T_2 = 2s, Fig. 5.17-(dashed lines). The two sets of curves were compared to the analytical model response equations (2.42) and (2.43), Fig. 5.17-(translucent lines). Fig. 5.17 shows behavior similarities between both the experimentally measured responses and predictions of the analytical model, with more than 90% matching between the experimental data and the model.

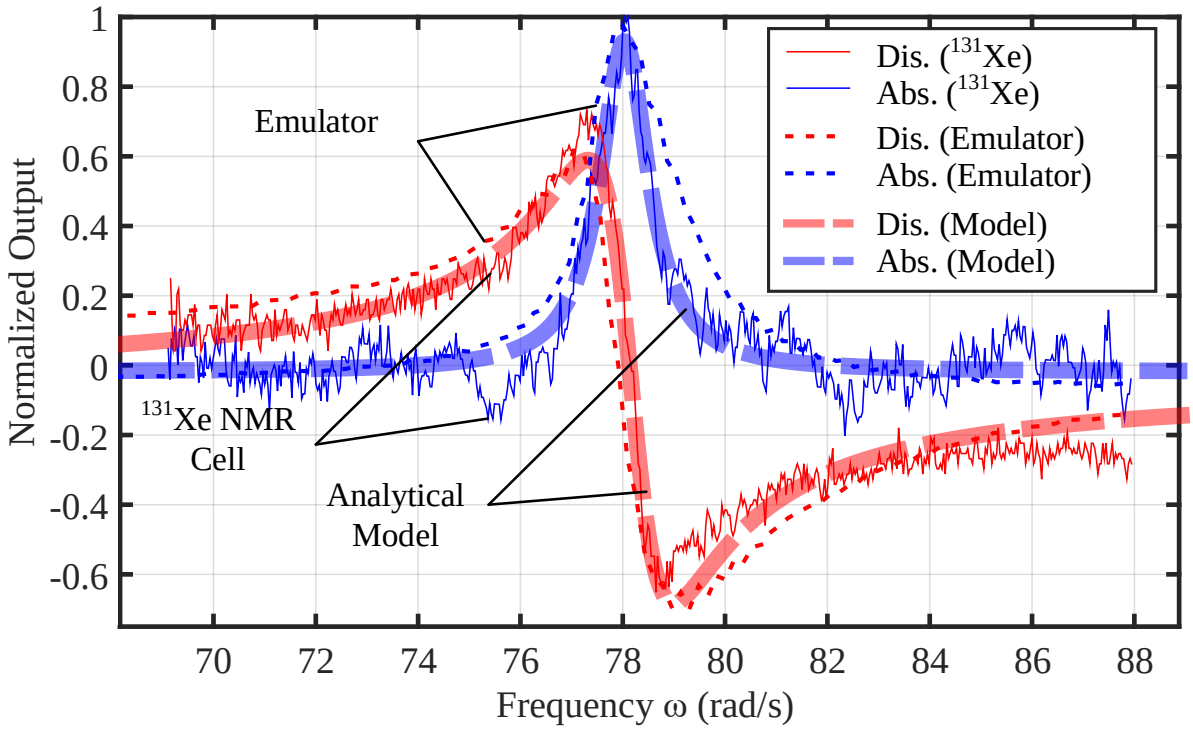

Figure 5.17: Experimentally measured absorption and dispersion curves of an NMR system (solid lines) and an NMR sensor emulator (dashed lines) compared to the prediction by the analytical model equations (2.42) and (2.43) (translucent lines).

5.3 Conclusion

This chapter presented an analog re-configurable emulator for NMR atomic sensors. The emulator is an electronic representation of the phenomenological model of atoms in an applied magnetic field. We presented the design of the emulator sub-blocks. Subsequently, we experimentally validated the emulator's functionality, such as the Larmor frequency, dispersion and absorption modes, and the relaxation time constant. We presented a comparison between the experimentally measured responses of the NMR emulator and an actual NMR system, showing similarities in response of both systems with more than 90% matching to the analytical model predictions. Finally, we showed that noise characteristics were independent of the emulator's relaxation time and SNR settings, which makes it suitable for visualizing noise characteristics of other atomic sensor components in a hardware-in-the-loop configuration.

Chapter 6

Conclusion

Atomic sensors have shown great performance in measuring physical quantities, such as time, rotation, and magnetic field, with high precision on tabletop setups. The emerging applications that require high performance miniaturized sensors sparked the interest in miniaturizing atomic sensors at the beginning of this century. To date, these sensors are assembled by picking and placing of individual components. This limitation can be addressed by developing processes that yield low cost, size, weight, and power sensors while maintaining the expected high performance.

This dissertation explored batch fabrication techniques for development, design, and assembly of atomic sensor components. The limitations of the developed fabrication processes were examined experimentally and verified analytically and using finite element models. An emulator of the atomic spin dynamics was developed for characterization and analysis of the developed atomic sensor components.

6.1 Contribution of the Dissertation

The work in this dissertation takes forward the efforts of previous team members of the NMRG project in the MicroSystems Laboratory. The designs of the 3D folded coils and structures were proposed in [33]. The initial demonstration of the fabrication on flat samples was shown in [46]. A fabrication process of 3D glassblown cells was introduced [34], and the feasibility of using them as atomic cells was presented in [35]. However, the noble gas (Xe) response was not demonstrated before in micro glassblown cells. Leveraging the results of the previous research in the lab, bellow are the contributions of this dissertation.

- Fine-tuning the fabrication process of folded structures, while introducing different polymer material for the hinges that solved the problem of polymer cracking, which limited the component characterization to flat samples in [46].
- Developed and experimentally verified the analytical model that links the folding accuracy to the atomic sensor performance.
- Developed a wafer-level fabrication process of a network of interconnected atomic cells utilizing glassblowing technology.
- Built a custom filling station for filling the cell network samples and sealing them in a controlled atmosphere of buffer and noble gases.
- Demonstrated the feasibility of filling an array of atomic cells simultaneously with noble and buffer gases, and measured the noble gas response as well as the pressure of all gases after sealing. The demonstration of feasibility was carried out by building atomic cells characterization setup capable of measuring nuclear spins of the noble gas. Measuring the noble and buffer gases pressures inside the cell was achieved by adopting methods used for large-sized cells.

- Developed a multi-aspect design process for producing highly spherical glassblown cells within the practical limits of the fabrication process. Identified that the critical design process aspects are geometry, optical properties, surface coating, and material.

- Presented design and validation of an NMR atomic sensor emulator that mimics the dynamics for the noble gas atoms in an applied magnetic field. The emulator was developed for characterization and analysis of the developed components in a hardware-in-the-loop configuration.

- The research presented in this dissertation was published in three peer-reviewed journal articles, [94, 90, 92], and two international conference papers, [91, 93].

6.2 Future Research Directions

NMR Atomic Gradiometer

Atomic gradiometers are gaining popularity in applications that require measuring ultra-low magnetic fields, a better estimation of the spatial field information at the target, and common noise rejection, [113]. These applications include compact non-invasive bio-magnetic imaging such as magnetoencephalography (MEG) and magnetocardiography (MCG). State of the art in the implementations of those gradiometers is using multiple atomic cells filled with a comparable amount of alkali metal and buffer gas and separated by some distance to estimate the field gradient, [118, 113]. Filling the cells with a comparable amount of alkali and buffer gas helps to cancel common noise from the laser source.

A future research direction could be adopting the developed cell network approach for creating atomic gradiometer. The advantage of using interconnected cells is that it ensures a better laser source noise cancellation since the cells are interconnected, and the cells have the

same gas pressure all the time. Additionally, the 3D geometry of the cells provides multiple optical ports for orthogonal pumping and probing of the cells, which gives a better signal-to-noise-ratio (SNR) of the signal as was concluded in [118]. Figure 6.1 shows an example of the characterization setup that can be used to pump and probe multiple cells at the same time and can potentially be used as an atomic gradiometer.

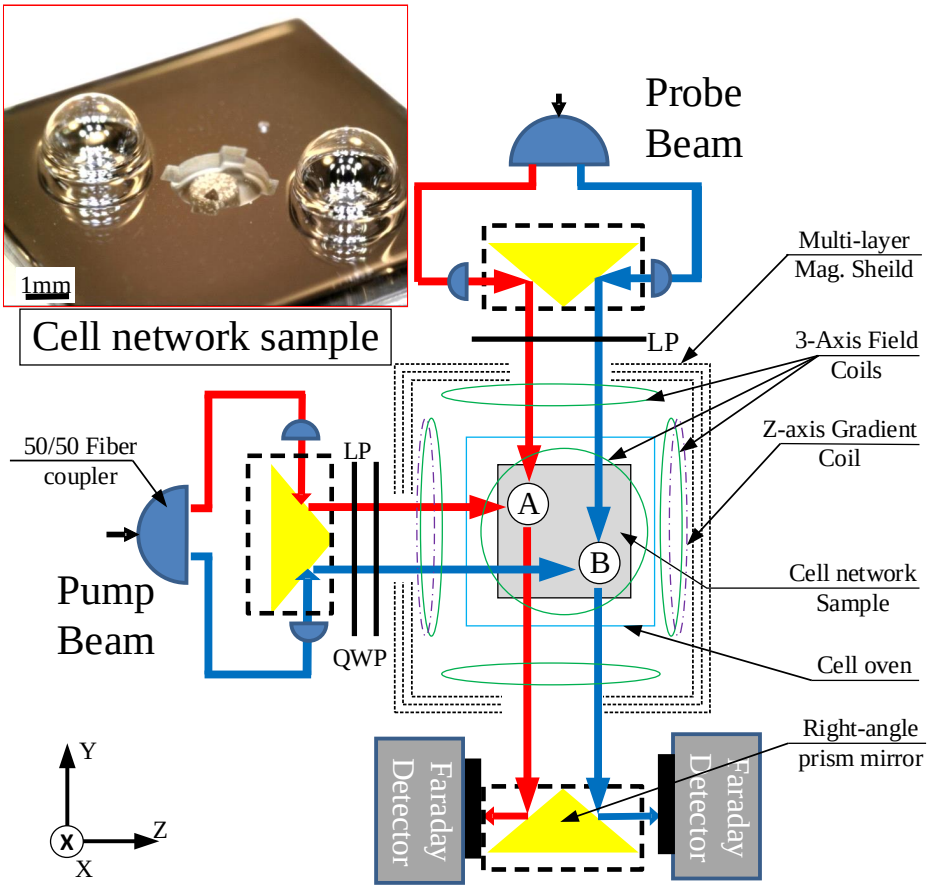

Figure 6.1: Experimental setup for pumping and probing two cells of the same sample simultaneously, insert: a photograph of fabricated prototype which was used in the experiment.

Moreover, using a single source for pumping and a single source for probing in combination with a switching mechanism such as digital light processor (DLP) is an attractive path to explore to shrink the sensor size and increase the number of interrogated cells.

Bibliography

[1] IEEE standard specification format guide and test procedure for coriolis vibratory gyros. *IEEE Std 1431-2004*, pages 1–78, Dec 2004.

[2] H. C. Abbink, E. Kanegsberg, K. D. Marino, and C. H. Volk. Micro-cell for NMR gyroscope, Nov. 6 2007. US Patent 7,292,031.

[3] H. C. Abbink, E. Kanegsberg, and R. A. Patterson. NMR gyroscope. July 3 2007. US Patent 7,239,135.

[4] C. Acar and A. Shkel. *MEMS vibratory gyroscopes: structural approaches to improve robustness*. Springer Science & Business Media, 2008.

[5] J. Allred, R. Lyman, T. Kornack, and M. V. Romalis. High-sensitivity atomic magnetometer unaffected by spin-exchange relaxation. *Physical review letters*, 89(13):130801, 2002.

[6] J. M. Andres. Optically pumped gyromagnetic apparatus, Oct. 26 1965. US Patent 3,214,683.

[7] S. Appelt, A. B.-A. Baranga, C. Erickson, M. Romalis, A. Young, and W. Happer. Theory of spin-exchange optical pumping of 3 he and 129 xe. *Physical Review A*, 58(2):1412, 1998.

[8] M. H. Asadian, Y. Wang, R. M. Noor, and A. M. Shkel. Design space exploration of hemi-toroidal fused quartz shell resonators. In *IEEE International Symposium on Inertial Sensors and Systems (INERTIAL'19)*, Naples, FL USA, April 1-5, 2019.

[9] M. H. Asadian, Y. Wang, and A. M. Shkel. Design and fabrication of 3d fused quartz shell resonators for broad range of frequencies and increased decay time. In *2018 IEEE SENSORS*, pages 1–4, New Delhi, India, October 29-31, 2018.

[10] H. Aschenbrenner. Eine anordnung zur registrierung rascher magnetischer storungen hochfrequenztechnik und elektroakustik. *Band*, 47:177–181, 1936.

[11] M. N. Baibich, J. M. Broto, A. Fert, F. N. Van Dau, F. Petroff, P. Etienne, G. Creuzet, A. Friederich, and J. Chazelas. Giant magnetoresistance of (001) fe/(001) cr magnetic superlattices. *Physical review letters*, 61(21):2472, 1988.

[12] D. Bayley, I. Greenwood, and J. Simpson. Optically pumped nuclear magnetic resonance gyroscope, Dec. 11 1973. US Patent 3,778,700.

[13] R. Beiranvand. Analyzing the uniformity of the generated magnetic field by a practical one-dimensional helmholtz coils system. *Review of Scientific Instruments*, 84(7):075109, 2013.

[14] G. Binasch, P. Grünberg, F. Saurenbach, and W. Zinn. Enhanced magnetoresistance in layered magnetic structures with antiferromagnetic interlayer exchange. *Physical review B*, 39(7):4828, 1989.

[15] F. Bloch. Nuclear induction. *Physical review*, 70(7-8):460, 1946.

[16] M. A. Brown and R. C. Semelka. *MRI.: Basic Principles and Applications*. John Wiley & Sons, 2011.

[17] F. Bucholtz, D. Dagenais, and K. Koo. High-frequency fibre-optic magnetometer with 70 ft/square root (hz) resolution. *Electronics Letters*, 25(25):1719–1721, 1989.

[18] D. Budker, W. Gawlik, D. F. Kimball, S. M. Rochester, V. V. Yashchuk, and A. Weis. Resonant nonlinear magneto-optical effects in atoms. *Rev. Mod. Phys.*, 74:1153–1201, Nov 2002.

[19] D. Budker and M. Romalis. Optical magnetometry. *Nature Physics*, 3(4), 2007.

[20] M. Bulatowicz and M. Larsen. Compact atomic magnetometer for global navigation (nav-cam). In *2012 IEEE/ION Position Location and Navigation Symposium (PLANS)*, pages 1088–1093, Myrtle Beach, SC, USA, 23-26 April, 2012.

[21] M. D. Bulatowicz. Temperature system with magnetic field suppression, Mar. 20 2012. US Patent 8,138,760.

[22] G. Cates, S. Schaefer, and W. Happer. Relaxation of spins due to field inhomogeneities in gaseous samples at low magnetic fields and low pressures. *Physical Review A*, 37(8):2877, 1988.

[23] G. Cates, D. White, T.-R. Chien, S. Schaefer, and W. Happer. Spin relaxation in gases due to inhomogeneous static and oscillating magnetic fields. *Physical Review A*, 38(10):5092, 1988.

[24] J. Clarke and A. I. Braginski. *The SQUID handbook*, volume 1. Wiley Online Library, 2004.

[25] C. Cohen-Tannoudji, J. Dupont-Roc, S. Haroche, and F. Laloë. Detection of the static magnetic field produced by the oriented nuclei of optically pumped he 3 gas. *Physical Review Letters*, 22(15):758, 1969.

[26] C. Cohen-Tannoudji, J. Dupont-Roc, S. Haroche, and F. Laloë. Diverses résonances de croisement de niveaux sur des atomes pompés optiquement en champ nul. i. théorie. *Revue de physique appliquée*, 5(1):95–101, 1970.

[27] A. D. Cronin, J. Schmiedmayer, and D. E. Pritchard. Optics and interferometry with atoms and molecules. *Reviews of Modern Physics*, 81(3):1051, 2009.

[28] H. Dang, A. C. Maloof, and M. V. Romalis. Ultrahigh sensitivity magnetic field and magnetization measurements with an atomic magnetometer. *Applied Physics Letters*, 97(15):151110, 2010.

[29] H. Dehmelt. Modulation of a light beam by precessing absorbing atoms. *Physical Review*, 105(6):1924, 1957.

[30] E. Donley. Nuclear magnetic resonance gyroscopes. In *Proceedings to the IEEE Sensors Conference*, pages 17–22, Waikoloa HI ,USA, November 1-4, 2010.

[31] E. Donley, J. Long, T. Liebisch, E. Hodby, T. Fisher, and J. Kitching. Nuclear quadrupole resonances in compact vapor cells: the crossover between the NMR and the nuclear quadrupole resonance interaction regimes. *Physical Review A*, 79(1):013420, 2009.

[32] A. Douahi, L. Nieradko, J. Beugnot, J. Dziuban, H. Maillote, S. Guerandel, M. Moraja, C. Gorecki, and V. Giordano. Vapour microcell for chip scale atomic frequency standard. *Electronics Letters*, 43(5):33–34, 2007.

[33] E. J. Eklund. *Microgyroscope based on spin-polarized nuclei*. PhD thesis, University of California, Irvine, 2008.

[34] E. J. Eklund and A. M. Shkel. Glass blowing on a wafer level. *IEEE Journal of Microelectromechanical Systems*, 16(2):232–239, 2007.

[35] E. J. Eklund, A. M. Shkel, S. Knappe, E. Donley, and J. Kitching. Glass-blown spherical microcells for chip-scale atomic devices. *Sensors and Actuators A: Physical*, 143(1):175–180, 2008.

[36] E. J. Eklund, A. M. Shkel, S. Knappe, E. Donley, and J. Kitching. Spherical rubidium vapor cells fabricated by micro glass blowing. In *IEEE (MEMS'07), Conference on Micro Electro Mechanical Systems.*, Kobe, Japan, January 21-25, 2007.

[37] J. Fang and J. Qin. Advances in atomic gyroscopes: A view from inertial navigation applications. *Sensors*, 12(5):6331–6346, 2012.

[38] S. M. Felton, M. T. Tolley, B. Shin, C. D. Onal, E. D. Demaine, D. Rus, and R. J. Wood. Self-folding with shape memory composites. *Soft Matter*, 9(32):7688–7694, 2013.

[39] R. P. Feynman, R. B. Leighton, and M. Sands. *The Feynman lectures on physics, Vol. III: The new millennium edition: Quantum Mechanics*, volume 3. Basic books, 2011.

[40] F. Franz and C. Volk. Spin relaxation of rubidium atoms in sudden and quasimolecular collisions with light-noble-gas atoms. *Physical review A*, 14(5):1711, 1976.

[41] J. T. Fraser. Optically pumped magnetic resonance gyroscope and direction sensor, Sept. 10 1963. US Patent 3,103,621.

[42] I. Greenwood and J. Simpson. Fundamental noise limitations in magnetic resonance gyroscopes. In *NAECON'77; Proceedings of the National Aerospace and Electronics Conference*, Dayton, OH USA, May 17-19, 1977.

[43] W. C. Griffith, S. Knappe, and J. Kitching. Femtotesla atomic magnetometry in a microfabricated vapor cell. *Optics express*, 18(26):27167–27172, 2010.

[44] B. Grover. Noble-gas nmr detection through noble-gas-rubidium hyperfine contact interaction. *Physical Review Letters*, 40(6):391, 1978.

[45] B. C. Grover, E. Kanegsberg, J. G. Mark, and R. L. Meyer. Nuclear magnetic resonance gyro, June 5 1979. US Patent 4,157,495.

[46] V. M. Gundeti. Folded MEMS approach to NMRG. Master's thesis, University of California, Irvine, 2015.

[47] E. L. Hahn. Free nuclear induction. *Physics Today*, 6(11):4–9, 1953.

[48] W. Happer. Optical pumping. *Reviews of Modern Physics*, 44(2):169, 1972.

[49] W. Happer, E. Miron, S. Schaefer, D. Schreiber, W. A. van Wijngaarden, and X. Zeng. Polarization of the nuclear spins of noble-gas atoms by spin exchange with optically pumped alkali-metal atoms. *Phys. Rev. A*, 29:3092–3110, Jun 1984.

[50] M. Hasegawa, R. Chutani, C. Gorecki, R. Boudot, P. Dziuban, V. Giordano, S. Clatot, and L. Mauri. Microfabrication of cesium vapor cells with buffer gas for MEMS atomic clocks. *Sensors and Actuators A: Physical*, 167(2):594–601, 2011.

[51] W. Heil, H. Humblot, E. Otten, M. Schafer, R. Sarkau, and M. Leduc. Very long nuclear relaxation times of spin polarized helium 3 in metal coated cells. *Physics Letters A*, 201(4):337–343, 1995.

[52] Y. Hui, T. Nan, N. X. Sun, and M. Rinaldi. High resolution magnetometer based on a high frequency magnetoelectric mems-cmos oscillator. *IEEE Journal of Microelectromechanical Systems*, 24(1):134–143, 2014.

[53] R. Jiménez-Martínez and S. Knappe. Microfabricated optically-pumped magnetometers. In *High Sensitivity Magnetometers*, pages 523–551. Springer, 2017.

[54] J. T. Kajiya. The rendering equation. In *ACM SIGGRAPH computer graphics*, volume 20, pages 143–150. ACM, 1986.

[55] M. Kasevich and S. Chu. Atomic interferometry using stimulated raman transitions. *Physical review letters*, 67(2):181, 1991.

[56] J. Kitching. Chip-scale atomic devices. *Applied Physics Reviews*, 5(3):031302, 2018.

[57] J. Kitching, E. A. Donley, E. Hodby, A. Shkel, and E. J. Eklund. Compact atomic magnetometer and gyroscope based on a diverging laser beam. Jan. 18 2011. US Patent 7,872,473.

[58] J. Kitching, S. Knappe, and E. A. Donley. Atomic sensors–a review. *IEEE Sensors Journal*, 11(9):1749–1758, 2011.

[59] P. Knapkiewicz. Technological assessment of mems alkali vapor cells for atomic references. *Micromachines*, 10(1):25, 2019.

[60] S. Knappe, O. Alem, D. Sheng, and J. Kitching. Microfabricated optically-pumped magnetometers for biomagnetic applications. In *Journal of Physics: Conference Series*, volume 723, page 012055. IOP Publishing, 2016.

[61] S. Knappe, V. Shah, P. D. Schwindt, L. Hollberg, J. Kitching, L.-A. Liew, and J. Moreland. A microfabricated atomic clock. *Applied Physics Letters*, 85(9):1460–1462, 2004.

[62] S. A. Knappe. Emerging topics: MEMS atomic clocks. *Comprehensive Microsystems*, 3, 2007.

[63] I. Kominis, T. Kornack, J. Allred, and M. Romalls. A subfemtotesla multichannel atomic magnetometer. *Nature*, 422(6932):596, 2003.

[64] T. Kornack, R. Ghosh, and M. Romalis. Nuclear spin gyroscope based on an atomic comagnetometer. *Physical review letters*, 95(23):230801, 2005.

[65] H. Korth, K. Strohbehn, F. Tejada, A. G. Andreou, J. Kitching, S. Knappe, S. J. Lehtonen, S. M. London, and M. Kafel. Miniature atomic scalar magnetometer for space based on the rubidium isotope 87Rb. *Journal of Geophysical Research: Space Physics*, 121(8):7870–7880, 2016.

[66] M. Kwakernaak, S. Lipp, S. McBride, P. Zanzucchi, W. Chan, V. Khalfin, H. An, R. Whaley Jr, B. Willner, and A. Ulmer. Components for batch-fabricated chip-scale atomic clocks. Technical report, Sarnoff Corp, Princeton NJ, 2004.

[67] T. M. Kwon and W. P. Debley. Magnetic resonance cell and method for its fabrication, May 22 1984. US Patent 4,450,407.

[68] T. M. Kwon and W. P. Debley. Magnetic resonance cell and method for its fabrication, May 22 1984. US Patent 4,450,407.

[69] L. Lam, E. Phillips, E. Kanegsberg, and G. Kamin. Application of cw single-mode gaalas lasers to Rb-Xe NMR gyroscopes. 412:272–277, 1983.

[70] M. Larsen and M. Bulatowicz. Nuclear magnetic resonance gyroscope: For darpa's micro-technology for positioning, navigation and timing program. In *IEEE International Symposium on Inertial Sensors and Systems (ISISS'14)*, Laguna Beach, CA USA, February 25-26, 2014.

[71] J. Lenz and S. Edelstein. Magnetic sensors and their applications. *IEEE Sensors journal*, 6(3):631–649, 2006.

[72] J. Li, W. Quan, B. Han, F. Liu, L. Xing, and G. Liu. Multilayer cylindrical magnetic shield for serf atomic co-magnetometer application. *IEEE Sensors Journal*, 19(8):2916–2923, 2018.

[73] J. Li, W. Quan, B. Zhou, Z. Wang, J. Lu, Z. Hu, G. Liu, and J. Fang. Serf atomic magnetometer–recent advances and applications: A review. *IEEE Sensors Journal*, 18(20):8198–8207, 2018.

[74] Y. W. Lin, A. Efimovskaya, and A. M. Shkel. Study of environmental survivability and stability of folded MEMS IMU. In *IEEE International Symposium on Inertial Sensors and Systems (INERTIAL'17)*, pages 132–135, Kauai, HI USA, March 28-31, 2017.

[75] P. A. Lindahl, S. R. Shaw, and S. B. Leeb. Fuel cell stack emulation for cell and hardware-in-the-loop testing. *IEEE Transactions on Instrumentation and Measurement*, 67(9):2143–2152, Sep. 2018.

[76] X. Liu, C. Chen, T. Qu, K. Yang, and H. Luo. Transverse spin relaxation and diffusion-constant measurements of spin-polarized 129 xe nuclei in the presence of a magnetic field gradient. *Scientific reports*, 6:24122, 2016.

[77] Y. Liu, J. K. Boyles, J. Genzer, and M. D. Dickey. Self-folding of polymer sheets using local light absorption. *Soft Matter*, 8(6):1764–1769, 2012.

[78] C.-C. Lu, J. Huang, P.-K. Chiu, S.-L. Chiu, and J.-T. Jeng. High-sensitivity low-noise miniature fluxgate magnetometers using a flip chip conceptual design. *Sensors*, 14(8):13815–13829, 2014.

[79] L. M. Lust and D. W. Youngner. Chip scale atomic gyroscope, Apr. 15 2008. US Patent 7,359,059.

[80] R. Lutwak, J. Deng, W. Riley, M. Varghese, J. Leblanc, G. Tepolt, M. Mescher, D. Serkland, K. Geib, and G. Peake. The chip-scale atomic clock-low-power physics package. Technical report, Symmetricom-Technology Realization Center, Beverly MA, 2004.

[81] Z. Ma, E. Sorte, and B. Saam. Collisional he 3 and xe 129 frequency shifts in rb–noble-gas mixtures. *Physical review letters*, 106(19):193005, 2011.

[82] C. P. Martendal and A. P. N. de Oliveira. Glass viscosity at crystallization temperature: an approach. *Journal of Thermal Analysis and Calorimetry*, 130(3):1903–1912, Dec 2017.

[83] D. Meyer and M. Larsen. Nuclear magnetic resonance gyro for inertial navigation. *Gyroscopy and Navigation*, 5(2):75–82, 2014.

[84] R. Mhaskar, S. Knappe, and J. Kitching. A low-power, high-sensitivity micromachined optical magnetometer. *Applied Physics Letters*, 101(24):241105, 2012.

[85] R. Michalzik. *VCSELs: A Research Review*, pages 3–18. Springer Berlin Heidelberg, Berlin, Heidelberg, 2013.

[86] P. Minotti, L. G. Pagani, N. Aresi, and G. Langfelder. Mems emulator: A tool for development and testing of electronics for microelectromechanical systems. *IEEE Journal of Microelectromechanical Systems*, 27(2):321–332, 2018.

[87] J. J. Mirijanian. Techniques to characterize vapor cell performance for a nuclear-magnetic-resonance gyroscope. Master's thesis, 2012.

[88] R. Mohr, K. Kratz, T. Weigel, M. Lucka-Gabor, M. Moneke, and A. Lendlein. Initiation of shape-memory effect by inductive heating of magnetic nanoparticles in thermoplastic polymers. *Proceedings of the National Academy of Sciences*, 103(10):3540–3545, 2006.

[89] L. Nieradko, C. Gorecki, A. Douahi, V. Giordano, J. C. Beugnot, J. Dziuban, and M. Moraja. New approach of fabrication and dispensing of micromachined cesium vapor cell. *Journal of Micro/Nanolithography, MEMS, and MOEMS*, 7(3):033013–033013, 2008.

[90] R. M. Noor, M. H. Asadian, and A. M. Shkel. Design considerations for micro-glassblown atomic vapor cells. *IEEE Journal of Microelectromechanical Systems*, 2019. Manuscript submitted for publication.

[91] R. M. Noor, V. Gundeti, and A. M. Shkel. A status on components development for folded micro NMR gyro. In *IEEE International Symposium on Inertial Sensors and Systems (INERTIAL'17)*, Kauai, HI USA, March 28-31, 2017.

[92] R. M. Noor, V. M. Gundeti, and A. M. Shkel. Reconfigurable analog emulator: a tool for development of NMR atomic sensors. *IEEE Sensors Journal*, 2019. Manuscript submitted for publication.

[93] R. M. Noor, N. Kulachenkov, M. H. Asadian, and A. M. Shkel. Study on MEMS glass-blown cells for NMR sensors. In *IEEE International Symposium on Inertial Sensors and Systems (INERTIAL'19)*, Naples, FL USA, April 1-5, 2019.

[94] R. M. Noor and A. M. Shkel. MEMS components for NMR atomic sensors. *IEEE Journal of Microelectromechanical Systems*, 27(6):1148–1159, 2018.

[95] J. J. Olivero and R. Longbothum. Empirical fits to the voigt line width: A brief review. *Journal of Quantitative Spectroscopy and Radiative Transfer*, 17(2):233–236, 1977.

[96] R. Osiander, S. Ecelberger, R. Givens, D. Wickenden, J. Murphy, and T. Kistenmacher. A microelectromechanical-based magnetostrictive magnetometer. *Applied physics letters*, 69(19):2930–2931, 1996.

[97] K. Padmaraju. Faraday rotation. *American Journal of Physics*, 67:8, 1999.

[98] S. Parkash and P. Vijendran. Sorption of active gases by non-evaporable getter. *Vacuum*, 33(5):295–299, 1983.

[99] M. A. Perez, J. Kitching, and A. M. Shkel. Design and demonstration of PECVD multilayer dielectric mirrors optimized for micromachined cavity angled sidewalls. *Sensors and Actuators A: Physical*, 155(1):23–32, 2009.

[100] M. A. Perez, U. Nguyen, S. Knappe, E. A. Donley, J. Kitching, and A. M. Shkel. Rubidium vapor cell with integrated bragg reflectors for compact atomic MEMS. *Sensors and Actuators A: Physical*, 154(2):295–303, 2009.

[101] Y. Pétremand, C. Affolderbach, R. Straessle, M. Pellaton, D. Briand, G. Mileti, and N. F. de Rooij. Microfabricated rubidium vapour cell with a thick glass core for small-scale atomic clock applications. *Journal of Micromechanics and Microengineering*, 22(2):025013, 2012.

[102] G. A. Pitz, A. J. Sandoval, T. B. Tafoya, W. L. Klennert, and D. A. Hostutler. Pressure broadening and shift of the rubidium d1 transition and potassium d2 transitions by various gases with comparison to other alkali rates. *Journal of Quantitative Spectroscopy and Radiative Transfer*, 140:18–29, 2014.

[103] E. Ramsden. *Hall-effect sensors: theory and application*. Elsevier, 2011.

[104] R. Rieger and J.-Y. Chen. An axon emulator for evaluation of nerve recording systems. In *2012 IEEE International Symposium on Circuits and Systems*, pages 1528–1531. IEEE, 2012.

[105] F. Riehle, T. Kisters, A. Witte, J. Helmcke, and C. J. Bordé. Optical ramsey spectroscopy in a rotating frame: Sagnac effect in a matter-wave interferometer. *Physical review letters*, 67(2):177, 1991.

[106] R. Robbins. SCS Parylene Deposition standard operating procedure. `https://research.utdallas.edu/cleanroom/manuals/scs-parylene-deposition`. Accessed: 2016-12-07.

[107] M. D. Rotondaro and G. P. Perram. Collisional broadening and shift of the rubidium d1 and d2 lines (52s12, 52p12, 52p32) by rare gases, h2, d2, n2, ch4 and cf4. *Journal of Quantitative Spectroscopy and Radiative Transfer*, 57(4):497–507, 1997.

[108] SAES Group. *St 101 Non-evaporable Getters*, 2007. Available online.

[109] I. Savukov and M. Romalis. NMR detection with an atomic magnetometer. *Physical review letters*, 94(12):123001, 2005.

[110] I. M. Savukov. *Spin Exchange Relaxation Free (SERF) Magnetometers*, pages 451–491. Springer International Publishing, Cham, 2017.

[111] S. Schaefer, G. Cates, T.-R. Chien, D. Gonatas, W. Happer, and T. Walker. Frequency shifts of the magnetic-resonance spectrum of mixtures of nuclear spin-polarized noble gases and vapors of spin-polarized alkali-metal atoms. *Physical Review A*, 39(11):5613, 1989.

[112] D. K. Serkland, K. M. Geib, G. M. Peake, R. Lutwak, A. Rashed, M. Varghese, G. Tepolt, and M. Prouty. Vcsels for atomic sensors. Technical report, Sandia National Laboratories (SNL-NM), Albuquerque, NM (United States), 2007.

[113] D. Sheng, A. R. Perry, S. P. Krzyzewski, S. Geller, J. Kitching, and S. Knappe. A microfabricated optically-pumped magnetic gradiometer. *Applied physics letters*, 110(3):031106, 2017.

[114] A. M. Shkel. The chip-scale combinatorial atomic navigator. *GPS World*, 24(8):8–10, 2013.

[115] J. Simpson, J. Fraser, and I. Greenwood. An optically pumped nuclear magnetic resonance gyroscope. *IEEE Transactions on Aerospace*, 1(2):1107–1110, 1963.

[116] D. A. Steck. Rubidium 87 d line data, 2001. available online at http://steck.us/alkalidata (revision 2.1.5, 13 January 2015).

[117] N. J. Stone. Table of nuclear magnetic dipole and electric quadrupole moments. *Atomic Data and Nuclear Data Tables*, 90(1):75–176, 2005.

[118] I. Sulai, Z. DeLand, M. Bulatowicz, C. Wahl, R. Wakai, and T. Walker. Characterizing atomic magnetic gradiometers for fetal magnetocardiography. *arXiv preprint arXiv:1906.03227*, 2019.

[119] J. Taylor, P. Cappellaro, L. Childress, L. Jiang, D. Budker, P. Hemmer, A. Yacoby, R. Walsworth, and M. Lukin. High-sensitivity diamond magnetometer with nanoscale resolution. *Nature Physics*, 4(10):810, 2008.

[120] J. Vanier and C. Audoin. *The quantum physics of atomic frequency standards*, volume 2. CRC Press, 1989.

[121] C. H. Volk, T. M. Kwon, and J. G. Mark. Measurement of the ^{87}Rb-^{129}Xe spin-exchange cross section. *Phys. Rev. A*, 21:1549–1555, May 1980.

[122] H. Wadell. Volume, shape, and roundness of quartz particles. *The Journal of Geology*, 43(3):250–280, 1935.

[123] T. G. Walker. Estimates of spin-exchange parameters for alkali-metal–noble-gas pairs. *Phys. Rev. A*, 40:4959–4964, Nov 1989.

[124] T. G. Walker and W. Happer. Spin-exchange optical pumping of noble-gas nuclei. *Reviews of Modern Physics*, 69(2):629, 1997.

[125] T. G. Walker and M. S. Larsen. Chapter eight-spin-exchange-pumped NMR gyros. *Advances In Atomic, Molecular, and Optical Physics*, 65:373–401, 2016.

[126] J. Wang, B. Zhou, W. Wu, L. Chen, and J. Fang. Uniform field coil design based on the target-field method in miniature atomic sensors. *IEEE Sensors Journal*, 19(8):2895–2901, 2018.

[127] G. Wertheim, M. Butler, K. West, and D. Buchanan. Determination of the gaussian and lorentzian content of experimental line shapes. *Review of Scientific Instruments*, 45(11):1369–1371, 1974.

[128] S. Woetzel, F. Talkenberg, T. Scholtes, R. IJsselsteijn, V. Schultze, and H.-G. Meyer. Lifetime improvement of micro-fabricated alkali vapor cells by atomic layer deposited wall coatings. *Surface and Coatings Technology*, 221:158–162, 2013.

[129] A. M. Worthington. *Dynamics of rotation: an elementary introduction to rigid dynamics*. Longmans, Green, and Company, 1910.

[130] Z. Wu, W. Happer, M. Kitano, and J. Daniels. Experimental studies of wall interactions of adsorbed spin-polarized xe 131 nuclei. *Physical Review A*, 42(5):2774, 1990.

[131] Z. You. Chapter 9 - magnetometer technology. In *Space Microsystems and Micro/nano Satellites*, Micro and Nano Technologies, pages 341 – 360. Butterworth-Heinemann, 2018.

[132] X. Zeng, E. Miron, W. Van Wijngaarden, D. Schreiber, and W. Happer. Wall relaxation of spin polarized 129xe nuclei. *Physics Letters A*, 96(4):191–194, 1983.

[133] C. Zhang, A. Cocking, E. Freeman, Z. Liu, and S. Tadigadapa. On-chip glass microspherical shell whispering gallery mode resonators. *Scientific reports*, 7(1):14965, 2017.

[134] S. A. Zotov, M. C. Rivers, A. A. Trusov, and A. M. Shkel. Chip-scale IMU using folded-MEMS approach. In *IEEE Sensors Conference, 2010*, Waikoloa, HI USA, November 1-4, 2010.

[135] S. Zou, H. Zhang, X. Chen, Z. Wang, W. Quan, and J.-c. Fang. Ultra-sensitive atomic magnetometers for studying spin precessions of hyperpolarized noble gases based on system identification. *IEEE Sensors Journal*, 18(24):9931–9939, 2018.

Appendix A

Custom Filling Station

The previously described process for filling cells with alkali metal and buffer gas in Chapter 4 requires certain conditions for the final anodic bonding. After the cell network is opened from the backside and the pill is inserted, the network needs to be filled with buffer gasses and then sealed. For this purpose, a special chamber was designed with the capability of generating a vacuum level of 10^{-6} Torr, included multiple ports for injecting gasses, and combined with anodic bonding which is capable of sealing cells with injected gases. To be able to perform the anodic bonding, the chamber was equipped with a heater that can heat the samples up to 400°C, electrical connections and electrodes to apply 600V, and a loading mechanism that is capable of applying a 10N force during the anodic bonding process.

Since these options were not commercially available, we built the custom chamber in the MicroSystems Lab at UCI. A specially designed chamber with a special heater for that purpose was designed and built, see Figure A.1 and Figure A.2 for the chamber and the heater drawings. The bill of material is shown next.

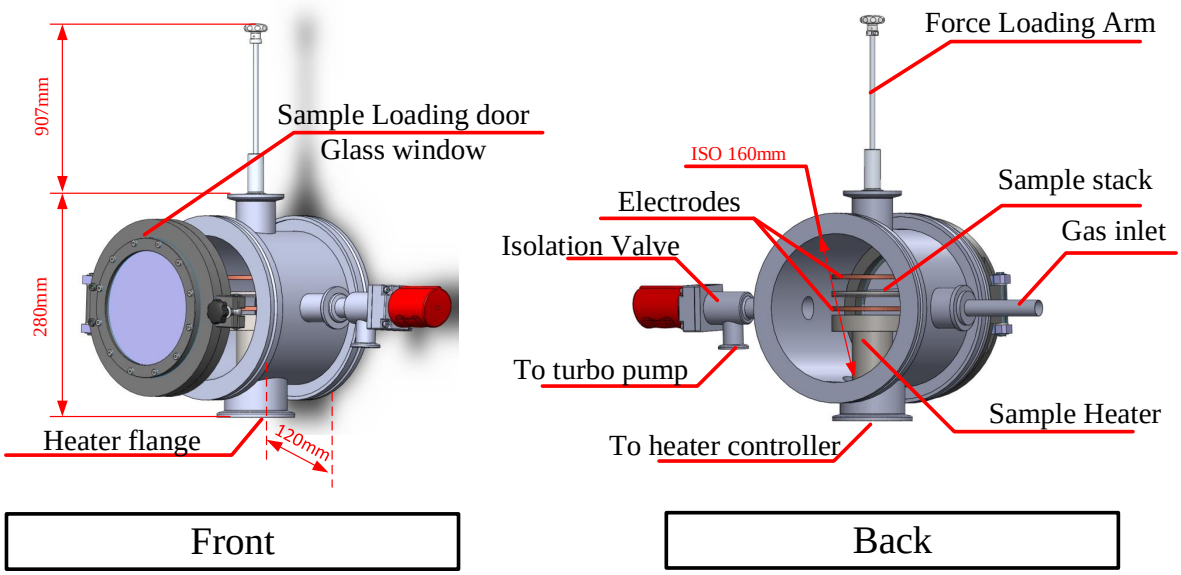

Figure A.1: Illustration showing the front and back sides of the filling station chamber.

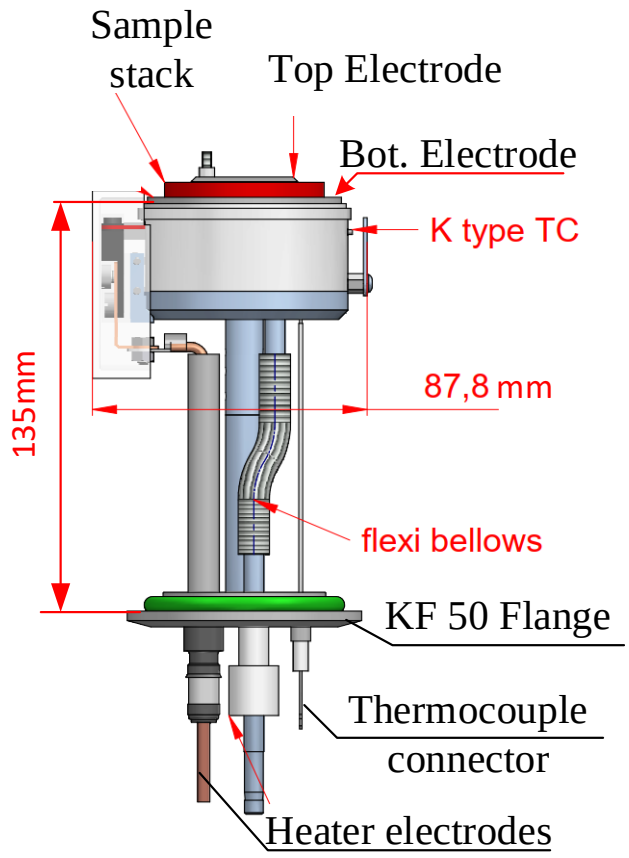

Figure A.2: Illustration showing the sample heater mounted on a KF 50 Flange

Table A.1: Bill of material for the filling station from two vendors Ceramisis Ltd. and Pfeiffer Vacuum Inc.

Quantity	Description	Catalog #	Unit Price
	Ceramisis Ltd		
1	2" Vacuum heater 1000C version of the heater (HTWM6-CCC-02) in Figure A.2	HTWM6-CCC-02	$12,862.66
	Pfeiffer Vacuum Inc		
1	Vacuum pump, HiCube 80 Eco DN 40 ISO-KF, Figure B.4	PM 015 888 -T	$4,995.00
1	CUSTOMIZED Vacuum chamber (DN 160 ISO-K cross), Figure A.1	320R1ZS160	$1,180.00
1	Quick-Access-Door, with Viewport, DN 160 ISO-F Stainless steel, Figures A.1 and B.4	520KTU160-G	$2,032.68
1	Rotary/Linear Feedthrough, DN 40 ISO-KF Elastomer -sealed stroke 250 mm, Figures A.1 and B.4	120MDD040-0250	$1,017.00
1	CUSTOMIZED Blank Flange, DN 20 ISO-K Stainless Steel 304/1.4301, Figure B.5	320FBL160	$670.00
1	Rotatable Bolt Ring, DN 160 ISO-K Stainless Steel 304/1.4301 circlip included	320FLU160	$197.00
1	Angle valve DN 40 ISO-KF manually operated	PF A51 033	$389.27
1	Angle valve DN 16 ISO-KF manually operated	PF A31 033	$276.04
1	DualGauge Display and control unit for two gauges 100-250 V AC, 50/60 Hz	PT G28 290'	$1,334.80
1	PKR 361, Active Pirani/ Cold cathode gauge DN 25 ISO-KF high current	PT T03 140 010	$1,060.20
1	Active Pirani/Capacitance Transmitter DN 16 ISO-KF, 80C	PT R26 855	$488.48
1	Supporting adapters and valves		$1,053.85

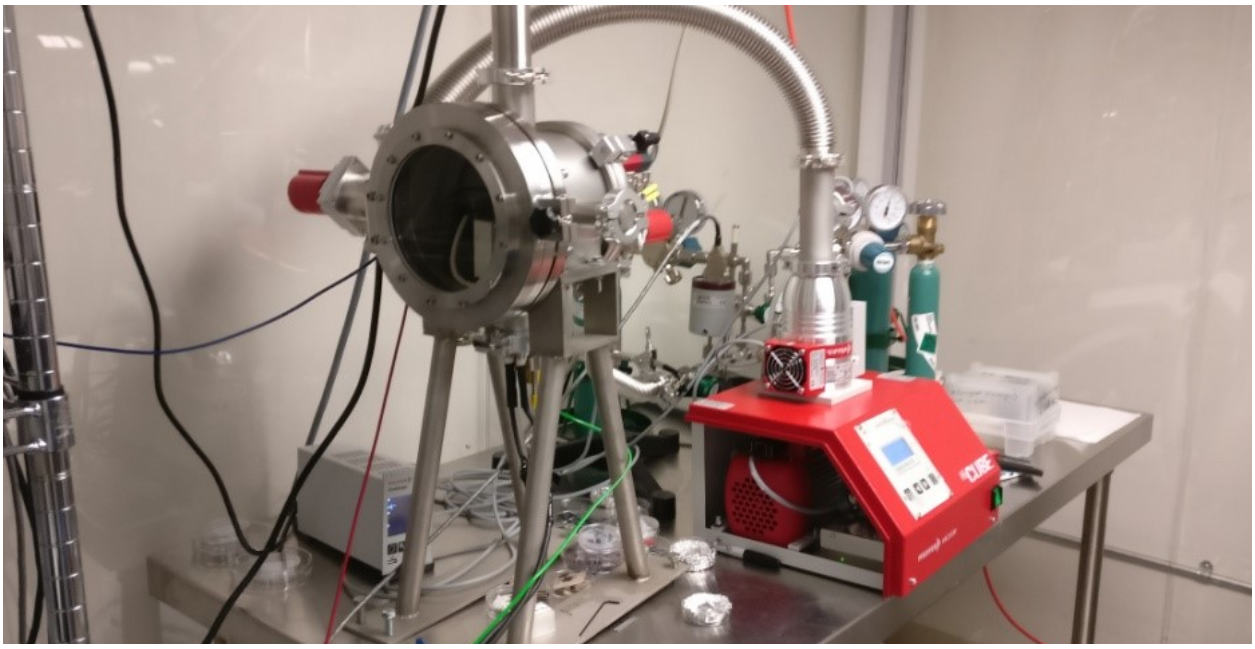

Figure A.3: Picture of the Filling Station at EG2119

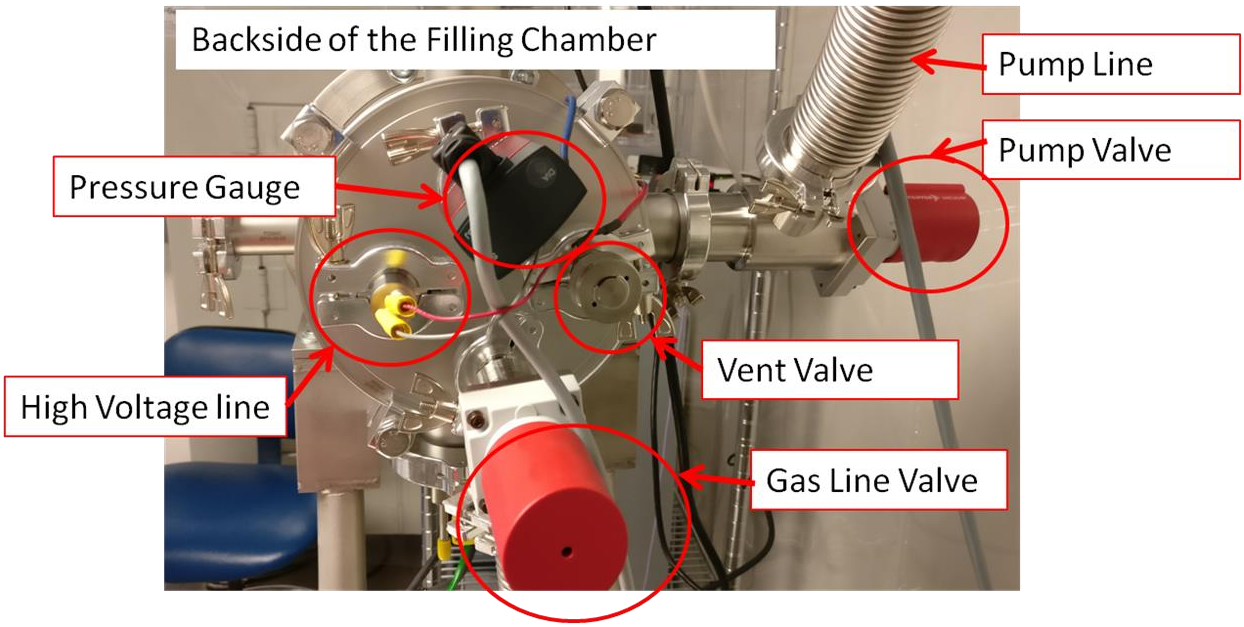

Figure A.4: Backside of the filling chamber showing pump, gas and venting valves, pressure gauge, high voltage and pump line.

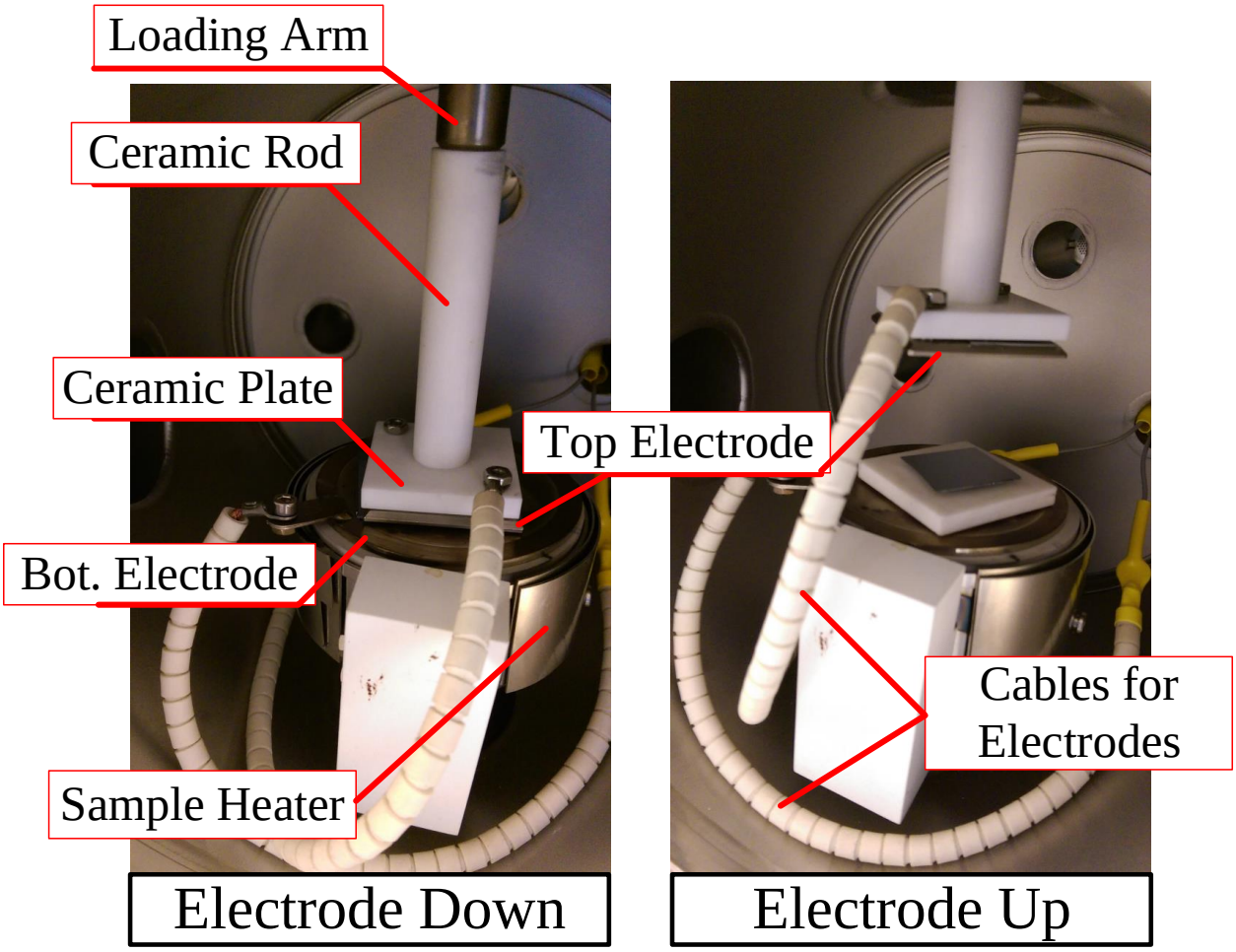

Figure A.5: Pictures from inside the filling chamber showing electrodes, loading arm, cables with ceramic beads, and additional ceramic parts that connects the top electrode to the loading arm. The picture on the left shows when the top electrodes is lowered and the force is applied and the picture on the right shows the top electrode in the up position.

Appendix B

Fabrication Recipes

B.1 Micro Resistive Heaters

In this Appendix the detailed recipes of the fabrication processes. For the fabrication of the micro resistive heaters, we are starting with 4" Si substrates with $1\mu m$ thermally grown oxide or a 4" glass wafer.

B.1.1 Metal 1: Electroplated Nickle

- Dehydrate wafers in the oven at 120°C for 60 minutes.
- Evaporate 250Åof Ti and 1500Åof Au on your substrate using Ebeam1 evaporator at INRF (Ask Mo or Richard for help).
- Cover the tom of the wafer with a small piece of blue tape (this where the clamp will be attached for electroplating)
- Spin coat wafers with AZ4620 PR at (500 for 10 seconds then 1500 for 30 seconds).

- bake in the oven 95°C for 30 minutes.
- Expose wafer using MA-6 mask aligner (10mW, g-line lamp) for 90 seconds (soft contact, 50um gap).
- Develop in 1:4 solution of AZ400K(Developer): H_2O, for about 150 seconds-180 seconds (carefully check your wafer for PR residues under the microscope).
- Remove the blue tape piece to expose the metal seed layer.
- Place a blue low tack dicing tape on the back (if it was Si wafer) to prevent Ni from depositing on the back of your wafer.
- Prepare the nickle electroplating process setup (talk to INRF staff about setup).
- When the setup is ready, place your wafer with wafer flat parallel to the bottom of the beaker, run the current source at 15mA for 10 minutes. (the electroplating time is highly dependent on the pattern, and if there were any uncovered parts with PR it would take longer) after 10 minutes check in Daktak for Ni desired thickness.
- After achieving the desired Ni thickness, remove the PR using AZ400K remover while heating it up to 50-80°C on the hot plate.
- Use Idoide-FREE gold etchant (GE-8110 from Transene Company, Inc.) to etch seed layer (40 seconds), use 2% HF to etch Ti adhesion layer (20-40 seconds dip).

B.1.2 Insulator Layer: SU-8

For the sake of testing the heater, SU-8 was used as an insulator layer. Polyimide or Parylene-c can be used as well. But will need to refer to their recipes.

- Spin coat SU-8 5 on your wafer at 2000rpm with 300rpm/s acceleration to achieve 7um film. (if the Ni was too thick $\geq 10\mu m$ it might be difficult to coat it with uniform film)

- Soft bake at 65°C for 2 minutes, then increase temp. to 95°C and bake for 5 minutes.
- Expose in MA-6 mask aligner for 20 seconds, then bake at 65°C then 95°C for 1 minute each.
- Develop in the SU-8 developer for 1 minute, check for undeveloped regions. (DO NOT use water, only use IPA to rinse the developer)
- bake on the hot plate at 150°C for 60 minutes (to make it hard and can withstand the heater temperature).

B.1.3 Metal 2: Sputtered Cu

Metal 2 was chosen to be sputtered Cu, sputtering gives a better coverage of steps and allows connection between metal 1 and metal 2 through the insulating material.

- Sputter Cr/Cu (250Å/10000Å), (DO NOT perform SPUTTER ETCHING as it might degrade the insulator layer and cause Cr to be irremovable).
- Spin coat AZ 4620 PR on the wafer (2000rpm 425rmp/s acceleration for 40 seconds) then bake at 90°C for 30 minutes.
- Expose in MA-6 mask aligner (CH2) for 90 seconds using Metal2 mask. Develop in 1:4 solution of AZ400K(Developer): H_2O for 2-3 minutes. (check every 60 seconds)
- Use Cu etchant (PCB copper etchant) to etch Cu (40-60 seconds), use chrome etchant 1020 from Transene Company, Inc. for 40 seconds to etch Cr adhesion layer.
- Dicing.

B.2 Folded Micro Helmholtz Coils

All wafers in this run were $500\mu m$ DSP Si+ (400nm) LPCVD SiN, from University Wafers.

B.2.1 Metal 1: electroplated Nickle

Metal 1 is the same process recipe as for the heater in B.1.1.

B.2.2 Insulator layer: Parylene

Parylene needs adhesion promoter to improve the parylene adhesion to the substrate.

- Mix 200ml water with 200ml IPA and 2ml A-174 silane adhesion promoter, and let it sit for two hours.
- Soak wafers in the solution for 30 minutes, take wafer out without blowing or rinsing and put it on a clean-room wipe and let it sit for 30 minutes to dry.
- Soak in IPA for 20 seconds, then dehydrate on the hotplate at 110°C for 120 seconds.
- Place a blue low tack tape on the backside of the wafer to prevent parylene from depositing on the backside.
- Load wafers on the wafer holder and put it in the parylene machine.
- Make a foil boat and measure 30 grams of parylene dimer, and load it in the vaporizer chamber in the parylene machine.
- Run the parylene machine following the standard operating procedures.

- Deposit 1500Åof Ti using Ebeam1 metal evaporator as a hard mask to etch parylene.
- Spin 2000 RPM AZ4620 PR, bake in the 90°C oven for 20 minutes or less. NOTE: NEVER let the wafer in the oven for more 20 minutes, this causes cracks in the parylene.
- Expose using parylene mask in the MA-6 mask aligner.
- After developing, dip wafers in 2% HF for 40 seconds, to etch Ti, remove PR using Acetone.
- Load wafer in Tion RIE machine, using O2CLEAN recipe with the parameters (250mT gas pressure, 150W RF power) etch for 10 minutes intervals for about 50-60 minutes.
- Dip wafer in 2% HF for 60 seconds to remove Ti hard mask and the residues deposited in the RIE machine.

B.2.3 Metal 2

The metal 2 step is similar to the metal 2 step in the heater recipe in B.1.3. The only difference is that we evaporate 250Åof Cr to protect the parylene from the high energy sputtered Cr atoms. Then we did Cr/Cu sputtering.

B.2.4 Backside Etch Though

The last step is to etch through the wafer to release the coil samples.

- Spin AZ4620 on the front-side of the wafer at 2000 rpm and bake at 90°C for 15 minutes.
- Spin AZ4620 on the backside of the wafer at 2000 rpm, bake at 90°C for 30 minutes. Expose using backside etch-through mask, then develop in AZ400K: H_2O solution.

- Place a blue low tack tape on the front-side of the wafer to protect parylene and other features.
- Attach wafer to a handle Si wafer using small double-sided Kapton tape.
- Load wafer in STS, etch using PROCESSB for 100 minutes in 20 minutes intervals to protect the photo-resist.
- After etching is done, soak in Acetone to remove coil samples from the blue tape.
- Clean using Acetone and IPA (don't soak in Acetone for too long, as Acetone cause parylene to swill which might damage the Cu traces.

B.3 Cell Network

This are detailed steps of the fabrication process shown in Figure 4.11. It requires three masks, front side (Si Cavities), backside (Backside), and through holes (Through Holes).

B.3.1 Top-side Si-Cavities and Through Holes

- Starting with new wafer, RCA Clean the wafer, dehydrate on 120°C hotplate for 2 minutes. *If the wafer was used before, you need to perform O_2 clean for at least 10 minutes.*
- Spin coat wafer with AZ4620 PR at (500 for 10 seconds then 1500 for 40 seconds), bake 10 minutes in 90°C oven.
- Spin coat another layer of AZ4620 PR at (500 for 10 seconds then 1500 for 40 seconds), bake 30 minutes in 90°C oven, Be careful to spread the PR nicely by choosing low acceleration in the first step.
- Expose in mask aligner (10mW, g-line lamp) for 180 seconds using mask 1 (Si Cavities).
- Expose the same PR in mask aligner again (10mW, g-line lamp) for 180 seconds using mask 3 (Through Holes).
- Develop in 1:2 AZ400k developer: DI-water, for around 2-3 minutes (stir and pay attention not to overdevelop the wafer).
- Hard bake the wafer in 120°C oven for 15 minutes.
- Apply Blue tape to the back of the wafer and make sure there are no trapped air bubbles (this will help protect the backside for better bonding surface).

- Spin coat a single side polished handle wafer with AZ4620 PR at (500 for 10 seconds then 3000 for 40 seconds)
- Place the wafer on top of the handle wafer while it is on the spinner and press gently on the edges only. Remove the stack from the spinner and bake for 20 minutes in 90°C oven.
- Etch in STS DRIE system using PROCESSB for multiple segments of 30 minutes each. Stop the etching for 5 minutes in between the segments.
- Check the etch depth using Daktak to confirm that the required depth is achieved.
- Use a thin blade to separate the wafers, DO NOT use excessive force, it might break the wafer.
- Place the wafer on top of wipe and slowly remove the blue tape, do not use ACETONE.
- Use AZ400T photo-resist remover to remove the photo-resist. It is recommended to heat up the solution to 70-80 °C.
- After removing the bulk of the photo-resist in AZ400T. Rinse the sample with DI water, blow-dry it with N_2.
- Use oxygen plasma to clean both sides of the wafer. Example of oxygen plasma cleaning: 20 minutes with 200Watt and 150 mTorr of process gas and 50cc Oxygen flow in PlasmaTherm.

This ends the part of etching Si Cavities. By now the wafer is etched $750\mu m$ from the top-side using both the Si Cavities and the through-holes masks. Next, we will complete etching through the wafer using "Through Holes" mask and pre-etch the backside using the (Backside) Mask. Pre-etching the channel makes it easier to perform photo-lithography on die level after the wafer has been diced and the alignment marks are no longer usable. It

also shortens the time required to open the backside of the cells after glassblowing.

B.3.2 Pre-etching backside channels and Through Holes

- Apply Blue tape to the top-side (etched Si Cavities) of the wafer and make sure there are no trapped air bubbles (this step is necessary to be able to load the wafer on the spinner since the blue tape is translucent it will allow us to perform wafer alignment without troubles).
- Spin coat the back of the wafer with AZ4620 PR at (500 for 10 seconds then 1500 for 40 seconds), bake 30 minutes in 90°C oven.
- Expose in mask aligner (10mW, g-line lamp) for 90 seconds using mask 3 (Through Holes).
- Develop in 1 part AZ400k developer to 2 parts DI-water, for around 1-2 minutes (stir and pay attention not to overdevelop the wafer).
- Spin coat a single side polished handle wafer with AZ4620 PR at (500 for 10 seconds then 3000 for 40 seconds)
- Place the wafer on top of the handle wafer while it is on the spinner and press gently. Remove the stack from the spinner and bake for 20 minutes in 90°C oven.
- Etch in STS DRIE system using PROCESSB for 30 minutes each for 2mm thick wafer.
- Check the etch depth using Daktak to confirm that the required depth is achieved (it should be around $200\mu m$).
- Repeat the photo-resist removing steps.
- Apply Blue tape to the top-side of the wafer.

- Spin coat wafer with AZ4620 PR at (500 for 10 seconds then 1500 for 40 seconds), bake 10 minutes in 90°C oven.
- Spin coat another layer of AZ4620 PR at (500 for 10 seconds then 1500 for 40 seconds), bake 30 minutes in 90°C oven.
- Expose in mask aligner (10mW, g-line lamp)for 180 seconds using mask 2 (Backside).
- Expose the same PR in mask aligner again (10mW, g-line lamp)for 180 seconds using mask 3 (Through Holes).
- Develop in 1 part AZ400k developer to 2 parts DI-water, for around 2-3 minutes (stir and pay attention not to overdevelop the wafer).
- Hard bake the wafer in 120°C oven for 15 minutes.
- Repeat the steps for attaching the wafer to a handle wafer.
- Etch in STS DRIE system using PROCESSB in segments of 30 minutes each. Stop the etching for 5 minutes in between the segments, and inspect the photo-resist, remove the wafer when all of the ports are open.
- Repeat cleaning steps mentioned earlier.

B.3.3 Anodic Bonding to Glass wafer

Clean the wafer carefully to achieve successful anodic bonding and reduce the chances for bond voids.

- After the Oxygen plasma cleaning of both sides of the wafer. Perform RCA cleaning for 20 minutes of the etched sample and a glass wafer at the same bath, use TEFLON holder.

- Rinse with DI water and make sure to blow dry it carefully, residual water will leave stains and lead to bond voids.
- Bring your samples to the wafer bonder and perform the anodic bonding in 1atm or higher of N_2 gas.

Samples were diced and processed individually to optimize different parameters of the process. The following description is for die-level processing.

B.3.4 Glass-Blowing

The process is described in Chapter 4, and here are some supplementary details.

Required and Recommended equipment

This procedure can use either annealing furnaces to blow an entire wafer or use the 2" tube

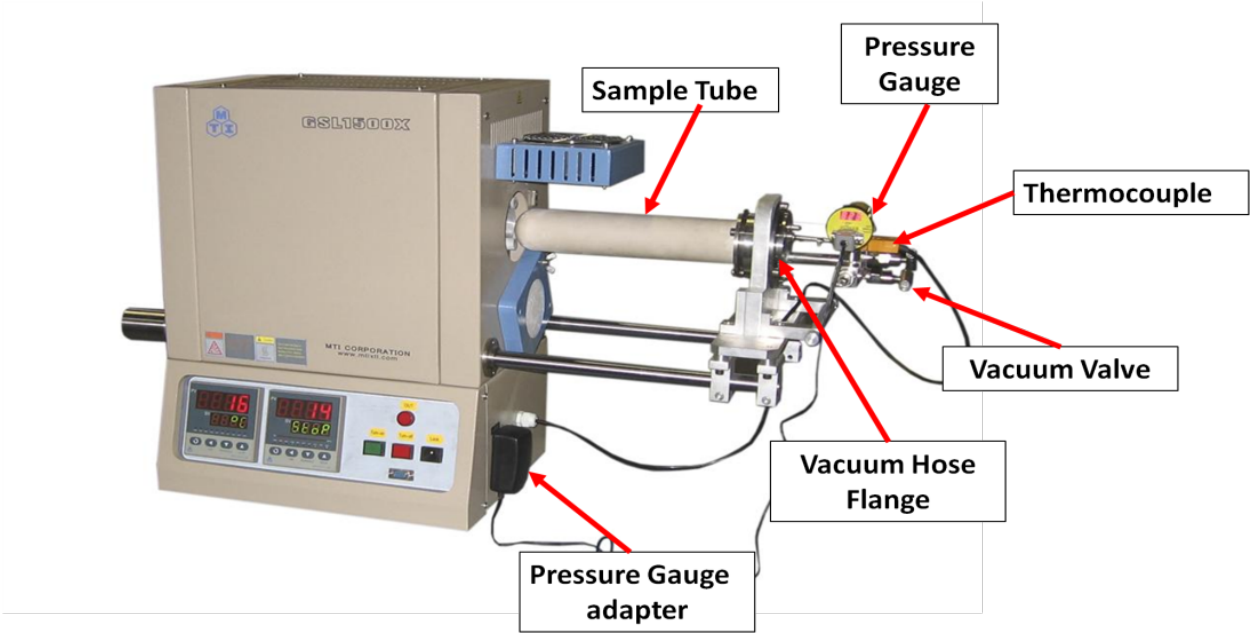

Figure B.1: Tube Furnace setup for vacuum blowing option.

furnace to blow single die. Tube furnace gives the advantage of blowing samples in partial

vacuum which gives better spherecity samples. The furnace used is: MTI Corporation (GSL-1500X) with a roughing vacuum pump, Figure B.1.

- Set the tube furnace to 880°C.
- Use the fused silica tube for the glassblowing process.
- Clean the sample: Apply standard solvent cleaning to the sample before it is glassblown to remove all organic residue on it. Use nitrogen-gun to dry it.
- Load your dies on the alumina sample boat, Figure B.2, and place the boat in the fused silica tube. Push it all the way to the end.
- Close the tube using the flange.
- Connect the temperature sensor and the pressure sensor as well as the vacuum pump hose to the flange.
- Turn on the vacuum pump, adjust the venting valve to set the desired blowing pressure using the pressure sensor.
- Turn off the pump and wait for the tube to vent, (DO NOT change the venting valve position).
- Push the tube into the furnace and wait for some time (3-7 minutes depending on the glass wafer thickness). Multiple iterations are needed to optimize the preheat time.
- Start the vacuum pump.
- Adjust the vent valve to control the pressure (50-300 torr). Note: this adjustment needs to be done in 30 seconds.
- Wait for (80 seconds) to blow the bubble up.

- Pull the tube out and slightly tighten the vent valve to reduce the pressure by 5-15 torr. This is required to prevent the bubble from collapsing.
- Wait 2 minutes then turn the vacuum pump off.
- Let the tube vent slowly, Note: if you vented quickly, it would break your sample.
- Open the tube and be careful not to damage the thermocouple.
- Use the special clamps to take out the boat and the sample, Figure B.3.
- Place the sample on a metal or ceramic piece and allow it to cool down.

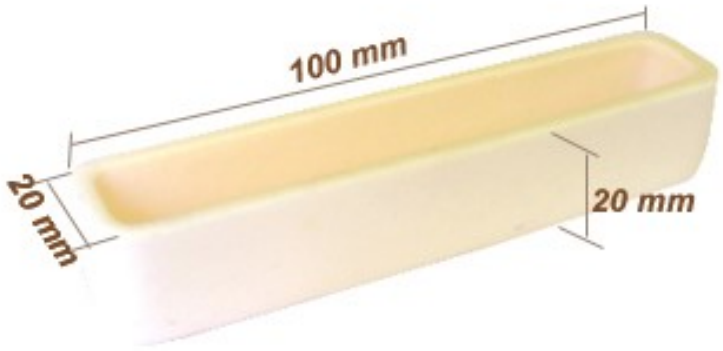

Figure B.2: Alumina Boat.

Figure B.3: Clamp to carry hot boat.

B.3.5 Backside opening

This procedure for is used to open the backside of the glassblown samples and prepare them for subsequent steps. Important points to be considered, the backside of the cells need

to be protected during DRIE process, the photo-resist needs to be cleaned completely after opening.

- Dice a dummy $500\mu m$ thick Si wafer into 25mm×25mm chips. These chips will be used to mount the glassblown cells.
- Dice a 2mm thick wafer into 5mm×10mm pieces. Theses will be used as spacers. NOTE: Make sure your bubble height is less than 2mm.
- set the hotplate to 95°C.
- Spin AZ4620 photo-resist (2000 RPM) on the 25mm×25mm chips, bake for 15 min on 95°C hotplate.
- Spin AZ4620 photo-resist (2000 RPM) again on the 25mm×25mm chips, put two spacers, bake for 15 min on 95°C hotplate.
- Spin AZ4620 photo-resist (3000 RPM) on the spacers, bake for 15 min 95°C hotplate.
- Spin AZ4620 photo-resist (3000 RPM) on the spacers, place the glassblown bubble upside down, press gently on the edges, bake for 15 min on 95°C hotplate.
- Using the glass pipette, pour AZ4620 photo-resist on your sample, if it has a through-hole in the middle try not to let the PR get into that opening, make sure to cover the edges with PR, spin (3000 RPM), bake for 10 min on 95°C hotplate, cover it with a glass petri dish while it is baking.
- repeat the previous step.
- Place the soft-mask on your sample using Kapton tape.
- Place the Si chip with the sample and the mask on a wafer using double-sided adhesive tape.

- Transfer the wafer to the exposure system, expose using a 10mW, g-line lamp, for 180 seconds.
- Remove the sample from the wafer, remove the mask, and develop in 1:3 Az400K: H_2O solution. Rinse with DI water.
- Double check under the microscope that the photo-resist is completely developed.
- Hard bake the sample on 120°C hotplate for 45 minutes, cover with glass petri dish while it is baking.
- The next step is mounting the Si chips with the upside-down samples on a handle wafer for backside DRIE etching.
- Cut blue tape into pieces equal in size to the Si Chips used for sample mounting. Attach the pieces to a handle wafer. One blue tape piece for each Si chip.
- Spin AZ4620 photo-resist (2000 RPM) on the handle wafer with blue tape pieces, bake for 30 min in the 90°C oven.
- Remove the Blue tape pieces. Apply a small drop of SANTOVAC 5 oil, spread it, attach the Si chip.
- Etch in STS for 10 to 15 minutes.
- Check if the bubble is open.
- Repeat the previous two steps until the bubble is open. DO NOT etch for longer than 15 minutes intervals. The PR will be consumed and the surface will be damaged and subsequent bonding will not be possible.
- Place the wafer of a 120°C hotplate for 2-3 minutes. Remove the Si chips from the wafer.

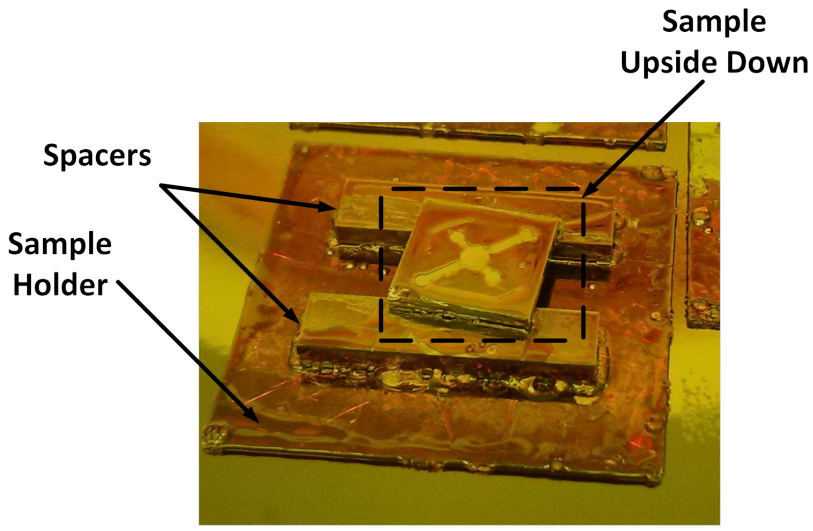

Figure B.4: Sample mounted upside down on spacers and a Si chip. The lithography step is completed here, ready for loading into STS.

B.3.6 Cell Cleaning

- Heat AZ400T to 70-80°C on the hotplate.
- Place the Si chip with the opened bubble in the solution.
- Check the sample gently if it can be released from the spacer. This may take up to an hour or two. DO NOT leave hot plate un-attended.
- Rinse sample with water, by placing the sample in a DI water bath.
- Repeat the previous step 2-3 times to remove AZ400T.
- Bake in 120°C oven for 20-60 minutes.
- Place the sample upside-down on a clean spacer (do not use PR to assemble this spacer). Perform oxygen plasma cleaning for 20-30 minutes In PlasmaTherm, for example.
- Perform RCA cleaning of the samples. Rinse with DI water.
- Make sure to blow dry the backside surface GENTLY using nitrogen gun.
- Place in 120°C dehydration bake oven for 2-3 hours.

B.4 Cell Filling

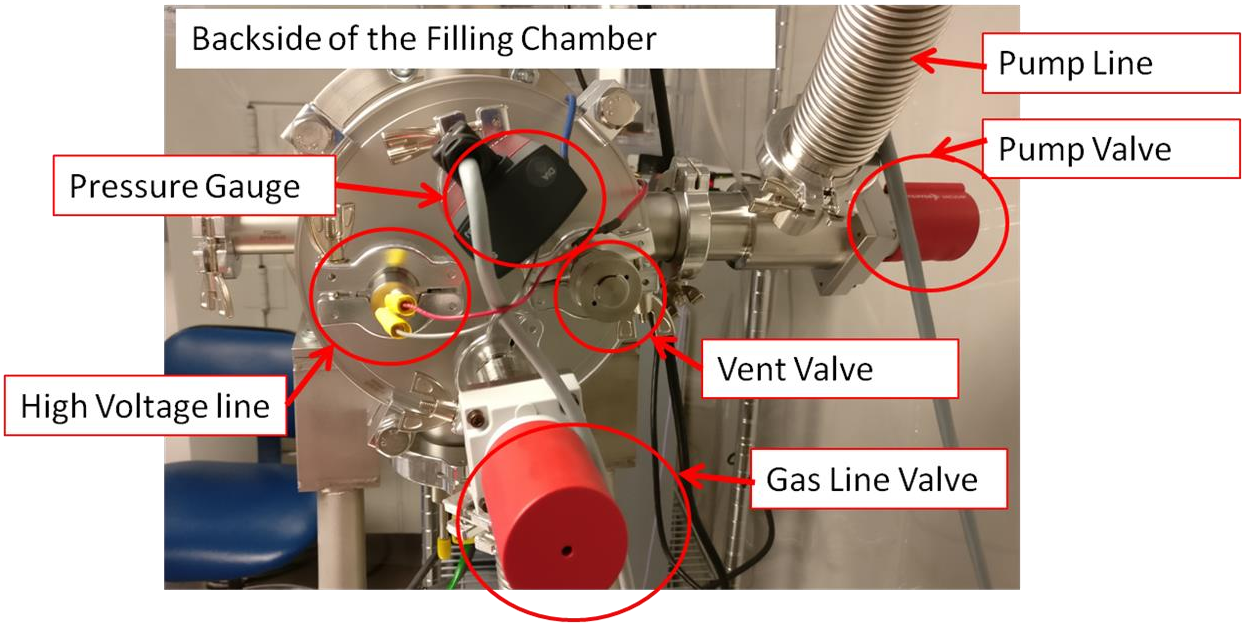

Figure B.5: Backside of the filling chamber showing pump, gas and venting valves, pressure gauge, high voltage and pump line.

Figure B.6: sample loading sequence: loading sample on the lower electrode then putting the ceramic frame, putting the metallic frame, putting dummy silicon sample to make the stack taller than the ceramic frame, returning the lower electrode to its position.

B.4.1 Procedure

Sample Loading

- Under a fume hood inside the clean room, place one Rb pill on the backside glass cover, place the cleaned sample on top of the glass cover and make sure the pill is setting

inside its chamber. Bring the sample stack to the filling station in EG 2119.

- On the filling station, close the valve that connects the pump to the chamber, figure B.5.
- Turn off the pump.
- Loosen the chamber's door nut.
- Vent the chamber using venting valve on the back, figure B.5.
- Remove the lower electrode and place it on the edge of the chamber door.
- Place the sample stack with the glass cap to the bottom on the center of the bottom electrode, figure B.6.
- Place the ceramic frame such that the sample fits in the center, adjust using tweezers, figure B.6.
- Carefully place the bonding frame on top of the sample, place dummy silicon die on top of the frame, such that the dummy die level is higher than the ceramic frame, figure B.6.
- Return the bottom electrode to its location, figure B.6.
- Close the chamber door, close the vent valve.
- Make sure the pump is completely stopped, and the frequency reading is 0Hz.
- Vent the pump using the venting valve.
- Open the pump line valve.
- Open the gas line valve.
- Start the pump.
- Keep pumping until the pressure reading is below $1x10^{-5}$ Torr.

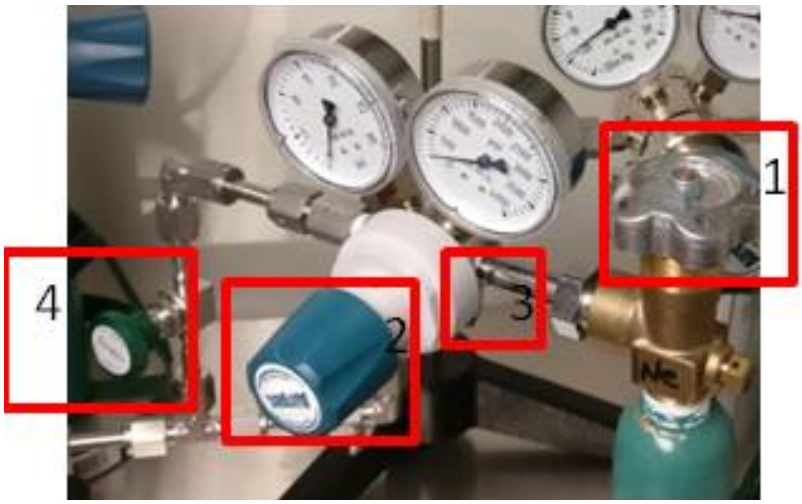

Figure B.7: Example of the 4 valves on each gas cylinder (1:Bottle valve, 2:pressure regulator, 3:regulator valve, 4:pipe valve)

- Set the heater to 350°C, turn it on to remove moisture, keep pumping until the pressure reading is around 1x10^{-5} Torr.
- Turn off the heater and let the sample cool down for few hours.
- Close the pump valve and turn off the pump.

Filling with gases

- Each gas cylinder has 4 valves (Bottle valve, pressure regulator, regulator valve, pipe valve). make sure all of them are closed before starting this, figure B.7.
- We will start by Xe.
- Reduce the regulator knob on the Xe bottle, to have control over the flow once the bottle is opened.
- Open the Xe bottle (using the bottle valve) and slowly adjust the regulator knob to control the flow, pump the desired amount (80-100 Torr), close the regulator valve, then the bottle valve.

- Repeat for other gases, Ne and N2.

- Wait 15 minutes to allow the gases to fill the sample.

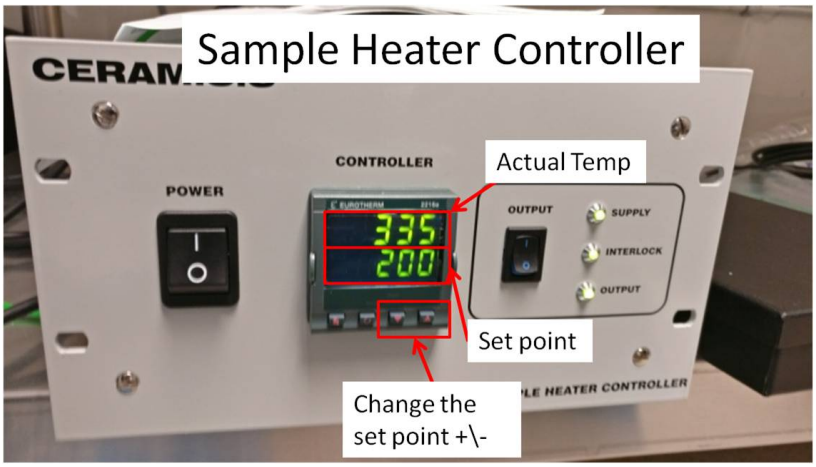

Figure B.8: Sample heater controller interface

Sealing the Cell

- Use Allan key to lower the top electrode slowly. Put the weights.

- Set the heater to 685°C then turn the output on, figure B.8. Wait 10 minutes until the sample is heated.

- Turn on the High Voltage supply, set the max current to 1mA (turn knob 1 on figure B.9 to "AMPS" then adjust knob 2 so that the reading in display 4 is "0.001"), set the

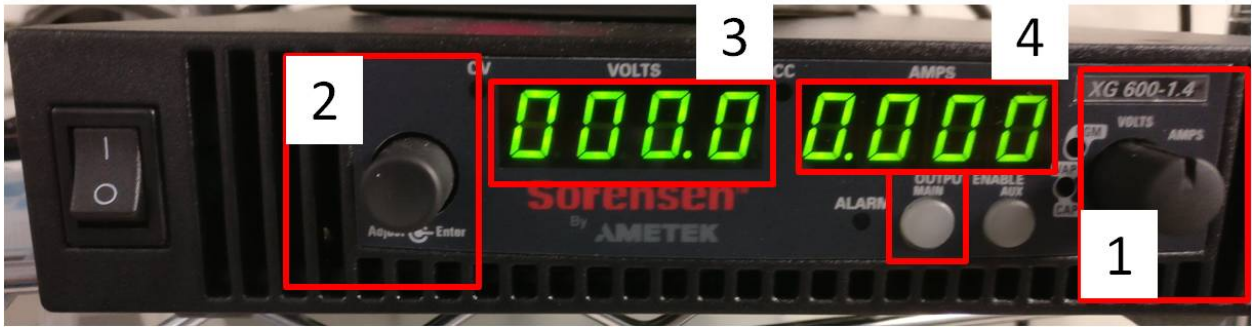

Figure B.9: High Voltage supply interface showing: 1) voltage or current selection knob, 2) adjustment knob, 3) Voltage reading, 4) current reading, and the main output toggle button)

max voltage to 600V (turn knob 1 on figure B.9 to "VOLTS" then adjust knob 2 so that the reading in display 4 is "600.0"). Turn the main output on. (you will observe the current display 4 on figure B.9 showing "0.002" that is the resolution of the device. you will also observe that the voltage is slowly rising and will stop around 350V, this is the bond-forming).

- Change the maximum current to 3mA and keep the voltage the same 600V. Turn on the output and wait 5 minutes. This will strengthen the bond
- Turn off the heater output and the voltage supply output.
- Wait a few hours or so to allow the sample to cool down. Never open the chamber while the heater is reading more than 200°C
- Remove the weights and lift the top electrode. Use Allan key to hold it in place.
- Vent the chamber and remove the bottom electrode, carefully remove the ceramic frame and use tweezers to remove the filling frame. Use tweezers to take the sample out.
- Inspect the bonding visually. There shouldn't be any large voids.

Activation of Rb pill

- Place the sample under activation laser, it is recommended to place it on a vertical stage with small steps to improve the focus.
- Put on the appropriate laser goggles and warn everyone in the room that you will be using the laser. It is invisible to the naked eye.
- Turn on the laser by turning the key switch to the left.
- Set the output power to 10% using the optical power slide, see figure B.10. Then start the emission

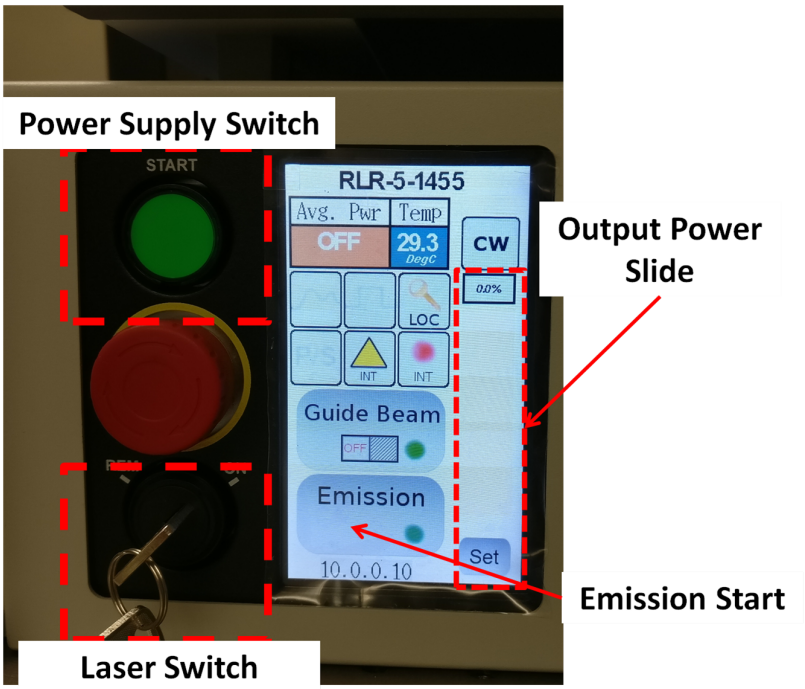

Figure B.10: Activation laser controller interface

- Use the IR viewer to focus the laser beam on the Rb dispenser. This Laser is dangerous and invisible, be careful when using it, always put on safety goggles

- After focusing the laser beam, turn off the emission, then increase the power to 75% and start the emission again for 30 seconds then stop. (the pill should be glowing in orange color).

- Now the cell is filled with an alkali metal and buffer gas, next step is to verify the presence of Rb using optical absorption experiment. The buffer gas content can be estimated using line-width shift and broadening of the absorption dips.

Appendix C

Vendors

Optics

Newport Corp.
1791 Deere Avenue, Irvine, CA, 92606.
Contact: 949-863-3144.
Website: *http://www.newport.com*
NOTE: High quality optical components, IR viewer and the optical rails were purchased from this vendor.

Thorlabs Inc.,
56 Sparta Avenue, Newton, New Jersey, 07860.
Contact: 973-579-7227.
Website: *http://www.thorlabs.us*
NOTE: Very versatile collection of optical components, most of the lenses, beam splitters, photodetectors, and kinematic mounts used in the optical setup shown in Chapter 4 were purchased from this vendor. Fast shipping usually components arrive in one week.

CVI laser optics,
200 Dorado Place SE, Albuquerque, NM 87123.
Contact: 505-296-9541.
Website: *https://www.cvimellesgriot.com/*

Lasers

IPG Photonics Corporation,
50 Old Webster Road, Oxford, MA 01540.
Contact: 508-373-1169 (Gregory Swope).
Website: *www.ipgphotonics.com*
NOTE: 5W CW 1455nm Raman Fiber Laser, used for activating Rb pills and optical heating.

Photodigm Corp.,
1155 E. Collins Blvd., Suite 200, Richardson TX 75081.
Contact: 972-235-7584 (Esther Moreno).
Website: *http://www.photodigm.com/*
795nm compact tunable laser for Rb spectroscopy up to 100mW, narrow line-width 1MHz

Wafers

Silicon wafers

Ultrasil Corporation,
3527 Breakwater Ave, Hayward, CA, 94545.
Contact: 510-266-3700 (Raymond Martin Duque).
Website: *http://www.ultrasil.com/*
NOTE: This vendor provides Si wafers with LPCVD films. The wafers used for fabricating the folded coils (Si + LPCVD 400nm SiN) were purchased from this vendor.

University Wafer,
850 Summer St. Suite# 207, Boston, MA 02127, USA
Contact: 800-713-9375 (Chris Baker).
Website: *www.UniversityWafer.com*
NOTE: Prime Si wafers with different thicknesses as well as Pyrex wafers. The 1mm thick prime Si wafers used for fabricating the cell network samples were purchased from this vendor.

Glass wafers

Mark Optics,
1424 E. St. Gertrude Place, Santa Ana, CA 92705
Contact: 714-545-6684 (Erika Puentes).
Website: *www.markoptics.com*
NOTE: Has a wide variety of glass wafers with different compositions and sizes. The Borosilicate glass (Pyrex) wafers used in the fabrication of cell network samples were supplied by this vendor.

HOYA Corp.,
680 North McCarthy Blvd, Suite 120, Milpitas, CA 95035-5120.
Contact: 408-654-2274.
Website: *www.hoyaoptics.com*
E-mail: *naoko.sato@hoya.com* (SATO Naoko)
NOTE: This vendor supplies the Aluminosilicate Glass (SD-2) wafers used in the study of different cell walls materials in Chapter 4.

Photo-lithography Masks

Photo-sciences,
2542 W 237th St., Torrance, CA, 90505.
Contact: 310-634-1500.
Website: *https://dev.photo-sciences.com/*
NOTE: This vendor provides high-quality chrome masks with fast turn around (less than a week). The masks for fabricating the folded coils and heaters described in Chapter 3 were purchased from this vendor.

CAD/Art Services,Inc.
87509 Oberman Lane, Bandon, OR 97411
Contact: 541-347-5315.
Website: *https://www.outputcity.com/*
Email: *cas@outputcity.com*
NOTE: This vendor provides lower resolution and inexpensive printed soft-masks. The masks for fabricating the cell network designs used soft masks from this vendor.

PCB

JLC PCB
Shenzhen, China
Website: *https://jlcpcb.com/*
Email: *support@jlcpcb.com*
NOTE: This vendor provides fast and affordable PCB prototyping. The emulator PCB was supplied by this vendor. The turn-around time is less than 10 days.

Sierra Assembly Technology Inc.
10880 Mulberry Ave, Fontana, CA 92337
Contact: 909-355-5400.
Website: *https://www.protoexpress.com/*
NOTE: This vendor supplies high-quality, specialized PCBs. The PCB for the folded NMR sensor prototype shown in Chapter 3 was ordered from this vendor. Usually long lead time (3-5) weeks and more expensive than JLCPCB.

Clean Room and Vacuum Systems Supplies

Ceramisis Ltd.
30 Brunel Road, St. Leonards on Sea, East Sussex, TN38 9RT, England, UK.
Contact: +44-7793-363440.
Website: *http://www.ceramisis.com/*
NOTE: Custom Vacuum Heater installed in the atomic cell filling station in EG2119, UCI. This heater heats up the sample to 400°C for the anodic bonding process. It can go up to 1200°C.

Ceramco Inc.
1467 E MAIN ST, CENTER CONWAY, NH 03813.
Contact: 603-447-2090.
Website: *https://www.ceramicfasteners.com*
NOTE: Replacement ceramic screws for the filling station heater.

Pfeiffer Vacuum Inc.
1622 Garland Ave, Tustin, CA 92780, USA.
Contact: 714-803-1895.
Website: *http://www.pfeiffer-vacuum.com/*
NOTE: This vendor supplied the custom Vacuum Chamber, turbopump, loading arm, and vacuum parts of the filling station shown in Appendix A.

PTB Sales
1361 Mountain View Circle, Azusa, CA 91702
Contact: 626-334-0500.
Website: *http://www.ptbsales.com/*
NOTE: Local Vacuum pumps repair, they provided option to pick-up pumps form lab. Affordable, lead time 3-4 weeks.

MTI Corp.
860 S. 19th Street, Richmond, CA 94804-3809.
Contact: 510-525-3070.
Website: *http://www.mtixtl.com/*
NOTE: This vendor provided the 2" tube vacuum glassblowing furnace that was shown in Appendix B.3.4

TDI International
4595 Mountain Lakes Blvd, Redding, CA 96003.
Contact: 530-243-2200.
Website: *https://www.tedpella.com/*
NOTE: Clean-room supplies, SEM Supplies. Chemical resistant tweezers sample and wafer tweezers were purchased from this supplier.

Atomic

SAES Getters
1122 E. Cheyenne Mountain BLVD Colorado Springs, CO 80906
Contact: 719-527-4116.
Website: *https://www.saesgetters.com/*
Email: *Heather_Florence@saes-group.com* (Heather Florence)
NOTE: This vendor supplied the Rb dispensers described in Chapter 4. Lead time is 8 weeks, minimum order amount applies.

Airgas USA, LLC-West Region.
23585 Los Adornos Aliso Viejo, CA 92656
Contact: 619-787-1425.
Website: *http://www.airgas.com/*
Email: *Todd.Price@airgas.com* (Todd Price)
NOTE: This vendor supplied the processing gases for cell filling such as, natural Xenon, Neon, and Nitrogen gases.

Machining and Prototyping

UCI FABWorks.
University of California Irvine, California IT2, Irvine, CA 92697.
Contact: 949-824-5667.
Website: *http://manufacturing.uci.edu/index.php/fabworks-2/*
NOTE: self serve 3D printing, laser cutting, and CNC machining. The guided folding mold discussed in Chapter 3 was 3D printed by this vendor.

UC Irvine Research Machine Shop.
B012 Reines Hall, Irvine CA 92697
Contact: 949-824-6445.
Website: *https://ps.uci.edu/content/ps-machine-shop-research*
Email: *msteinbo@uci.edu* (Manager: Mark Steinborn)
NOTE: This shop provides quality machined parts and welding services to faculty and students. Several parts were machined in this machine shop including, Aluminum and ceramic filling frames shown in appendix B.4, and attachments to the electrodes of filling station shown in appendix A.